

---

# Linear-Petahertz-PhotoConductive Switching

Keyhan Golyari

---



München 2022



---

# Linear-Petahertz-PhotoConductive Switching

Keyhan Golyari

---

Dissertation  
an der Fakultät für Physik  
der Ludwig-Maximilians-Universität  
München

Vorgelegt von  
Keyhan Golyari  
aus Mashhad, Iran

München, den 04.02.2022

Ertsgutacher: Prof. Dr. Ferenc Krausz

Zweitgutachter: Prof. Dr. Jens Biegert

Tag der München Prüfung, 22.03.2022

# Table of contents

Zusammenfassung:.....	ix
Abstract: .....	xi
List of abbreviations:.....	xiii
List of figures .....	XV
1. Introduction:.....	19
1.1. Overview of different measurement techniques.....	21
1.2. Nonlinear photo-conductive sampling.....	24
2. Theoretical background.....	31
2.1. High harmonic generation .....	31
2.2. Attosecond Streaking.....	36
2.2.1 SNR of attosecond streaking.....	38
2.3. Intra-band current.....	40
2.4. Bloch equation .....	41
2.5. Landau-Zener transition.....	43
3. Experimental Setup and measurement procedure. ....	51
3.1. Laser source .....	51
3.2. AS2000.....	53
3.2.1. HHG chamber .....	53
3.2.2. Delay chamber .....	54
3.2.3. Experimental chamber .....	55
3.3. Data acquisition .....	56
3.3.1. Photo-conductive sampling.....	56
3.3.2. Streaking .....	58
3.4. Experimental procedure.....	60

3.4.1: Streaking .....	60
3.4.2. Photo-conductive sampling.....	60
<b>4. LPPS in solids .....</b>	<b>61</b>
4.1: Theory of ultra-fast currents .....	61
4.2. LPPS in SiO <sub>2</sub> and LiF .....	63
4.3. Benchmarking of LPPS in solids vs attosecond streaking .....	66
4.4. Bandwidth of detection of LPPS in solids.....	68
4.5. Dynamic range of LPPS in solids.....	73
4.6. Conclusion of LPPS in solids .....	80
<b>5. LPPS in gases.....</b>	<b>81</b>
5.1 Measurement procedure.....	81
5.2: Source of signal .....	83
5.2.1: comparison of dipole magnitude in LiF and Ne .....	83
5.2.2: Population transfer .....	84
5.2.3: Metallic barrier transmission probability.....	86
5.3. CEP dependence of the signal .....	89
5.5. Dynamic range .....	92
5.6: Extension of bandwidth of detection in LPPS by Ne.....	93
5.6.1: UV light generation.....	94
5.6.2: Signal modulation .....	94
5.6.3: Measurement geometry.....	94
5.6.4: Streaking of UV pulse.....	95
5.6.5 Differentiating between noise and signal at high frequencies .....	96
5.6.6 Second harmonics detection by LPPS .....	100
5.6.7 A recipe to increase SNR for second harmonics signal.....	102
5.7. Conclusion of LPPS in gases .....	105
<b>6. Conclusion and outlooks .....</b>	<b>107</b>

Bibliography..... 111  
Appendix A. Lock-in modulation: ..... 119  
Appendix B. lithium fluoride crystal: ..... 121  
Appendix C. Data Archiving:..... 122  
Acknowledgements ..... 123



# Zusammenfassung:

Nonlinear Photoconductive Sampling (NPS) als ein zeitaufgelöstes Messverfahren des elektrischen Feldes deckt eine große Bandbreite im optischen Frequenzbereich ab. In diesem Verfahren wird ein dielektrisches Material mit großer Bandlücke durch die nichtlineare Wechselwirkung mit einem intensiven Wenige-Zyklen Träger-Einhüllenden-Phase (CEP) stabilen Lichtpuls leitfähig. Danach werden die erzeugten freien Ladungsträger mit einem orthogonal polarisierten verzögerten kurzen Lichtpuls im Leitungsband des Materials gesteuert und ein makroskopischer elektrischer Dipol wird im Material induziert. Das elektrische Feld dieses Dipols wird durch externe Elektroden abgeschirmt, wodurch dort eine elektrische Ladung induziert wird, die proportional zum Vektorpotential des verzögerten Feldes ist. Der starke nichtlineare Charakter des NPS bringt mehrere Unbestimmtheiten hinsichtlich des Anfangszustands des injizierten Ladungsträgerwellenpakets mit sich, wodurch seine Untersuchung verkompliziert wird.

Diese Arbeit zielt darauf ab, die Komplexität des NPS durch ultra-kurze lineare Injektion mit einem Vakuum-UV-Puls zu vereinfachen. Darüberhinaus wird durch die lineare Induktion der Leitfähigkeit der Injektionsschritt von der Ansteuerung entkoppelt, wodurch auch die Notwendigkeit der orthogonalen Polarisation für die Injektions- und Ansteuerungspulse entfällt.

Ein in-situ Vergleich zwischen diesen Strömen und Attosekund Streaking beweist, dass wenn das Leitungsband eines Materials eine parabolische Dispersionsrelation besitzt, ist die Gruppengeschwindigkeit der injizierten Bloch-Wellenpakete proportional zum Vektorpotential des Ansteuerungsfeldes.

Ein Vergleich zwischen den Photoströmen in Lithiumfluorid und amorphem Siliziumdioxid wird durchgeführt. Das Ergebnis zeigt, dass die linear induzierte Photoleitfähigkeit in einem Medium mit großer Bandlücke die obere Grenze der nachweisbaren Frequenzen des elektrischen Feldes erhöht. Ein Kreuzkorrelationsanalyse zwischen der spektralen Antwort in Attosecond Streaking und unserem Verfahren zeigt, dass die Dauer der linearen Photoinduktion der Ladungsträger in LiF auf weniger als 1.2 fs begrenzt ist. Da diese Schaltfrequenz in der Nähe von 1 Petahertz ist, nennen wir dieses Verfahren Linear Petahertz Photoconductive Switching (LPPS).

Der Untersuchung des dynamischen Bereichs des LPPS zeigt, dass diese Methode bis zu einer Ansteuerungsfeldamplitude von  $F_0 = 0.2 \text{ V/\AA}$  linear ist. Derzeit liegen die kleinsten messbaren Feldoszillationen überhalb des Hintergrundrauschens fast  $0.008 \text{ V/\AA}$ . Daher hat das Verfahren in LiF einen dynamischen Bereich von fast 27 dB.

Die Ansteuerung der photoinduzierten Ladungsträger mit den Feldamplituden von über  $0.2 \text{ V/\AA}$  resultiert in die Abweichungen der Ströme vom entsprechenden Vektorpotential. Wir folgern daraus, dass die begrenzte Ausdehnung des nahe parabolischen Dispersion im ersten Leitungsband von LiF und der Landau-Zener Übergang der elektronischen Bloch-Wellen der oberen Bänder diese Abweichungen verursachen.

Die Ergebnisse des LPPS in LiF zeigen, dass wir für ein gutes Signal-Rausch-Verhältnis (SNR) zwei Bedingungen benötigen. 1) eine große lineare Übergangsenergie und 2) ein unendliche

ausgedehnterparabolischer Endzustand. Inerte Gase sind dafür perfekten Kandidaten. Wir führen daher die gleichen Experimente in Neon durch (Ionisierungsenergie von 21.56 eV). Die erste Beobachtung ist, dass das SNR in Neon 158 mal stärker als in LiF ist. Wir schließen daraus, dass hier die Ursache für dieses gewaltige Signal der Transport der Elektronen zu den Elektroden ist. Wir sehen auch, dass LPPS in Neon eine größere spektrale Empfindlichkeit gegenüber dem UV-Bereich besitzt. Schließlich berichten wir, dass die unendlich ausgedehnten parabolische freien elektronische Endzustände in Neon den Dynamikbereich des LPPS auf über 50 dB in der Intensität erweitern.

Zuletzt untersuchen wir das Ausmaß der spektralen Bandbreite der Messung durch Frequenzverdopplung des grundlegenden NIR-Transienten (1000 nm bis 500 nm) unter Verwendung eines Beta-Bariumborat (BBO)-Kristalls. Diese Messungen zeigen, dass die spektrale Grenze der Detektion bis zu 1 PHz (300 nm) erreichen kann. Theoretische Berechnungen zeigen, dass das SNR des Signals der zweiten Harmonischen verdoppelt werden kann, indem die CEP des NIR-Pulses, der den Injektions-VUV-Puls erzeugt, so gewählt wird, dass pro Oszillationszyklus der zweiten Harmonischen ein lineares Injektionsereignis stattfindet.

# Abstract:

Nonlinear photoconductive sampling (NPS) as a time-resolved measurement technique covers a large bandwidth of measurement. In this method, a large band-gap material is nonlinearly photo-conducted by a strong few-cycle CEP stable laser pulse. A second delayed optical transient further steers these carriers in the conduction band of the material, that induces a macroscopic electric dipole in the medium. The electric field of this dipole screens electric charge on external electrode that is proportional to the vector potential of the delayed optical transient. The strong nonlinear nature of the photo-injection in NPS brings multiple uncertainties on the initial state of the injected carriers' wave-packet. As a result, deeper study of these photo-currents becomes complicated.

The work presented in this thesis was motivated by the need to simplify these complexities of NPS through ultra-short injection of photo-carriers linearly. Linear injection by short VUV pulses decouples the injection and the driving steps, which eliminates the requirement of orthogonal polarization for the injection and the drive pulses.

An in-situ comparison of these currents with attosecond streaking proves that, when the dispersion relation of these bands is parabolic, the group velocity of injected Bloch wave-packets is proportional to the vector potential of the driving field.

A comparison of the induced photo-currents in lithium fluoride and amorphous silicon dioxide was performed. The result of this comparison reveals that photo-conduction in a medium with a larger band-gap extends the cutoff frequency of the detection. A cross correlation analysis between the spectral response of the field measurement of attosecond streaking and this current sampling technique showed that the duration of linear carrier photo-injection in LiF is confined to less than 1.2 fs. Since this switching frequency is close to the 1 petahertz frontier, we call the sampling technique Linear petahertz Photo-conductive switching (LPPS).

The measurement of the dynamic range of LPPS in LiF show that this technique up to driving field amplitude of  $F_0 = 0.2 \text{ V/\AA}$  remains linear. Meanwhile, the smallest detectable oscillations above the noise floor are about  $0.008 \text{ V/\AA}$ . This is about 27 dB of intensity dynamic range.

Steering photo-carriers with driving field amplitudes above  $0.2 \text{ V/\AA}$  results in a deviation of the currents from the vector potential. It was deduced that the limited parabolic extent of the LiF first conduction band and Landau-Zener transition electronic Bloch waves to upper bands cause these deviations

LPPS in LiF shows that for good SNR we need two conditions. 1) a large linear transition energy and 2) a large parabolic final state that ideally extends to infinity. Inert gases are perfect candidates. Experiments were performed in neon (Ionization energy of 21.56 eV). The first observation is that the SNR is 158 times stronger than the case of LiF. We deduced that the cause of this huge signal is the transport of the electrons to the electrodes. Also, we see that LPPS in Ne has more spectral sensitivity toward the UV region. Finally, we report that, the infinite parabolic free electronic state of Ne extends the dynamic range of LPPS to above 50 dB in intensity.

Finally, we set out to discover the extent of the spectral bandwidth of the measurement by frequency doubling the fundamental NIR transient (1000 nm to 500 nm) using a beta-barium borate (BBO) crystal. These measurements show the spectral cutoff of the detection can reach 1 PHz (300 nm). We calculated that the SNR of the second harmonic signal can be doubled, by choosing the CEP of the NIR pulse that generates the injection VUV pulse such that one linear injection event occurs per second harmonic oscillation cycle.

# List of abbreviations:

BBO	Beta-Barium Borate
BNC	Bayonet Neill–Concelman
CB	Conduction band
CCD	Charge coupled device
CEP	Carrier-envelope-phase
DFG	Difference frequency generation
DFT	Density functional theory
EOS	Electro-optic sampling
FROG	Frequency-resolved optical gating
HCF	Hollow-core fiber
HHG	High harmonic generation
LPPS	Linear petahertz photo-conductive switching
MCP	Micro-channel-plate
MODFET	The modulated-doping field effect transistor
MIR	Middle infrared
Nd:YLF	Neodymium-doped yttrium lithium fluoride
NIR	Near infrared
NPS	Nonlinear photo-conductive sampling
PCB	Printed circuit board
PPLN	Periodically poled lithium niobate
Reflective focal length	RFL
SFG	Sum frequency generation
SHG	Second harmonic generation
SNR	Signal to noise ratio
SPM	Self-phase modulation
TDDFT	Time-dependent density functional theory
TIPTOE	Time-domain observation of an electric field
Ti:Sa	titanium-sapphire
TOF	Time-of-flight spectrometer
UV	Ultraviolet
VB	Valence band
VUV	Vacuum ultraviolet
XUV	Extreme Ultraviolet



# List of figures

- 1.1 Schematic of bipolar junction transistor
- 1.2. Time resolved energy transfer between the electric field and the electric dipole moment of the medium and electric field
- 1.3 Spectral response of NPS
- 1.4 Schematic of geometry of existing fields in NPS
- 1.5 Depiction of complications of nonlinear carrier photo-injection in NPS
- 2.1 Tunneling ionization step in HHG
- 2.2 Comparison of effect of CEP on the cutoff energy and the yield of harmonics
- 2.3 Schematic of the attosecond streaking measurement
- 2.4 Normalized spectra of electrons detected by TOF from photoionization by XUV photons
- 2.5 Comparison of electric field and vector potential in time-domain
- 2.6 Validity of semi-classical model
- 2.7 Time evolution of energy eigenvalue of two-level system in Landau Zener model
- 2.8 Semi-classical demonstration of the time required to for Landau Zener tunneling
- 2.9 Demonstration of crossing bands
- 2.10 Demonstration of anti-crossing bands
- 3.1 Schematic of the HHG chamber in AS2000
- 3.2 Schematic of the Delay chamber in AS2000
- 3.3 Schematic of the Experimental chamber in AS2000
- 3.4 The sampling medium of LPPS in LiF and SiO<sub>2</sub>
- 3.5 Feedthrough CF flange with floating ground
- 3.6 Definition of zero-channel in streaking electron spectra
- 3.7 Calibration of electron kinetic energy with the time of flight at 200 V of lens
- 4.1 Linear Photoconduction procedure
- 4.2 Two color scheme for creation of ultra-fast currents in large bandgap solids
- 4.3 Macroscopic picture of the detection of the ultra-fast currents
- 4.4 Density functional theory (DFT) calculations for LiF band structure along x cut of the crystal
- 4.5 Density functional theory (DFT) calculations for LiF band structure along x cut of the crystal for bands above 20 eV

- 4.6 LPPS benchmarking setup
- 4.7 Benchmarking of the LPPS in SiO<sub>2</sub> with streaking in Ne
- 4.8 Benchmarking of the LPPS in LiF with streaking in Ne
- 4.9 Frequency sensitivity of the LPPS in SiO<sub>2</sub>
- 4.10 Frequency sensitivity of the LPPS in LiF
- 4.11 Illustration of the effect of injection time on bandwidth of LPPS in time-domain
- 4.12 Calculated temporal profile of the VUV pulse that injects the carriers into the CB of the LiF
- 4.13 Intensity-dependent LPPS measurements in LiF
- 4.14 Deviation from vector potential at driving in LPPS in stronger driving amplitudes.
- 4.15 Extend of parabolic dispersion region for the first CB of the LiF
- 4.16 Demonstration of the mechanisms that cause deviations from vector potential like behavior of the optical driven currents
- 4.17 All the steps that lead to the final current in LPPS
- 5.1 Data acquisition for the LPPS in gases
- 5.2 The comparison of the signal amplitude of the LPPS in Ne and in LiF
- 5.3 Population transfer mechanism in LPPS in Ne
- 5.4 Comparison of the signal from population transfer mechanism and the vector potential of the driving field at three different driving amplitudes
- 5.5 Comparison of the signal from Metallic barrier transmission probability mechanism and the vector potential of the driving field at three different driving amplitudes
- 5.6 Comparison of the signal from both mechanism and the vector potential of the driving field at three different driving amplitudes
- 5.7 Comparison of the LPPS signal at 2 different injection CEPs
- 5.8 Envelope of the injection pulse at 2 different injection CEPs
- 5.9 Streaking spectrogram for the bench marking for LPPS in gas
- 5.10 Comparison of the retrieved vector potential from streaking with detected current from LPPS in Ne
- 5.11 Comparison of the spectrum of the detected signals in streaking and LPPS in Ne and their respective group delays
- 5.12 Comparison of the LPPS signal in gas for 6 different field amplitudes with the reference signal
- 5.13 The lowest detectable current oscillation by LPPS in Ne
- 5.14 Schematic optical geometry of the LPPS setup for detection of the second harmonics
- 5.15 Results of Attosecond streaking for detection of the second harmonics of the NIR pulse from Ti:Sa. Source

- 5.16 Higher frequency parts of time derivative of streaking signal of the generated second harmonic.
- 5.17 Comparison of the extracted second harmonics field with fundamental field
- 5.18 Final test for separating the signal from the noise of the second harmonics signal
- 5.19 The measured LPPS current of the second harmonics field (@ 390 nm) and the fundamental field at (@ 780 nm)
- 5.20 Spectral sensitivity of LPPS in Neon
- 5.21 comparison theoretical detected fundamental and 2<sup>nd</sup> harmonics signal if both have same amplitude
- 5.22 The CEP dependence of spectral sensitivity of the LPPS for fundamental and second harmonics spectrum of the Ti:Sa source
- 5.23 Comparison of the calculated time-dependent signal based for different CEPs
- A.1 CEP flipping detection mechanism with lock-in amplifier
- A.2 Demonstration of the failure of the CEP flipping scheme in 2<sup>nd</sup> harmonics detection.
- A.3 Signal modulation scheme for detection of the 2<sup>nd</sup> harmonics pulse



# 1. Introduction:

One of the grand goals of signal processing is to push its speed further into the petahertz region [1,2]. Currently, the maximum speed of electronic processing, by modulation doped field-effect transistors (MODFET), is about 0.25 THz [3]. Using high electron mobility transistors, this limit can be pushed toward 1 THz [4]. The limiting factor in the speed of processing is due to the dependence of these gating systems on the transport of electrons along semiconductor junctions; therefore, different scattering processes limit the electron mobility and as a result the processing speed.

A normal semiconductor-based switch has a base pin that provides electronic carriers and the gate allows these carriers to flow toward their collection point. Carriers are provided by doped semiconductors that are biased by a DC voltage. The junction is a configuration of P-type and N-type semiconductors which creates a potential barrier from the emitter and the collector pin. The gating can turn on and off the conductivity of this semiconductor bridge which allows the carriers to flow through the switch (figure 1.1). An ideal switch should allow instant transport of the charge carriers. But the uncertainty principle dictates that the lower limit of the switching time  $\Delta T_{\text{swt}} \geq \hbar/E_{\text{gap}}$  [5]. Semiconductors usually have bandgaps around 1 eV. Therefore, the switching time cannot be shorter than  $\Delta T_{\text{swt}} = 4.2$  fs. Increasing the bandgap reduces this intrinsic time scale but, on the other hand, reduces the conductivity of electrons<sup>1</sup> [6]. This is only achievable in the ideal case where switching speed is not limited by carrier mobility and diffusive transport limitations. Therefore, all electronic signal processing is not a promising way to achieve petahertz signal processing.

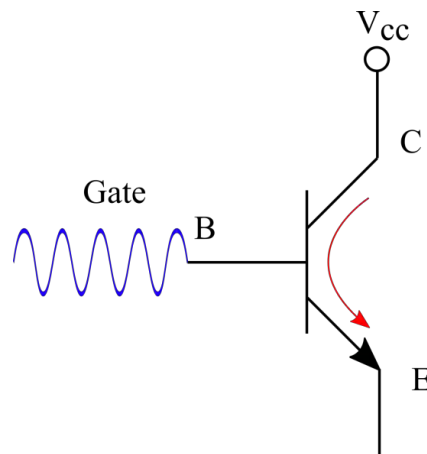


Figure 1.1. A common NPN bipolar semiconductor transistor switch.  $V_{cc}$  is the DC voltage that carriers. Existence of the middle P-type semiconductor between the base and the collector and the base and the emitter prevents the current to flow through the collector to the emitter. Applying a voltage between the base and the collector pin would suppress the PN potential barrier. As a result, electrons will move from the emitter to the collector. Since by convention movement of positive charges defines the direction of the electric current the current arrow is from the collector to the emitter.

Auston et al. [7] have proven that using photoconduction as the source of switching can increase the speed of signal processing up to 0.6 THz. The switch consists of two electrodes that are connected by a

---

<sup>1</sup> This relationship is an indirect consequence of the size of the bandgap. The conductivity is the product of carrier mobility and carrier concentration. The former is dependent on the curvature of the band structure. The latter is related to the density of states and the occupation number of the band. Bigger bandgap materials have smaller carrier concentrations therefore their conductivity is lower.

semiconductor. These electrodes are biased by a DC voltage. The carriers are provided by linear photoconduction from the electric field of a pulsed laser with femtosecond pulses which are focused on the gap. The excited charge carriers in the conduction band of the semiconductor are subsequently accelerated by the bias voltage. The induced acceleration from the photocurrent causes the charge carriers to radiate at terahertz frequencies, generating a pulse lasting several picoseconds [8, 9]. The limiting factor for the speed of such switch is the rise time of carrier excitation, transit time of carriers, and screening effects at interconnects [10]. This limitation can be reduced if the driving of carriers is done by optical means.

An early evidence which supports the hypothesis that nonlinear optical transition can serve as fast switching gate, was the generation of high harmonics in solids [11]. Ghimire et.al have shown that focusing a mid-infra-red (MIR) pulse on a ZnO crystal would create harmonics of the MIR source up to 25<sup>th</sup> order [12]. The observations shows that the frequency spacing of such harmonics is twice that of the carrier frequency of the intense driving field, thus it is deduced that these carriers' dynamics should happen with the period of half cycle of the strong field. A simple explanation of this observation is as follows: The intense laser pulse allows the electrons to tunnel from the valence band (VB) to the conduction band (CB). This creates an inter-band current. Afterward, the electronic Bloch wave-packet is steered by the same field, which results in the generation of Bloch oscillations in the band structure. Steering of Bloch waves creates an intra-band current. When these charge carriers reach the edge of the Brillouin zone, they Bragg diffract and return to the zone from the opposite side of the band, having a non-parabolic band result in generation of higher energy photons as result of these periodic motion. Later, it was shown that steering carriers into non-parabolic parts of CB is enough to create odd harmonics [13] During the excursion of carrier in the CB, it can recombine with the respective hole in VB at a different point in band. This also result in generation of high energy photons. [14]. Further proof of such ultra-fast dynamics has been reported, for example, by M. Schultze et.al. [15]. They reported that the absorption rate of the extreme-ultra-violet (XUV) in SiO<sub>2</sub> can be modulated by strong field interaction with a laser field at field amplitudes near  $= 2 \text{ V/\AA}$ . These modulations of the XUV absorption were in synchrony with the vector potential of the strong laser pulse, providing a sub-cycle control of the optical properties of the SiO<sub>2</sub>. In a recent development, J. A. Gessner has shown that depending on the conductivity of the material (i.e. metallic, semiconductor, or insulator) these modulations can be in synchrony to an electric field or the vector potential of the strong field [16]. Furthermore, H. Mashiko et.al [17] showed that using strong field interactions in gallium nitride, dipole oscillation can be manipulated on a timescale as fast as 860 as. The resultant dipole frequency reaches 1.16 PHz, showing the potential for future high-speed signal processing technologies based on wide-bandgap semiconductors.

Probing of such petahertz sub-cycle dynamics requires the time-domain measurement of the electric field of the optical pulses. Any ultra-fast dynamics induced by photoconduction and further being driven by another optical field create radiation that modulates the driving field. The time-domain study of the radiation not only provides information about the "fastness" of induced dynamics but also can serve as a new strong spectroscopic technique. This is due to the fact that the emitted radiation has a unique temporal fingerprint for each material. These kinds of measurements are usually done in a pump-probe manner. The pump is always a strong interaction that triggers these electronic dynamics. This causes a change in the optical properties of the medium under interaction including the absorption coefficient, linear and nonlinear refractive index, and electronic conductivity. The probe is normally a weaker interaction that is delayed versus the pump, which is used to measure these changes.

The study of dynamics which arise due to injection would be hard if we cannot distinguish the excitation from the secondary dynamics. This becomes more difficult when the excitation is temporally long. For example, a simple case of energy transfer between medium and light becomes ambiguous. Whether the energy transfer is due to excitation itself -which means that imaginary part of the susceptibility tensor of medium is changing- or the change is due to changes in the wave function of the electron in the new excited

state by the same field –changes in the real part of susceptibility tensor- [18]. Therefore, the excitation step and the subsequent electronic dynamics become coupled (figure 1.2). One way to decouple these steps is achieved by confinement of the excitation steps to shorter time windows. Short excitation on the sub-cycle timescale provides a better understanding of how fast the optically driven dynamics can be induced. Additionally, since, optical interactions that happen in shorter time scales can excite a larger band of electronic excitations, ranging from fast electronic to slower molecular dynamics can be induced. The former happens in normally the UV-VIS-NIR and the latter occurs in the NIR-MIR spectral range. In terms of the optical bandwidth, the dynamics can cover more than two octaves of bandwidth.

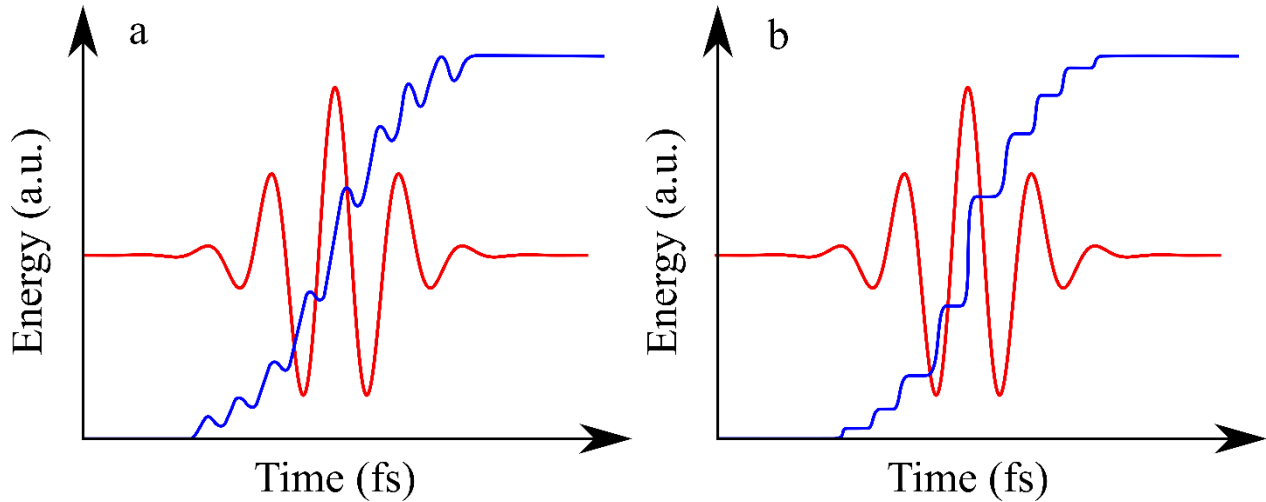


Figure 1.2. Time-resolved energy transfer between the electric field and the medium  $W(t) = \int_{-\infty}^t E(t') \frac{dP(t')}{dt'} dt'$  (blue curve), the electric field of the interacting radiation (red curve). a) when we consider the dipole acceleration during the injection. The steps can be the result of the injection of the carrier from the initial state to the final state of the medium, the modulations on the steps are due to the driving of the carriers in the final step. b) turning off the drive artificially the steps become clear stationary periods are due to the fact that zero crossing of the electric field doesn't contribute to any energy transfer.

Optical excitations induce time dependent electronic polarization in medium. The temporal variation of the electric dipole generates radiation [19]. If we can measure the electric field of this radiation, we can understand the dynamics of these dipoles. Since each dipole excitation has a unique characteristic, such time-resolved measurements lead to time-resolved spectroscopy. Time-resolved spectroscopy not only provides spectral information of the system under the study but also, sheds light on the time scale of different dynamics. One way to perform time-resolved spectroscopy is through the time-resolved measurement of the electric field. An overview of the different measurement techniques that can provide sub-cycle information is given in the following sections.

## 1.1. Overview of different measurement techniques

In the past decade, advancements in the generation of tailored carrier-envelope-phase (CEP) stable ultra-short electromagnetic transients [20], have enabled a variety of techniques for the measurement of the electric field of light. For two decades attosecond streaking served as the cornerstone of the time-resolved measurement of the electric field of light [21, 22, 15]. But this method suffers from a low signal-to-noise ratio as a result of a time-consuming measurement technique. In a nutshell, an isolated extreme ultra-violet (XUV) pulse creates an electron wave packet, with a final group velocity that is modulated by the vector potential of a delayed IR light transient at the moment of electron ionization. Measuring the final velocity of these electrons gives temporal information about the electric field of the light transient [23]. The short

nature of the photo-ionization inherent in the XUV photons results in a large measurement bandwidth. But this comes with a number of complications:

1. Measurement of the final velocity of the electrons is achieved using time of flight spectroscopy. As a result, this technique doesn't have a high signal-to-noise ratio (SNR).<sup>2</sup>
2. The final velocity is proportional to the vector potential of the electric field of light which is intended to be measured. Since in frequency-domain  $A(\omega) = iE(\omega)/\omega$ , the technique doesn't have sensitivity for high frequencies.
3. The measurement has to be done in strongly evacuated chambers (order of magnitude  $10^8$  mbars of vacuum). This makes the method expensive.
4. The ionization cross-section for XUV photons is low. Furthermore, the angle of acceptance of electrons into the time-of-flight spectrometer (TOF) is small. As a result, counts of detected electrons in the TOF are low. Therefore, a long integration time is needed to scan the entire electric field of an optical transient. This is achieved only when a laser system can stay stable over a long period of time.

These shortcomings of attosecond streaking motivated researchers to invent new methods[30, 35, 32, 37]. All these methods have one thing in common—an ultra-fast excitation as a gate followed by a delayed probing pulse whose electric field is intended to be measured. The majority of these methods use nonlinear interactions as gating mechanisms since nonlinear excitations are generally faster than linear excitations [24].

Mathematically, the measured signal  $S(\tau)$  is a convolution of the gating function  $G(t)$  and the time-dependent quantity under the study  $q(t)$ :

$$S(\tau) = \int_{-\infty}^{\infty} q(t) \times G(t - \tau) dt \quad 1.1$$

In an ideal case, the  $G(t)$  is Dirac's delta function. Therefore, the signal will be the exact value of the quantity at the moment of the sampling:

$$S(\tau) = \int_{-\infty}^{\infty} q(t) \times \delta(t - \tau) dt = q(\tau) \quad 1.2$$

Depending on the measurement technique, the gating function either couples to the electric field  $F(t)$  or to the vector potential of the field which in SI unit is<sup>3</sup>:

$$A(t) = \int_t^{\infty} F(t') dt' \quad 1.3$$

In the rest of this chapter, a review of the variety of techniques that use nonlinear interactions as their gating for the sampling of the electric field of ultra-short pulses is presented. The comparison is provided on how the order of nonlinearity and the way that respective interaction couples with the electric dipole of sampling medium will play a role in the sensitivity and the bandwidth of measurement of each sampling technique.

The lowest nonlinear order is the second-order nonlinearity. The nonlinear electric dipole is created by wave mixing of two electric fields. Electro-optic sampling (EOS) uses this order of nonlinearity to measure the electric field. This method was invented by Gérard Mourou [25, 26, 27]. Here we have two pulses, an ultra-short pulse which is traditionally called the sampling pulse and the longer pulse to be measured which is

---

<sup>2</sup> The limits of SNR of attosecond streaking are described in section 2.2.1

<sup>3</sup> In absence of magnetic field

called the test pulse. The sum-frequency generation (SFG) and the difference frequency generation (DFG) of the pulses up-convert the spectrum of the test pulse. These SFG or DFG then spectrally overlap with the upper or lower part of the spectral window of the sampling pulse respectively. The electric field of this overlap region is called the local oscillator. As a result of the interference between the local oscillator and the SFG or DFG, a beat signal is generated. If the local oscillator is very short with respect to the test pulse the beat signal will be proportional to the electric field of the test pulse at the moment of the delay between test and sample pulse [28]. To remove the background signal from the local oscillator a balanced detection method is used. In the terminology of this thesis, the sampling pulse is given by the injecting pulse and the test pulse corresponds to the drive pulse.

EOS or any method like this that uses a nonlinear crystal to mix gate the drive pulse nonlinearly has to have a large phase-matching bandwidth, which is limited by the finite crystal thickness necessary for efficient nonlinear processes. Another key aspect that limits the bandwidth is the required overlap of the spectrum of the SFG/DFG pulse with the sampling pulse. In the case of high-frequency components of the test pulse, part of the SFG signal will not overlap with the local oscillator and therefore cannot be measured. The highest detection bandwidth in EOS has been demonstrated by Ridente et al. [29] who could show that by shortening the time duration of the sample pulse toward 2.5 fs, radiation up to 0.5 PHz can be resolved.

There are numerous ways to use nonlinear interactions that don't require phase matching. In these methods nonlinear absorption provides the gate in which the electric field that we want to measure, which has a delay with respect to the nonlinear injecting field changes the final state of the electronic wave function created by nonlinear injection and this delay dependent change is measured. Some changes of final state are proportional to the electric field of driving field some are proportional to the vector potential of such field.

An example of the measurement techniques which the measured quantity is proportional to electric field of the sampling field has been achieved using a method called the tunneling ionization with a perturbation for the time-domain observation of an electric field (TIPTOE) [30, 31]. In this method, the injecting pulse is used for tunneling ionization in a gaseous medium. The sampling pulse, furthermore, modulates the tunneling probability of the electrons. This change in the ionization probability is measured by the electric current obtained from an electrode.

As was discussed, the signal in TIPTOE should be proportional to the number of tunneled electrons. But, studies have shown that the further acceleration of the tunneled electrons with the weaker probe pulse can contribute to the signal, in an effect called femtosecond streaking [32]. Furthermore, since we want to modulate the rate of tunneling ionization, we need to start with a high probability of tunneling ionization. The tunneling ionization is more probable at longer wavelengths [33]. Therefore, the gate pulse cannot have a short half cycle. This in return will limit the upper limit of the detected frequency. The highest frequency reported using this measurement technique is about 0.75 PHz [34].

Another approach that involves tunneling ionization is called the petahertz optical oscilloscope [35]. In this method, the injecting pulse is used to generate high harmonics. In a nutshell, the injection pulse causes the tunneling ionization of an electron, accelerates the electron away from the atom, and later accelerates it back toward the parent atom. As a result of the recombination of the electron with the parent ion, XUV photons are emitted. This excursion happens in a fraction of the sampling pulse's optical cycle. The sampling pulse can modulate the trajectory of this excursion and as a result, change the phase of the generated XUV photon. It has been shown that this phase change is proportional to the amplitude of the sampling pulse electric field at the moment of tunneling ionization.

In the petahertz optical oscilloscope, the XUV generation is perturbed in an angled geometry, where the sampling pulse and injecting pulse propagates with a relative angle with respect to each other. Therefore, each change in the XUV phase changes the direction of the generated XUV pulse and this change of angle

is linearly proportional to the phase change. Finally, the signal is obtained by looking at the angle change of the detected XUV spectra.

As was discussed before, phase matching limits the detection bandwidth of the electric field. The deflection angle of the XUV radiation is a result of phase matching; therefore, the highest detected frequency in the PHz optical oscilloscope did not exceed 0.6 PHz.

A reliance on phase matching and the need for angle-resolved XUV spectroscopy complicate the electric field measurements using the petahertz optical oscilloscope technique. While TIPTOE does not suffer from these shortcomings, it relies on the probability of tunneling ionization which favors longer wavelengths.

Although tunneling ionization in gases provides ultra-fast gating, it requires very intense laser pulses to enable strong-field ionization, due to the high ionization potential for commonly used noble gases. Another way to access short gating times can be achieved by nonlinear photoconduction in large bandgap materials. In a method called nonlinear photoconductive sampling (NPS). Since this method will not deal with electron counting or XUV spectroscopy it doesn't require a vacuum chamber, which makes it tabletop. On the other hand, the complications due to tunneling ionization are solved since the gating happens due to multi-photon absorption. As will be discussed in more detail in the next section, this method can overcome many of these shortcomings and it is a suitable technique for the measurement of the electric field of ultra-short optical transients.

## 1.2. Nonlinear photo-conductive sampling

In the past, field-effect transistors have been used to sample electric fields up to 100 GHz [3]. As mentioned above, ultra-fast photoexcitation followed by Auston switch sampling can push the bandwidth of solid-state measurements towards the multi terahertz region [9]. In the mentioned experiments, the solid-state switch is made out of a semiconductor. The bandgap of these materials does not exceed 1 to 1.5 eV. The radiation that linearly photo-excites the carriers in these materials has the half-cycle time of 2.06 fs. If this radiation has only one half-cycle, then the highest frequency that we can resolve is roughly 0.241 PHz.

Therefore, it was proposed that instead of small bandgap materials, large bandgap materials can be used [36]. Also, to confine the photoexcitation to an even shorter time scale with respect to the normal optical half-cycles, nonlinear photoexcitation should be employed; therefore, the proposed method was called nonlinear photoconductive sampling.

In this method, a strong few-cycle CEP stable transient injects charge carriers to the conduction band (CB) of a large bandgap material (for example  $\text{SiO}_2$ ,  $E_{\text{gap}} = 9 \text{ eV}$ ). Furthermore, these carriers will be driven by a delayed pulse with orthogonal polarization with respect to the injecting pulse. In crude classical picture as a result of acceleration of electric charges that are suddenly born in an external electric field the charge carriers will obtain final velocity. As result of this velocity the electron hole pair that are created by nonlinear injection will drift away from each other which will create an asymptotic electric dipole, the electric field of this dipole screens some charges on external electrodes. The studies have shown that the detected delay-dependent currents have a temporal form similar to the vector potential of the driving field [37] (another example of a method where the real part of the induced dipole moment is modulated by the field).

The ultra-short injection time provided by the strong nonlinear nature of the photo injection in  $\text{SiO}_2$ , resulted in an unprecedented extension of the detection bandwidth in NPS. For a few-cycle titanium doped sapphire

(Ti:Sa) laser system (1 mJ, 300 KHz, 4 fs, 780 nm, 1.57 eV), nonlinear photo-conduction in SiO<sub>2</sub> requires 4 photon injection<sup>4</sup>. The gate function for this injection can be approximated by [37]:

$$G(t) = F_{\text{inject}}^8(t) \quad 1.4$$

Here,  $F_{\text{inject}}(t)$  is the electric field of the laser pulse. Therefore, the detected current in the case of the NPS SiO<sub>2</sub> using an 800 nm pulse is:

$$S(\tau) = \int_{-\infty}^{\infty} A_{\text{drive}}(t) \times F_{\text{inject}}^8(t - \tau) dt \quad 1.5$$

Here  $A_{\text{drive}}(t)$  is the vector potential of the field that is to be detected. Since the integral in Eq. 1.5 is a convolution integral, the spectrum of the recorded signal,  $S(\omega)$ , is the product of the spectrum of the vector potential of the drive pulse,  $A(\omega)$ , and the spectrum of the gate,  $G(\omega)$ :

$$S(\omega) = A(\omega) \times G(\omega) \quad 1.6$$

Figure 1.3.b shows the spectral response  $G(\omega)$  of the pulse shown in figure 1.3.a. As can be seen in figure 1.3.c, the sensitivity of the measurement, for frequencies above 1.75 PHz (~6 eV, ~190 nm), drops below 20% of the maximum value. The minima in the spectral response are the result of the injection spikes left and right of the main spike in figure 1.3.b. Sederberg et.al have shown experimentally that using this technique they can sample up to 1.1 PHz in normal atmospheric pressure [37]. Detection of higher frequencies is impossible since air will absorb any radiation above 1.2 PHz [38].

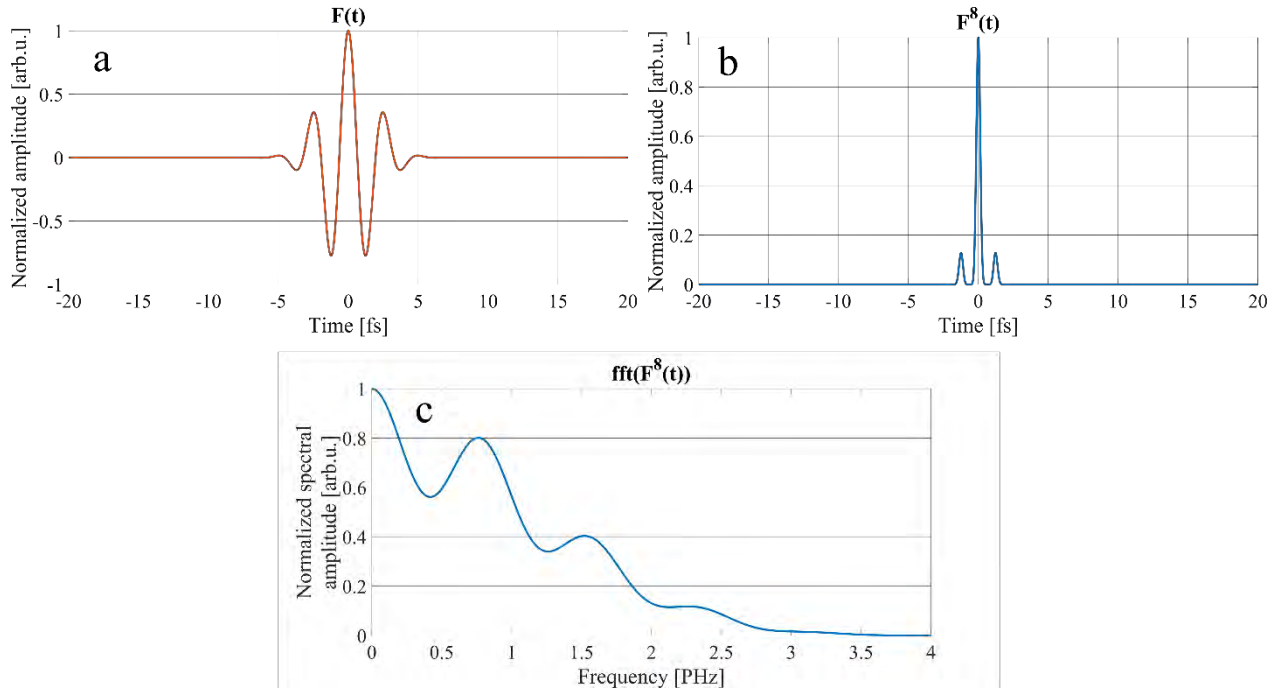


Figure 1.3. a) The electric field of the injecting pulse. b) The gate function for  $F_{\text{inject}}^8(t)$ . c) The absolute value of the Fourier transform of the  $F_{\text{inject}}^8(t)$ .

<sup>4</sup> This 780 nm pulse is so broadband that 550 nm part of it can do the 4 photon injection.

The sample geometry of the NPS is very simple. For example, one can take a normal piece of silicon dioxide wafer, put two electrodes over it and shine the inject and the delayed drive pulse on it. There is no need to use a vacuum system. This is much simpler in contrast to TIPTOE where the signal is dependent on the electron counts this will set a constraint on the geometry of the electrode.

The strong field interaction of the injecting field provides a far better sampling of the electric field of ultra-short optical transients in comparison to similar techniques (i.e. TIPTOE and petahertz optical oscilloscope), however at same time this strong field prevents full decoupling of the injecting and the driving step. This means that both steps can influence the other step.

The first problem is that the nonlinear injection depends on the amplitude of the total electric field. Figure 1.4 depicts all the existing fields in NPS. The total electric field consists of two electric field contributions, the injecting field, and the driving field, and it is the total field that injects carriers into the conduction band. The following simple example can help us understand how small changes in the total field amplitude can change the carrier injection probability:

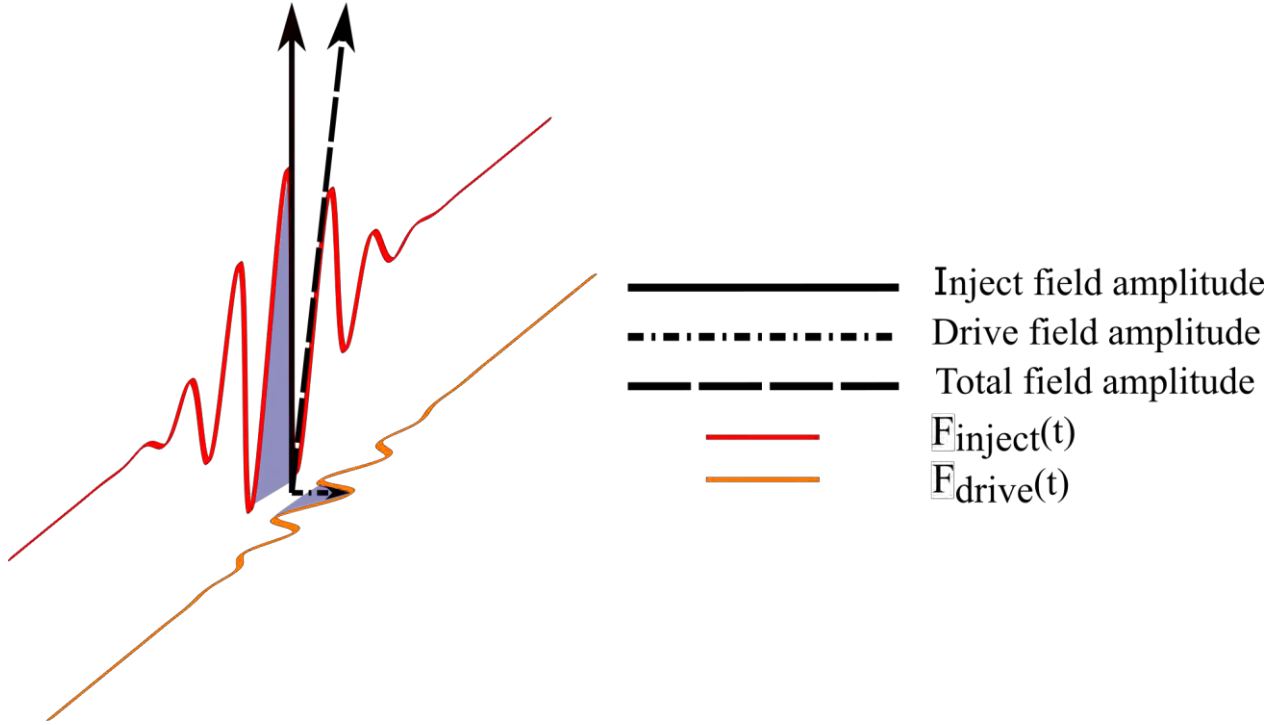


Figure 1.4. Depiction of the fact that actual nonlinear photo-injection is the result of the total electric field. The red curve is the intended injecting field; the orange curve is the intended driving field. Shaded areas depict the time extend when we expect that the injection should happen in the injecting field. The solid arrow shows the direction and the amplitude of the injecting field; the horizontal dashed line is the depiction of the direction and the amplitude of the driving field; The oblique dashed line depicts of the direction and the amplitude of the total field that eventually nonlinearly injects the carriers to CB.

Consider that, two orthogonally polarized laser pulses that propagate along the z-direction exist, whose electric fields are defined as follow:

$$\vec{F}_{\text{inject}}(t) = F_0(t)\hat{x}\cos(kz - \omega t) \quad 1.6.a$$

$$\vec{F}_{\text{drive}}(t) = 0.1 \times F_0(t)\hat{y}\cos(kz - \omega t + \omega\tau) \quad 1.6.b$$

where  $F_0(t)$  is the temporal field envelope of the inject field and  $\tau$  is the delay between injecting ( $\vec{F}_{\text{inject}}$ ) and driving ( $\vec{F}_{\text{drive}}$ ) fields.  $F_0(t)$  can be written as:

$$F_0(t) = af(t) \quad 1.7$$

where  $a$  is the maximum envelope amplitude and  $f(t)$  is a distribution function normalized to unity, for more simplicity, we can choose it to be Gaussian, but in general any form of this function will not change the result of our analysis.

Let's assume that only the strongest half cycle of the injecting field is responsible for the carrier injection. Depending on the inject/drive delay ( $\tau$ ), we shall have the following cases for the maximum and minimum amplitude of the total field:

$$MAX(A_{tot}) = \sqrt{A^2 + \left(\frac{A}{10}\right)^2} = A\sqrt{1.01} \quad 1.8.a$$

$$MIN(A_{tot}) = A \quad 1.8.b$$

For the case of injection in  $\text{SiO}_2$  with 1.57 eV pulse (4 photon absorption) the transition probability scale with  $A_{tot}^8$ , which in the maximum case will be  $A^8 \times (\sqrt{1.01})^8 = A^8 \times 1.04$  and in case of the minimum is  $A^8$ . As you can see, we can change the injection probability by 4 percent. The situation is worse if we have higher bandgap material like LiF (13 eV), (in this case with 6 photon absorption for 1.57 eV inject pulse) we can change the injection probability by 6 percent. Therefore, NPS suffers from the fact that the probability of photo-injection changes by delaying the injecting and the driving pulse.

Another problem is that after carriers are promoted to CB they still experience the existence of the strong field. Although choosing orthogonal polarization for the injecting and the driving field ensures that the injecting will not drive the carriers in CB, it still can facilitate the transition of the carriers to the upper bands (Figure 1.5). As a result the initial population of carries in the CB is will be unknown. The created electronic occupation can be dispersed throughout the Brillouin zone and distributed over several conduction bands<sup>5</sup>

---

<sup>5</sup> We shall explain in section 4.2 why the dispersed population in various CBs will prohibit a one-to-one mapping between optical and electronic signals and their coupling to external circuitry.

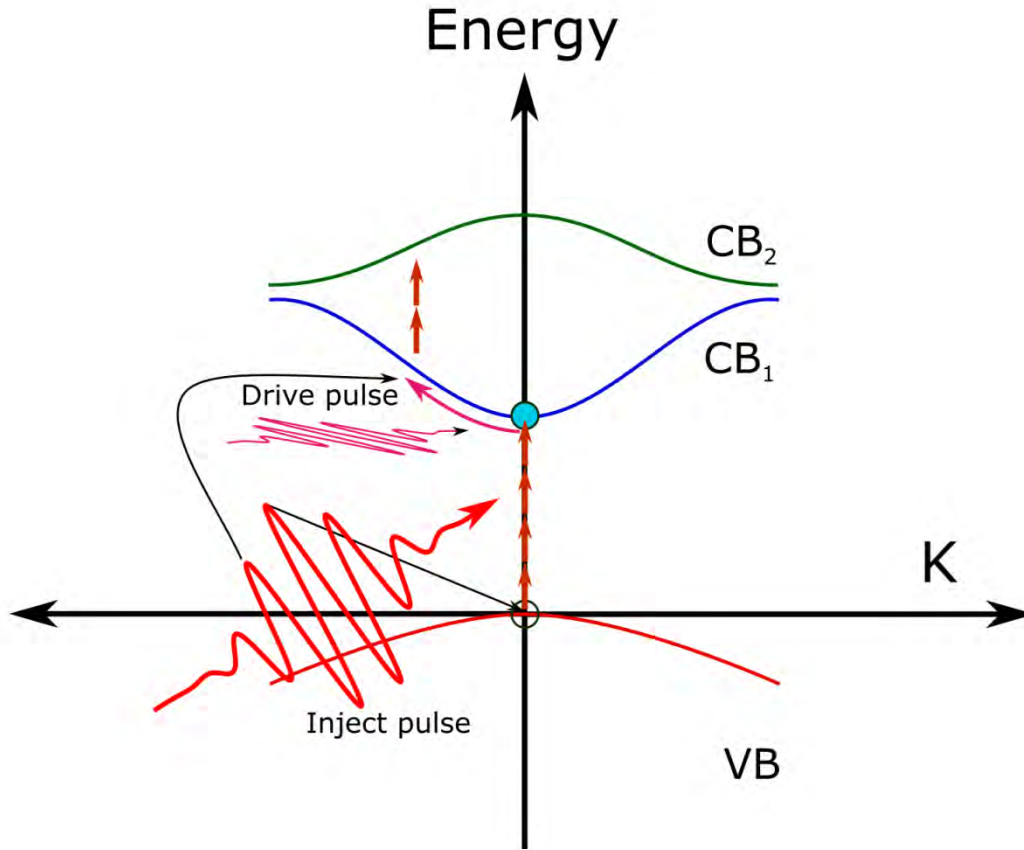


Figure 1.5. Depiction of complications of nonlinear carrier photo-injection in NPS.

Another problem is that if according to Eq. 1.1, for the full reconstruction of the driving pulse we must have a perfect characterization of the injecting pulse unless the central half cycle of the injecting pulse is dominant enough that only one instance of photo-injection matters. While we can get some information about the nature of the photo-conduction process by recording the CEP dependent current, a complete understanding of this step requires two-foci experiments, wherein one plane of focus a delayed inject and drive measurement is performed and in the second plane of focus the changes in the electric field of the injecting and the driving pulse in each delay is measured. Since these measurements have to be repeated for all delays between the inject pulses versus the drive pulse, performing such measurement can give us unprecedented information about the dynamics of injecting and driving but also is very time consuming and cumbersome<sup>6</sup>.

The complexities that are mentioned up to now can be resolved if we introduce a simpler way of injection, that decouples the injection and the driving step completely. One way to achieve cleaner injection is to transfer carrier population to the CB of large bandgap materials employing ultra-short linear injection. In contrast to nonlinear injection, linear can be controlled using bandwidth selection, and consequently, single-photon injection permits the homogeneous exhaustion of the full energy spread of individual energy bands (please refer to section 4.2). A Bloch wave that is created through this linear injection is steered by means of a secondary optical delayed transient. Because the source of this carrier injection is linear, it can switch on the conductivity in the medium on the 1 fs time scale (please refer to section 4.5). We call this method

<sup>6</sup> More information about these kinds of two foci measurements can be found in the doctoral thesis of the Dmitry Zimin [39]

linear petahertz photoconductive sampling (LPPS). It will be shown that due to the nature of the injection, the linear injecting field cannot create any ultra-fast current in the medium. As a result, the need to use orthogonally polarized geometry for the inject/drive measurements is removed. The main focus of the current thesis is to provide such a solution and scrutinize further dynamics that arise from the ultra-fast control of the charge carriers. In the next chapter, we shall discuss current benchmarking techniques for the full characterization of the electric field. Furthermore, we shall discuss the replacement source of injection, and finally, we shall talk about the theory of the charge carrier optical driven dynamics.



# 2. Theoretical background

In the previous chapter, it has been discussed that ultrashort linear injection of carriers in CB of large band-gap materials provides a better understanding of ultrafast light-driven carrier dynamics. While nonlinear injection offers the ultra-short time scale for photo-carrier injection, it will create an electronic wave-packet that is dispersed over multiple bands in the CB which brings uncertainty on the understanding of the initial state of the injected electronic wave-packet. Because of this complication, if the carriers are promoted to CB in a controlled linear fashion, a better understanding of ultra-fast light-driven currents is established. This injecting source should have enough photon energy to trigger electronic transitions from VB to CB of these materials and have large bandwidth to ensure the fast transition. One way to create radiation with such characteristics (High photon energy, temporally short) is called High Harmonics Generation (HHG).

In this chapter, first, we will have a quick review of the process of the HHG as a source of linear photo-injection in large band-gap materials. Later on, we will discuss how electronic wave-packets promoted by linear photo-injection would evolve in time under influence of a secondary linear photo-drive. Additionally, one of the goals of this thesis is to introduce linear photo-conduction as a gating source for field sampling. Since any field sampling method requires benchmarking versus a standard method, another part of this chapter will focus on attosecond streaking as the cornerstone method of measuring the electric field of light. We will discuss all its capabilities and shortcomings as a method of time-resolved field measurement.

## 2.1. High harmonic generation

When an ultra-short strong electric field is focused on a gas target, it will create a train of high-energy photon bursts that can have energies that extend to the extreme ultraviolet region<sup>7</sup> and beyond<sup>8</sup>. The spectra of these high-energy photons are spaced by twice the energy of the ultra-short pulse. At first one might think that the generation of these higher harmonics can be explained by perturbative nonlinear light-matter interaction. But the change of intensity of these higher harmonics does not follow perturbative prediction. In the perturbative framework, we don't consider that the external field is strong enough to change the Hamiltonian of the Coulomb interaction between electrons and the nuclei. But in this case, the strong electric field distorts the Coulomb potential of a neutral atom (figure 2.1). The bending of the potential well (dashed green curve in figure 2.1.a) enables the electron to tunnel out the potential well. This tunneled electron is born with zero average velocity [42]. After the tunneling ionization, the strong electric field accelerates this electron away from the atom until the sign of the field changes. Afterward, the electron decelerates while moving away from the atom till it stops and again accelerates back toward the parent atom [43, 44].

At the moment of recombination, the electron has kinetic energy acquired by the acceleration in an external field. As a result of recombination with the parenting ion, a photon is released which has the final kinetic energy of the electron plus the ionization energy of the atom. It can be shown [45] that, the maximum classical energy from this three-step model equals to<sup>9</sup>:

---

<sup>7</sup> Bandwidth within 10 eV to 124 eV is called extreme ultra violet.

<sup>8</sup> keV HHG photons have been reported by extreme intense laser pulses with intensities around  $I \approx 10^{16}$  W/cm<sup>2</sup>[40, 41]

<sup>9</sup> This relation does not take into account the quantum effects. There are photons whose energy supersedes this limit, but the flux of these photons falls rapidly above this cutoff limit.

$$E_{\max} = I_p + 3.17 \times U_p \quad 2.2a$$

$$U_p = \frac{e^2 F_a^2}{4m\omega_0^2} \quad 2.2b$$

where  $I_p$  is ionization energy,  $e$  is electron charge,  $F_a$  the maximum electric field amplitude of the external field,  $m$  the mass of electron and  $\omega_0 = 2 \times \pi/T_0$  is the electric field carrier angular frequency ( $T_0$  is period of one cycle of external field).  $U_p$  is called ponderomotive energy, which is the energy of quiver motion of a free electron in an external field averaged over one cycle [46].

The tunneling ionization can happen in each strong half cycle of the external field. Therefore, we shall have these strong bursts every half cycle. Since the generation of these photons occurs every half cycle of the external field  $T = T_0/2$ , where  $T_0$  is period of the field, then the frequency of the generated harmonics are spaced by  $\Delta\nu_0 = T_0/2 = 2\nu_0$ . So, the energy spacing of these photons is twice the energy of the carrier wave of the external field.

We described 3 steps in the generation of higher harmonics photons: 1) tunneling ionization, 2) electron round trip, and 3) recombination. These steps play different roles in the yield and energy of these high-harmonic photons. The energy of these photons is affected only by the first and second steps while their yield is affected by the first and third steps. [47].

The probability of tunneling ionization depends on the magnitude of the external field amplitude [48]. A stronger field bends the Coulomb potential more. As a result, an electron sees a thinner potential barrier to tunnel through, which leads to a higher probability of tunneling (figure 2.1.b).

As result of tunneling ionization, the electronic wave function will be a combination of a bound part and a free propagating part [49]:

$$\psi(t) = |G(t)\rangle + |\varphi(t)\rangle \quad 2.3$$

where  $|G(t)\rangle$  is the time-evolved bounded state wave function and  $|\varphi(t)\rangle$  is the free-electron wave packet that is propagating inside the external field (these states can be written as a superposition of Volkov states [50, 51]).

Since the wave function has two terms, the created dipole has an interfering part between the tunneled and the bound part of the wave function. Oscillations of this dipole moment are causing the radiation. We can write the dipole moment expectation value as follows:

$$\langle \mathcal{D}(t) \rangle = e \langle \psi(t) | \vec{x} | \psi(t) \rangle \quad 2.4$$

$$\langle \mathcal{D}(t) \rangle = e \langle G(t) | \vec{x} | \varphi(t) \rangle + c. c. \quad 2.5$$

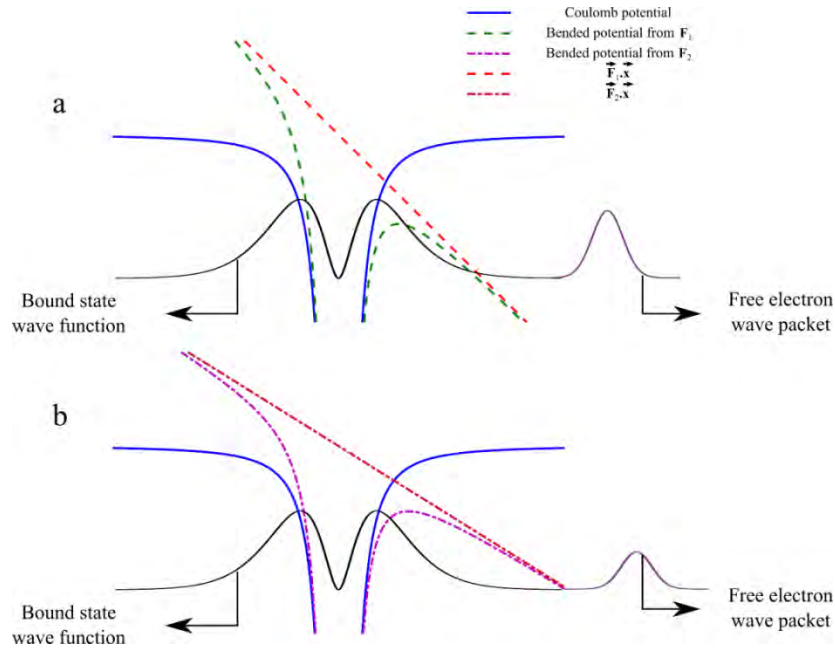


Figure 2.1. The Coulomb potential of the neutral atom (blue curve) is bent (green dashed curve) by the external electric field, the interaction is depicted in length gauge (red line indicates the dipole interaction of the external electric field with an atom). As a result of this barrier bending part of the wave function of the bounded electron (black function) is tunneled out (violet wave packet). The effect of the strength of the electric field on the probability of the tunneling ionization can be seen by the comparison made in a) stronger electric field  $E_1$  bends the Coulomb barrier more. b) The weaker electric field  $E_2$  bends the barrier less. The less tunneling length leads to the higher probability of tunneling.

The second time derivative of the term  $\langle G(t) | \vec{x} | \varphi(t) \rangle$  and its complex conjugate are responsible for the radiation of these photons [52]. If  $|\varphi(t)\rangle$  has a large spatial spread, the resulting integrals in Eq. 2.5 will be very small [53]. The electron wave function is a composition of many plane waves with different momentum. In free space, the faster components of the wave-packet will travel more than the slower parts. That is why longer propagation results in more spread of the wave-packet over free space [54]. This diffusion of the wave packet reduces the chance of recombination [55]. The bound part of the wave function is localized; therefore, the large spatial spread of the free-electron wave packet reduces the spatial overlap with the bound part, which in return reduces the amplitude of the dipole integral. If we start with a larger atom, the initial tunneled wave packet is larger. A large spread in space means a smaller spread in momentum, which in return reduces the spatial spread of the wave packet during the propagation, which increases the recombination probability for larger atoms [56]. The length of the round trip depends on the moment of tunneling. If tunneling happens near the extremum of a half-cycle, an electron sees a stronger electric field it will accelerate further away from the ion, which in return reduces the probability of electron recombination; this means that electrons with higher kinetic energy have a smaller chance of recombination<sup>10</sup>.

The final kinetic energy of the electron following one round trip depends on the moment of tunneling ionization [57]. Considering electrons that are born in one half-cycle of the electric field (let's call this half-cycle as birth half-cycle), those that are born near the zero-crossing of the electric field before the extremum of the birth half cycle can experience more accelerating time than those which are born later. These electrons will travel farthest. The one that is born before the extremum of the birth half-cycle will never return to the

<sup>10</sup> It should be noted that also just like any scattering cross-section, the recombination cross-section decreases starting from a certain kinetic energy.

parenting atom. Because, right before they can return to the atom by the next half-cycle the sign of the electric field changes, and again, they travel away from the atom. Returning to the atom is only possible for those electrons which are after the extremum of the birth half-cycle<sup>11</sup>. Moving away from the extremum the length of the round trip to the atom starts to decrease. The final kinetic energy of the electron will first start to increase and then after a certain point, it decreases again. The reason for the initial increase of final kinetic energy is that when the moment of tunneling is moved away from the extremum the time duration in which returning half-cycle accelerates this electron back to atom increase. Hence final kinetic energy increases. But also, by moving away from the extremum we will decrease the length of the electron excursion, since the tunneled electron experiences a weaker electric field, which in return results in the reduction of the final velocity of the returning electron. Therefore, the electron energy will start to decrease again. As a result, HHG spectra from each half cycle have two sets of energy distribution. They are distinguished by the length of their round trip. One set is called a long trajectory and the other is called a short trajectory. Since the moment of tunneling ionization plays an important role in the final kinetic energy of the corresponding electron, HHG photons will have an inherent chirp, which is negative.

In the case of long trajectories, if the corresponding electron tunnels out when the electric field has a stronger amplitude, it will experience a narrower potential barrier, thus, the ionization probability is more. On the other hand, electrons that are born near the stronger field amplitude will travel more, thus, the recombination probability is lower. For the case of short trajectories, since tunneled electrons experience weaker field amplitude, they experience larger potential barriers and consequently, they will have a shorter round trip (i.e. lower tunneling and higher recombination probability). Therefore, in a certain span of HHG spectra, there will be a balance of tunneling and recombination probability. As a result, the intensity of HHG photons in this span remains almost constant. This region is called the plateau region [58, 59].

In addition to the moment of tunneling, the amplitude of the neighboring next half-cycle affects the final magnitude of the kinetic energy of the electron [60, 61]. If the neighboring half-cycle has a stronger electric field than the tunneling half cycle, during the time that electron accelerates back, it will experience a stronger electric field than the moment of tunneling. Thus, the final kinetic energy of the electron increases. As a consequence, electrons with the highest final kinetic energy are those born in the half-cycle before the strongest half cycle of the external field. In the case of a pulse with  $CEP = 0$  which is also called a cosine pulse, there is only one half-cycle that can provide these electrons with such final kinetic energy. Therefore, there is no modulation of HHG spectra in this region. This region is called the cutoff region [62]. In case of the pulse with  $CEP = \pi/2$  which is called a sine pulse two half cycles can provide electrons with the same final kinetic energy and as a result the cutoff region becomes modulated. The photons from the cosine pulse have the highest cutoff energy and those from the sine pulse have the highest harmonic yield (figure 2.2)

There is also a third region harmonics spectrum. The energy of these photons is lower than those of the plateau region. Harmonic generation within this region is not well described by the three-step model and simple multi-photon transition also falls short to describe the generation of such photons [63]. These photons have energies below the ionization energy of their parent atom.

The fact that a cosine pulse can create HHG photons that have no equivalence in the neighboring half-cycles helps us to isolate HHG pulses in time [64]. Applying a high-pass spectral filter to the HHG pulse train will ensure the transmission of HHG spectra that are generated from the electrons that belong to the cutoff region. As a result, we shall have a single short burst of HHG photons. Although we have lost the bandwidth of radiation by spectral filtering, which means temporal stretching of the pulse, choosing the right thickness

---

<sup>11</sup> The reader should remember that we are only talking about one half-cycle. So, if we state that the return is only possible after extremum, we are only talking about the event which takes place in one half-cycle. For sure if we go further to the next half-cycle between the zero-crossing till just before the extremum of that half-cycle there will be no return to atom.

for the HHG filter will compensate for the inherent negative chirp of the HHG pulse, which can compress the pulse. Using this filtering technique, we can generate HHG bursts below 80 as [65].

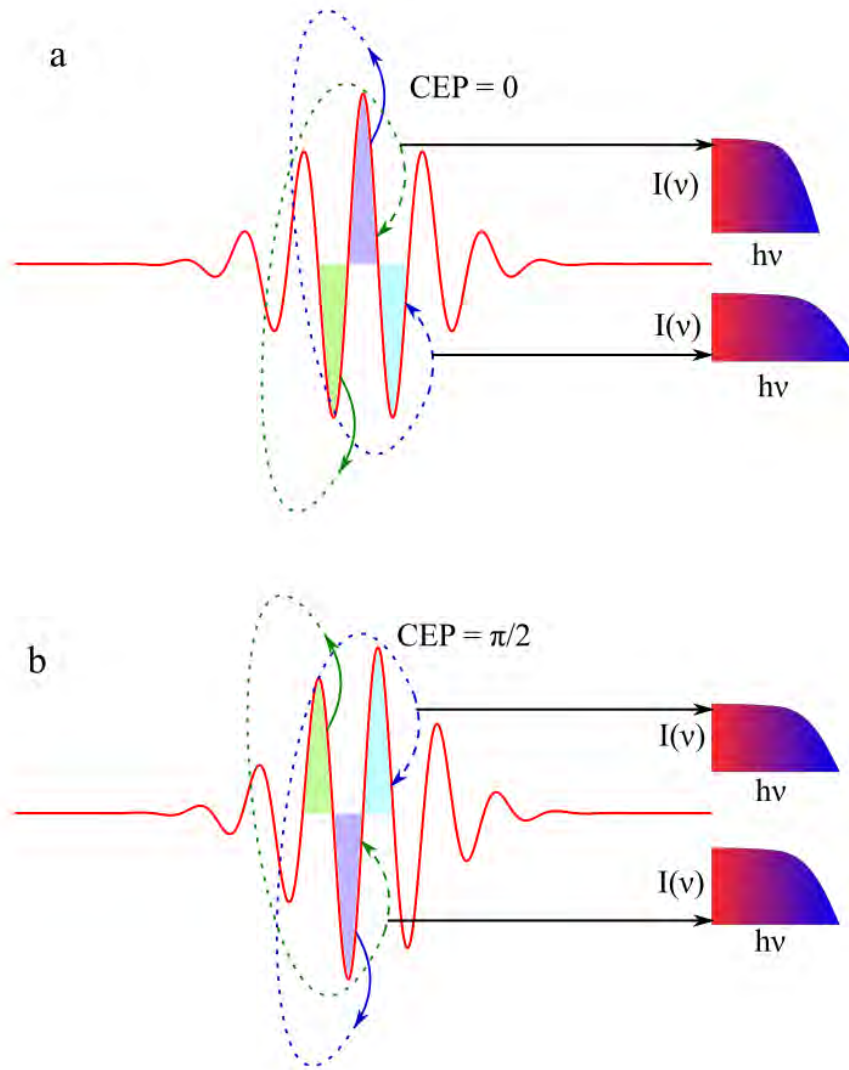


Figure 2.2. Comparison of the effect of CEP on the cutoff energy and the yield of harmonics. Shaded areas under the half cycles denote part of the electric fields that accelerate the electrons back toward the parent ion. a) Cosine pulse: The green half-cycle ionizes electrons that are returned with the violet half cycle (i.e. the green trajectory). Since the violet half cycle is the strongest half cycle the final kinetic energy of the electrons is the highest, but since the electrons didn't tunnel out at the strongest half cycle the harmonics yield is not the largest. On the other hand, if the violet half-cycle ionizes the electrons the blue half-cycle returns them to the atom. Here the strongest half-cycle ionized the electron therefore we have the highest harmonics yield but we don't have the highest energy of XUV photons. b) Sine pulse: violet and blue half-cycle have the same amplitude, therefore any electron that is driven back by these two half-cycles has the same final kinetic energy. Electrons that are ionized in the violet half-cycle have a higher yield than the electrons which are ionized from the green half cycle; therefore, we shall have two half-cycles with same cutoff energy but one has a higher yield than the other one (higher yield XUVs are depicted in the upper plot in the inset of b and lower yields are the lower plot in the same inset)

These ultra-short high-energy pulses allow us to characterize the electric field of optical pulses. In the next section, we will talk about a method that incorporates these radiations as injection sources for the detection of the few-cycle optical transients.

## 2.2. Attosecond Streaking

In this section, we will talk about the most prominent technique for electric-field measurements of optical transients, which is called attosecond streaking.

If a free electron interacts with the entire temporal electric field of an electromagnetic pulse, the field cannot transfer any momentum to the electron [66]. This is because, for propagating laser pulses, the integral of the electric field over time is zero:

$$\int_{-\infty}^{\infty} F(t) dt = 0 \quad 2.6$$

To have a net momentum transfer, an electron has to be born during a pulse. In that case, the net transfer momentum is:

$$P_{\text{transfer}} = -e \int_{\tau}^{\infty} F(t) dt \quad 2.7$$

Where  $e$  is the elementary charge and  $\tau$  is the moment in time when the electron is born inside the electric field.

One way to fulfill such conditions is to release the electron in an ultra-fast manner into a pulsed electric field. XUV photons with pulse durations around couples of hundreds of attoseconds, provide us with such opportunity. They can ionize atomic systems and the generated electronic wave-packets by such ionization have the temporal structure of these XUV photons.

In attosecond streaking, the creation and time evolution of the electronic wave-packet happens in a two-color scheme. An ultra-short XUV pulse and a delayed optical transient will interact with an atom (mainly an inert gas). Due to the ultra-short ionization-time provided by XUV photons, Eq. 2.7 can be used to predict the average final momentum of the created electronic wave-packet [67], if  $F(t)$  is the electric field of the optical transient and  $\tau$  is the delay between the XUV (we shall call this inject pulse) and optical transient (we shall call this pulse the drive pulse).

Let's consider a case, where the delay of the injecting pulse versus the drive pulse is equal to  $\tau$ . Assume that these two pulses are focused onto a jet of an inert gas (e.g., argon or neon, which have ionization energies of 15.75 eV and 21.56 eV, respectively). The initial kinetic energy of ionized electrons is:

$$T_0 = h\nu_{\text{XUV}} - I_p \quad 2.8$$

here  $h$  is the Planck constant ( $h = 6.62 \times 10^{-34} \text{ m}^2\text{kg/s}$ ),  $\nu_{\text{XUV}}$  is the frequency of the ionizing XUV photon and  $I_p$  is the ionization potential of the inert gas.

Since these electrons were released with a delay  $\tau$  to the drive pulse, the final velocity becomes:

$$V_{\text{final}} = \frac{1}{m_e} \times \left( V_{\text{initial}} - e \int_{\tau}^{\infty} F(t) dt \right) \quad 2.9$$

where  $m_e$  is the mass of the electron ( $9.1 \times 10^{-31} \text{ kg}$ ) and  $V_{\text{initial}} = \sqrt{2m_e K_0}$  is the initial velocity of the electron.

The integral in the right-hand side of Eq. 2.9 is the vector potential of the pulse at the moment of  $\tau$ , therefore:

$$V_{\text{final}} = \frac{1}{m_e} \times (V_{\text{initial}} - eA(\tau)) \quad 2.10$$

From Eq. 2.10, we realize that the measurement of final velocity is equivalent to the measurement of the vector potential of the pulse at the moment of ionization. Therefore, measurement of the delay-dependent final velocity of these electrons would result in the full temporal characterization of  $\vec{A}(\tau)$ . If the delay  $\tau$  to  $-\infty$  or  $+\infty$  would get the information about the initial velocity of these electrons at the moment of ionization as well (since  $\lim_{\tau \rightarrow \pm\infty} \vec{A}(\tau) = 0$ ), as a result, the initial velocity of electrons is measured.

The solution for electron velocity measurement is offered by a kind of mass spectrometer that is called a TOF [68]. A basic TOF is a long vacuum tube of length  $L$  with an electron-sensitive detector. If an electron with velocity  $V_{\text{final}}$  enters the TOF and travels the length  $L$ , it takes an electron  $T = L/V_{\text{final}}$  seconds to reach the detector. The detector for the TOF is a micro-channel plate detector (MCP) [69]. Based on a triggering event (that we will call the zero-channel) the TOF will know when electrons were born. In a usual TOF experiment, a gas nozzle is placed close to the entrance of the TOF (figure 2.3), then from the moment of the triggering event, a timer starts to measure the time until the electron hits the MCP.

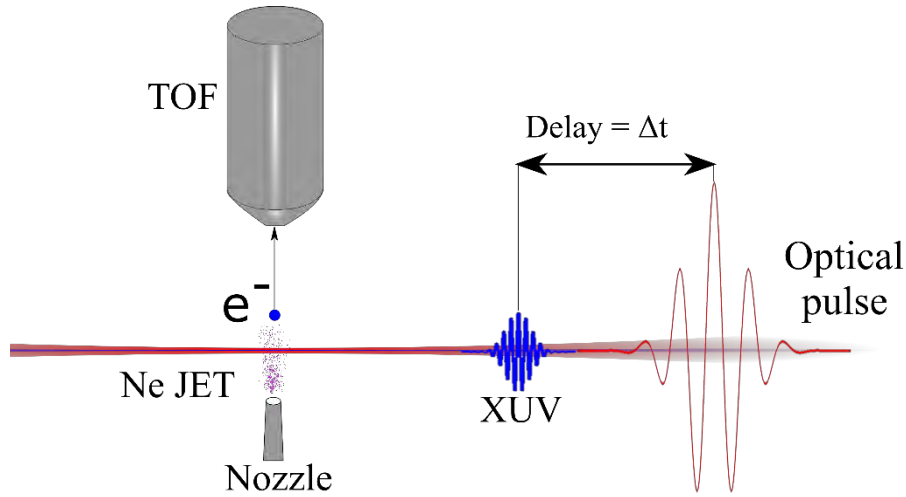


Figure 2.3. Schematic of the attosecond streaking measurement

By differentiating  $-A(\tau)$  with respect to  $\tau$ , we will get the delay-dependent value of the electric field of the drive pulse:

$$\frac{dA(\tau)}{d\tau} = -E(\tau) \quad 2.11$$

In the previous chapter, we mentioned that isolated XUV pulses can be generated by HHG and a high pass filter can be used to transmit cutoff harmonics. If we generate harmonics from argon (ionization energy  $I_p = 15.75$  eV) using a few-cycle NIR transient at 780 nm (4 fs, 800  $\mu$ J), and use a 150 nm aluminum/scandium (AlSc) filter, we shall have a bandwidth 10 eV centered at 60 eV. The Fourier limit of such bandwidth is about  $\Delta t_{\text{xuv}} = 140$  as. Because this time duration is short, the temporal structure of the XUV pulse will map directly to the temporal structure of the electronic wave-packet, even when these electrons are accelerated in the external electric field. Therefore, the detected signal by the TOF is a representation of the structure of XUV photons [70] (Figure 2.4).

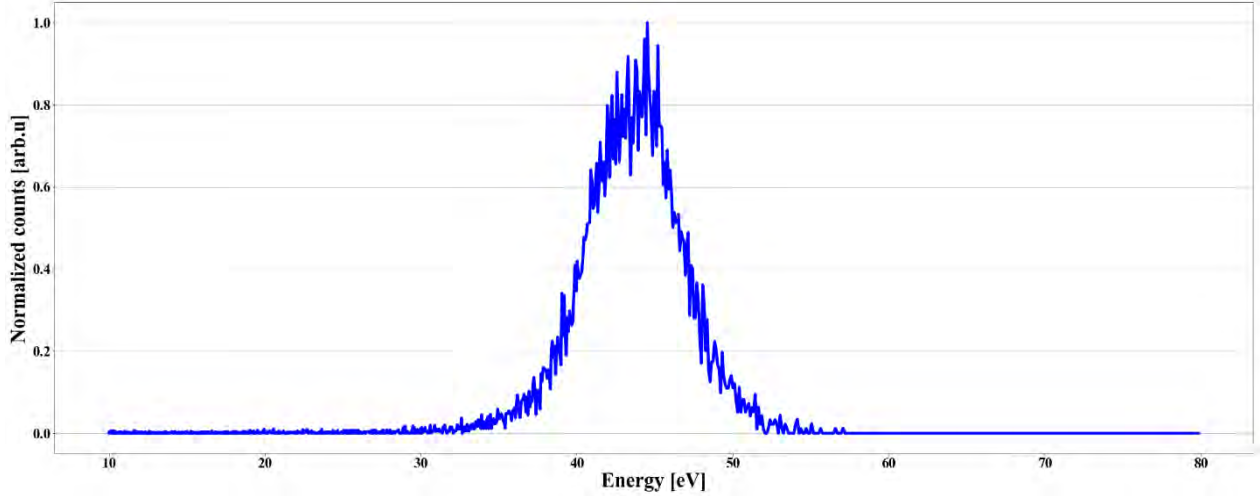


Figure 2.4. Normalized spectra of electrons detected by TOF, when we use AlSc as the XUV filter

By changing the delay between injecting and drive pulses, we will record a spectrogram of electrons. Since the average energy of each delay-dependent electron distribution is equal to the expectation value of the energy of the electron wave packet for each delay [71], i.e.:

$$\langle E_{\text{wave}} \rangle = \frac{\int_{E=0}^{\infty} N(E) E dE}{\int_{E=0}^{\infty} N(E) dE} \quad 2.12$$

The average energy of the electron spectrum is used to calculate the final velocity of the electron and finally, reconstruct the electric field of the driving pulse.

It can be shown that the quantum mechanical equation that describes the detected spectrogram is similar to the one that describes frequency-resolved optical gating (FROG) [72]:

$$S(p, \tau) = \left| \int_{-\infty}^{\infty} F_{\text{xuv}}(t) \times G(t + \tau) e^{\frac{ip^2}{2}t} dt \right| \quad 2.13$$

$$G(t) = \frac{D(p_0 + A_{\text{drive}}(t))}{D(p_0)} \exp \left( -i \int_t^{\infty} p_0 A_{\text{drive}}(t') + \frac{1}{2} A_{\text{drive}}^2(t') dt' \right) \quad 2.14$$

where  $F_{\text{xuv}}(t)$  is the temporal shape of the XUV field,  $D(p_0)$  is the transition dipole moment of the gas between initial bound state and final ionized state with momentum  $p_0$ , and  $A_{\text{drive}}(t)$  is the vector potential of the driving pulse. Therefore, if we perform a FROG retrieval algorithm on the spectrogram, we can characterize the XUV pulse as well.

### 2.2.1 SNR of attosecond streaking

Let's consider an XUV photon with energy of 70 eV. If we use this XUV photon to ionize neon atoms ( $I_p = 21.56$  eV), the initial velocity of ionized electrons is  $4.12 \times 10^6$  m/s. If the length of the TOF is  $L = 43$  cm, then the time of flight for unaccelerated electrons is  $T_0 = 1.04 \times 10^{-7}$  s. Also, let's assume the following form for the electric field of the driving pulse:

$$F(t) = F_0 \exp \left[ -1.38 \left( \frac{t}{\tau_p} \right)^2 \right] \cos(\omega t) \quad 2.15$$

where  $\tau_p = 4$  fs is the pulse duration,  $\omega = 2.41$  PHz is its central angular frequency, and  $F_0 = 0.6$  V/Å (corresponding to  $10^{13}$  W/cm<sup>2</sup> intensity, remember that  $10^{14}$  W/cm<sup>2</sup> is the intensity needed for HHG in Argon).

Let's assume that, the XUV ionization of an electron happens, at the zero-crossing electric field of the strongest half cycle of the electric field of the driving pulse (in other words, the maximum amplitude of vector potential, see figure 2.5). For this delay, the driving pulse changes the velocity of the ionized electrons by  $\Delta v = 4.33 \times 10^5$  m/s. As a result, the time of flight of the accelerated electron will be:  $T_f = 0.94 \times 10^{-7}$  s.

The difference between time of flight of the accelerated and unaccelerated electrons are:

$$\Delta T = T_0 - T_f = 9.9 \times 10^{-9} \text{s.}$$

For a 100 ps per time bin, multiple-event time digitizer like MCS6A, this is 99 channels. Ideally, we should be able to detect changes in the electric field when there is at least 1 channel change (in our case 100 ps), or  $\Delta V = 4.3 \times 10^5$  m/s. This value corresponds to  $\Delta A = 2.44 \times 10^{-5}$ . For an optical wave at 780 nm, this will correspond to an electric-field change of  $\Delta F = 0.06$  V/Å. This is theoretically the weakest field amplitude at  $\lambda = 780$  nm that will be measured in the absence of noise by the aforementioned setup. At,  $\lambda = 390$  nm, the weakest field amplitude increases to  $\Delta F = 0.12$  V/Å, since attosecond streaking measures vector potential. Therefore, to measure weaker fields, a longer TOF is required. But having a longer TOF reduces the number of electrons that reach the MCP which reduces the sensitivity of the measurement.

This theoretical calculation shows that attosecond streaking has low SNR for the detection of optical transients with weak electric field amplitude. The situation becomes worse at higher frequencies because the final velocity of the electrons is the function of the vector potential of the driving field. Any detection that relies on the measurement of the vector potential naturally favors lower frequencies.

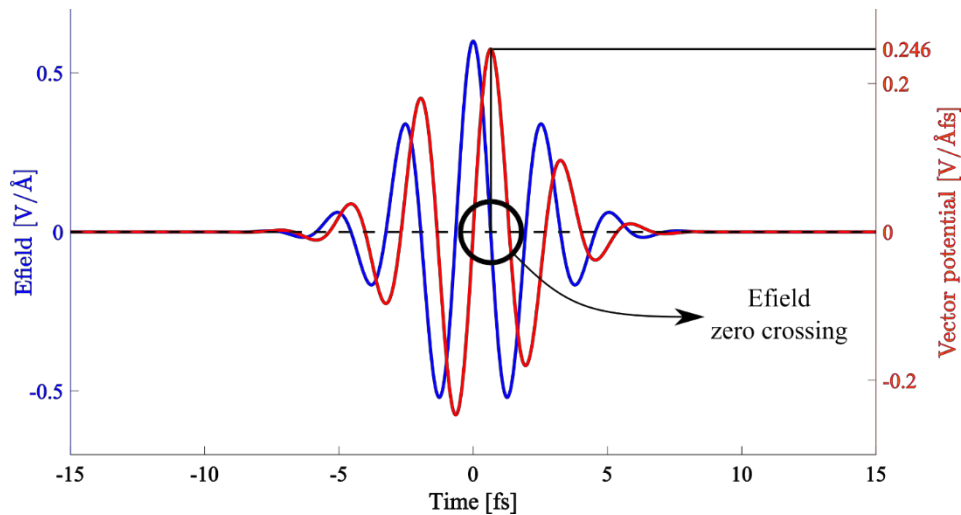


Figure 2.5. The theoretical electric field of the driving pulse (blue curve). Corresponding vector potential field (red curve)

### 2.3. Intra-band current

Time-dependent change in electric dipole creates electric currents [19]. Let's consider a simple dipole i.e.:

$$\vec{\mathbf{p}} = q\vec{\mathbf{d}} \quad 2.16$$

Where the  $\vec{\mathbf{p}}$  is the dipole moment vector,  $q$  is the amount of electric charge that is separated and  $\vec{\mathbf{d}}$  is the displacement vector. If the amount of separated charge is constant, then, the temporal change of this dipole is:

$$\frac{d\vec{\mathbf{p}}}{dt} = q\vec{\mathbf{v}} \quad 2.17$$

where  $\vec{\mathbf{v}}$  is the relative velocity of the charge separation.

In quantum mechanics, it is easier to talk about momentum:

$$\frac{d\vec{\mathbf{p}}}{dt} = \frac{q\vec{\mathbf{p}}}{m} \quad 2.18$$

(Please note that since electric dipole and momentum are usually shown using the letter  $p$ , the author has chosen to use normal font  $\mathbf{p}$  for momentum and script font  $\vec{\mathbf{p}}$  for momentum.), where  $m$  is the effective mass of the charge carriers. Moreover, the measurable quantities in terms of quantum mechanics are expectation values:

$$\left\langle \frac{d\vec{\mathbf{p}}}{dt} \right\rangle = \frac{q\langle \vec{\mathbf{p}} \rangle}{m} \quad 2.19$$

Finally, for a system that has multiple charge carriers, the total dipole change is:

$$\left\langle \frac{d\vec{\mathbf{p}}}{dt} \right\rangle_{\text{total}} = \sum_{\substack{i=\text{all} \\ \text{charge} \\ \text{carriers}}} \frac{q_i \langle \vec{\mathbf{p}}_i \rangle}{m_i} \quad 2.20$$

where the index  $i$  indicates the different charge carriers. Charge carriers in a solid-state system are electrons and holes. These carriers may be distributed in different quantum states, with different population probabilities. So  $\langle \vec{\mathbf{p}}_i \rangle$  is the product of the occupation number of the specific state times the density of that state times the expectation value of the momentum of the single state:

$$\langle \vec{\mathbf{p}}_i \rangle = g_i \times \rho_i \times \langle \vec{\mathbf{p}} \rangle_i \quad 2.21$$

where  $g_i$  is the density of state  $i$  and  $\rho_i$  the occupation number for that state. One can use density functional theory (DFT) to calculate initial density of states [73]. When charge carriers interact with an external electric field, they transition to other states; therefore, the occupation numbers also change with time. This time-dependent change can be furthermore calculated within the framework of the time-dependent DFT (TDDFT) [74]. In our current model, we consider that the density of states remains constant (this assumption is valid under weak-field interaction) [75].

## 2.4. Bloch equation

The next question is how to calculate the expectation value of the momentum for a given state? Most of the systems that we study are periodic. Therefore, we can use the Bloch theorem to describe their wave function [76]. The Bloch theorem states that given a system with a periodic potential:

$$V(\vec{r} + \vec{R}) = V(\vec{r}) \quad 2.22$$

The energy eigenstates this system can be written as:

$$\psi_n(\vec{r}) = e^{i\vec{k}\cdot\vec{r}} \phi_n(\vec{r}) \quad 2.23$$

Here,  $\phi(\vec{r})$  is periodic in  $\vec{r}$  with  $\vec{R}$  periodicity. The  $\vec{k}$  is called the lattice wave vector and should not be confused with the wave vector for the particle momentum. The index n is the indicator of the energy band that the carrier is occupying.

Inserting this wave function in the Schrödinger equation we get

$$H_{\vec{k}} \phi_n(\vec{r}) = \left( \frac{\hbar^2}{2m} \left( \frac{1}{i} \vec{\nabla} + \vec{k} \right)^2 + V(\vec{r}) \right) \phi_n(\vec{r}) \quad 2.24$$

Looking at the Schrödinger equation for these systems we notice quickly that the energy eigenvalue for each band is a function of  $\vec{k}$ . If we move by one lattice wavenumber value (i.e.  $\vec{q}$ ), and we take the Taylor expansion of the energy in k we have:

$$\varepsilon_n(\vec{k} + \vec{q}) = \varepsilon_n(\vec{k}) + \vec{\nabla} \varepsilon_n(\vec{k}) \cdot \vec{q} + \frac{1}{2} \sum_{i,j} \frac{\partial^2 \varepsilon_n(\vec{k})}{\partial k_i \partial k_j} q_i q_j + \mathcal{O}(q^3) \quad 2.25$$

This equation looks similar to the small-perturbation correction to eigenenergies. In this case,  $\varepsilon_n(\vec{k} + \vec{q})$  is eigenvalue for  $H_{\vec{k}+\vec{q}}$ , which according to periodic nature of the Hamiltonian looks like:

$$H_{\vec{k}+\vec{q}} = H_{\vec{k}} + \frac{\hbar^2}{m} \left( \frac{1}{i} \vec{\nabla} + \vec{k} \right) \cdot \vec{q} + \frac{q^2}{2m} \quad 2.26$$

Since q is small, we can neglect the quadratic term in Eq. 2.10 and 2.11 and consider  $\frac{\hbar^2}{m} \left( \frac{1}{i} \vec{\nabla} + \vec{k} \right)$  as a perturbation source. Next, we calculate the perturbative energy shift and equate terms with the same q order in Eq. 2.25 and 2.26. As a result, the perturbative energy relation is:

$$\vec{\nabla} \varepsilon_n(\vec{k}) = \frac{\hbar^2}{m} \int \phi_n^*(\vec{r}) \left( \frac{1}{\hbar} \vec{\nabla} + \vec{k} \right) \phi_n(\vec{r}) d^3 \vec{r} \quad 2.27$$

Using the Bloch wave function relation, we get:

$$\vec{\nabla} \varepsilon_n(\vec{k}) = \int \psi_n^*(\vec{r}) (i\hbar \vec{\nabla}) \psi_n(\vec{r}) d^3 \vec{r} \quad 2.28$$

This is the definition of expectation value for the momentum:

$$\langle \vec{p} \rangle = \vec{\nabla} \varepsilon_n(\vec{k}) = \int \psi_n^*(\vec{r}) (i\hbar \vec{\nabla}) \psi_n(\vec{r}) d^3 \vec{r} \quad 2.29$$

One of the requirements for the validity of the above analysis is that the wavelength of the applied field should be orders of magnitude larger than the spatial extent of the wavefunction. In the language of the reciprocal lattice, this means that the wavefunction should occupy multiple  $k$  points.

Now we need to know how this expectation value evolves in a system that interacts with external fields. Since the band energy, is a function of  $\vec{k}$ , the change in the expected value of momentum has to come from the change in  $k$  point in the crystal which the carrier is occupying. By applying some semi-classical approximation<sup>12</sup> Bloch predicted that the carrier under influence of external field would travel through  $k$  points in the lattice in a ballistic manner, thus:

$$\vec{k}_f = \vec{k}_i + \frac{1}{c}\vec{A}(t) \quad 2.30$$

Putting this time-dependent value of  $k$  into Eq. 2.29 we get:

$$\langle \vec{p} \rangle = \vec{\nabla} \mathcal{E}_n \left( \vec{k}_i + \frac{1}{c}\vec{A}(t) \right) \quad 2.30$$

Now, we can easily describe the current due to time-dependent dipole moment changes.

In a system with multiple bands, with different band energy dispersion relations, the time-dependent inter-band current is:

$$\mathbf{J}(t) = \sum_{\mathbf{k}} \sum_n q_n \times \rho_n(\vec{k}(t)) \times (\vec{\nabla} \mathcal{E}_n(\vec{k}(t))) \quad 2.31$$

Let's consider a wave packet with a crystal momentum spread of  $\Delta k$  centered at the crystal's  $\Gamma$  point ( $k = 0$ ). Let's also assume that this crystal has a parabolic dispersion relation:

$$\mathcal{E}(k) = \alpha k^2 \quad 2.32$$

where we define the effective mass of the carrier as:

$$M_{\text{eff}} = \frac{2\alpha}{\hbar^2} \quad 2.33$$

Then the energy extent is  $\Delta E = \alpha \Delta k^2$ . This means that time-domain extent of the wave packet should be  $\Delta T = \frac{\hbar}{\Delta E} = \frac{\hbar}{\alpha \Delta k^2}$  (figure 2.6).

---

<sup>12</sup> It means that the electromagnetic field is treated classically, and it is assumed to be homogeneous. This assumption also neglects the existence of any scattering [73].

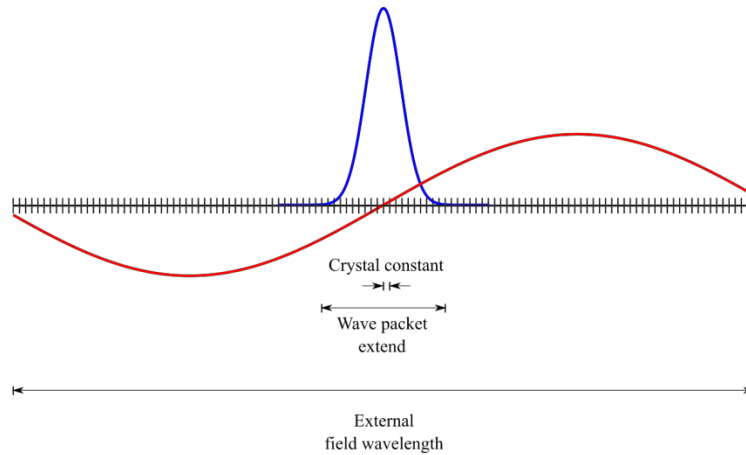


Figure 2.6. The validity of the semi-classical model. The blue curve demonstrates the envelope of wave packet of charge carrier in space. The red curve is the spatial extent of the wavelength of the external field. The semi-classical model is valid when this wavelength is much greater than the spatial spread of the charge carrier wave function.

From the previous discussions, we conclude that for a better understanding of the ultrafast carrier currents in large bandgap mediums, we need to find another injection process. An injection process that completely decouples the inject and drive steps, gives us a well-defined initial carrier wave packet in CB and does not damage the medium. This process also has to happen on a short time scale. Linear injection using XUV pulses from HHG can provide us with the means to achieve all these goals.

## 2.5. Landau-Zener transition

The acceleration theorem provides a fair description of what happens when the electron wave-packet propagates adiabatically within its energy band. But it does not describe the transition of electrons between bands<sup>13</sup>.

Landau and Zener proved formalism for the diabatic<sup>14</sup> transition between two-level systems where the energy levels are a function of a time-dependent parameter [77, 78, 79, 80]. In the case of solids, during the interaction with an electromagnetic wave, this parameter is the time-dependent lattice momentum,  $k(t) = k_0 + 1/c \times A(t)$ .

The energy eigenvalue of each band has a dispersion relation to  $k$ . One approach is to plot the energy with respect to  $k$ ; but, in case of an external influence that can change the value of  $k$ , we can directly describe the energies of the two bands as functions of time. As a matter of fact, in this formalism, the change of the parameter is always due to the perturbation from an external influence. In our case, this is a time-dependent electric field.

Landau and Zener have shown that, if there exist a critical value of the parameter  $k$ , where the energy difference of the two states is very small, then a non-adiabatic transition can occur, after which the system can evolve adiabatically.

To illustrate the problem, let's first consider a simple two-level system where the Hamiltonian is:

<sup>13</sup> It should be noted that, any superposition of Bloch states that possess the same crystal momentum obeys the acceleration theorem, even if the accelerating field causes transitions among the bands

<sup>14</sup> Diabatic means non-adiabatic which means there is a transfer of energy or particle in contrast to the adiabatic case where there is no transfer of energy or particle.

$$H = \begin{pmatrix} \frac{\alpha t}{2} & H_{12} \\ H_{12}^* & -\frac{\alpha t}{2} \end{pmatrix} \quad 2.34$$

where  $H_{12}$  and its complex conjugate are very small<sup>15</sup>.

If the coupling term is zero the time-dependent energy eigenvalues for the two states  $\psi_1 = \begin{pmatrix} 1 \\ 0 \end{pmatrix}$  and  $\psi_2 = \begin{pmatrix} 0 \\ 1 \end{pmatrix}$  would be,  $E_1 = \frac{\alpha t}{2}$  and  $E_2 = -\frac{\alpha t}{2}$  (figure 2.7.a).

Now if we include the coupling term, at  $t = 0$ , we shall have the energy eigenvalues  $E(0) = \pm|H_{12}|$ . For  $t \rightarrow \pm\infty$ ,  $\lim_{t \rightarrow \pm\infty} E(t) = \pm\alpha t/2$ . So, the energy of these states  $\psi_1 = \begin{pmatrix} 1 \\ 0 \end{pmatrix}$  and  $\psi_2 = \begin{pmatrix} 0 \\ 1 \end{pmatrix}$  will evolve like figure 2.7.b since state 1 and 2 will change to one another at  $t = 0$ , we define two energy function  $E_+$  and  $E_-$  as follow:

$$E_{\pm} = \pm\sqrt{|H_{12}|^2 + \alpha^2 t^2/4} \quad 2.35$$

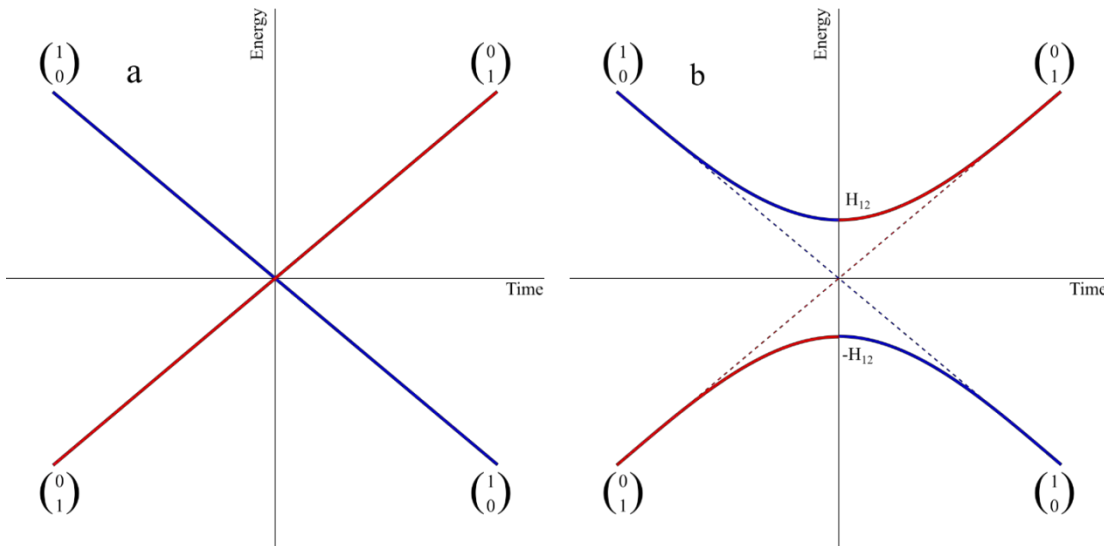


Figure 2.7. Time evolution of energy eigenvalue of a two-level system, with state  $\begin{pmatrix} 1 \\ 0 \end{pmatrix}$  depicted by blue curves and state  $\begin{pmatrix} 0 \\ 1 \end{pmatrix}$  depicted by red curves. a) Crossing states, the coupling between two state is zero if the initial time electron is in one state (e.g. state  $\begin{pmatrix} 1 \\ 0 \end{pmatrix}$ ) it will continue to remain in the same state at the point of crossing blue. b) Anti crossing scenario, where due to the coupling of the two states,  $\begin{pmatrix} 1 \\ 0 \end{pmatrix}$  will continue its evolution in state  $\begin{pmatrix} 0 \\ 1 \end{pmatrix}$ . The dashed line represents the uncoupled scenario.

These energy curves are also known as diabatic energy eigenstates.

<sup>15</sup> For better understanding of this example please refer to the following paper [81] by J. R. Rubbmark et al.

Let's consider that at  $t = -\infty$  we are at state  $\psi_2 = \begin{pmatrix} 0 \\ 1 \end{pmatrix}$ , i.e. the energy is  $E_-(t)$ . The adiabatic theorem suggests that the system at  $t = 0$  will follow the same curve and continue to evolve with the same energy curve as in the state  $\psi_1 = \begin{pmatrix} 1 \\ 0 \end{pmatrix}$ <sup>16</sup>.

If we want to stay in state  $\psi_2 = \begin{pmatrix} 0 \\ 1 \end{pmatrix}$  after  $t > 0$  we cannot rely on an adiabatic evolution anymore. Therefore, the diabatic transition has to happen. To understand the reason behind this transition, let's take a look at the Hamiltonian of the system at  $t = 0$ :

$$H = \begin{pmatrix} 0 & H_{12} \\ H_{12}^* & 0 \end{pmatrix} \quad 2.36$$

This Hamiltonian looks like the Hamiltonian of the Rabi system, with Rabi oscillation frequency of [82]:

$$\nu_{\text{Rabi}} = \frac{|H_{12}|}{h} \quad 2.37$$

Therefore, due to this coupling term the system at time zero make a transition to level two adiabatically. The period of this Rabi oscillation plays an important role in the definition of the diabatic transition time.

The half period, when the tangent line of the energy curves at  $t = 0$  (the black horizontal line in figure 2.8) is taken and continued in both negative and positive direction until it crosses the energy curve for the non-coupled system (blue and red dashed lines in figure 2.8), is defined as the diabatic time:

$$\tau_d = 2 \times \frac{|H_{12}|}{\alpha} \quad 2.24$$

$2 \times \tau_d$  is the time it takes for the energy of the non-coupled system to change from the  $-\frac{\alpha t}{2}$  to  $\frac{\alpha t}{2}$ . If the period of one Rabi oscillation is smaller than the diabatic time, it is possible to start from the  $E_-(t)$  curve and continue to the upper curve, i.e.  $E_+(t)$ . The criterion for such transition is:

---

<sup>16</sup> Remember that adiabatic transition just means that the energy is conserved. Therefore, continuing from state  $\begin{pmatrix} 1 \\ 0 \end{pmatrix}$  for  $t < 0$  to the same state for  $t > 0$  is prohibited.

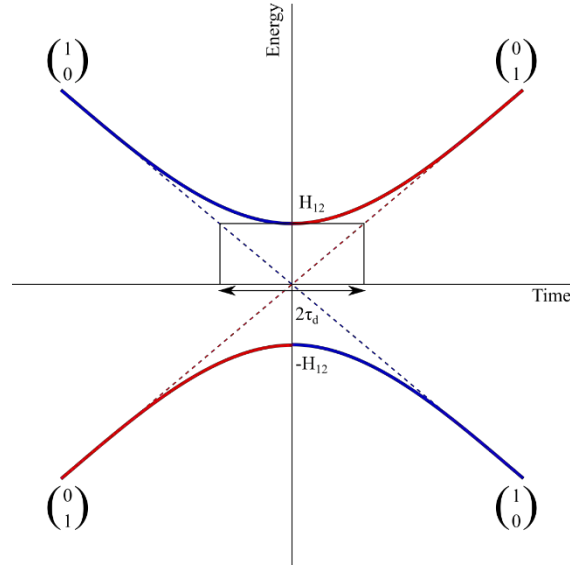


Figure 2.8. Semi-classical demonstration of the time required to for state  $\psi_1 = \begin{pmatrix} 1 \\ 0 \end{pmatrix}$  turn into the state  $\psi_2 = \begin{pmatrix} 0 \\ 1 \end{pmatrix}$ . If the time is greater than the Rabi oscillation period of these states, then Landau-Zener transition happens.

$$\frac{|H_{12}|^2}{\alpha \hbar} \gg 1 \quad 2.38$$

Landau and Zener proved that the probability of such transition is equal to:

$$P_D = \exp(-4\pi^2 \nu_{\text{Rabi}} \tau_d) \quad 2.39$$

If the  $|H_{12}|$  is sufficiently small the probability of transition increases.

This approximation is only valid when:

1. The perturbation parameter in the Hamiltonian is a known, linear function of time.
2. The energy separation of the diabatic states varies linearly with time.
3. The coupling in the diabatic Hamiltonian matrix is independent of time.

An important parameter in this approach is the Landau-Zener velocity:

$$v_{LZ} = \frac{\frac{\partial}{\partial t} |E_+ - E_-|}{\frac{\partial}{\partial q} |E_+ - E_-|} \approx \frac{dq}{dt} \quad 2.40$$

where  $q$  is the strength of the perturbation. A larger  $v_{LZ}$  means a larger diabatic transition probability [83]. You can use this parameter to rewrite the probability of the transition as:

$$P_D = \exp(-2\pi\gamma) \quad 2.41$$

Here  $\gamma$  is:

$$\gamma = \frac{|H_{12}|^2 / \hbar}{\left| \frac{dq}{dt} \frac{\partial}{\partial q} (E_+ - E_-) \right|} \quad 2.42$$

In a periodic system, if we don't have the coupling<sup>17</sup> the energy eigenvalues are completely parabolic:

$$E(k) \propto k^2 \quad 2.43$$

According to the Bloch theorem, any periodic system has to have same energy after every Brillouin zone, i.e.:

$$E(k + \pi/\alpha) = E(k) \quad 2.44$$

where  $\alpha$  is size of the lattice.

If we plot these energy eigenvalues (figure. 2.9) in one Brillouin zone we will see a collection of points that look like crossing points same as the figure 2.7.a.

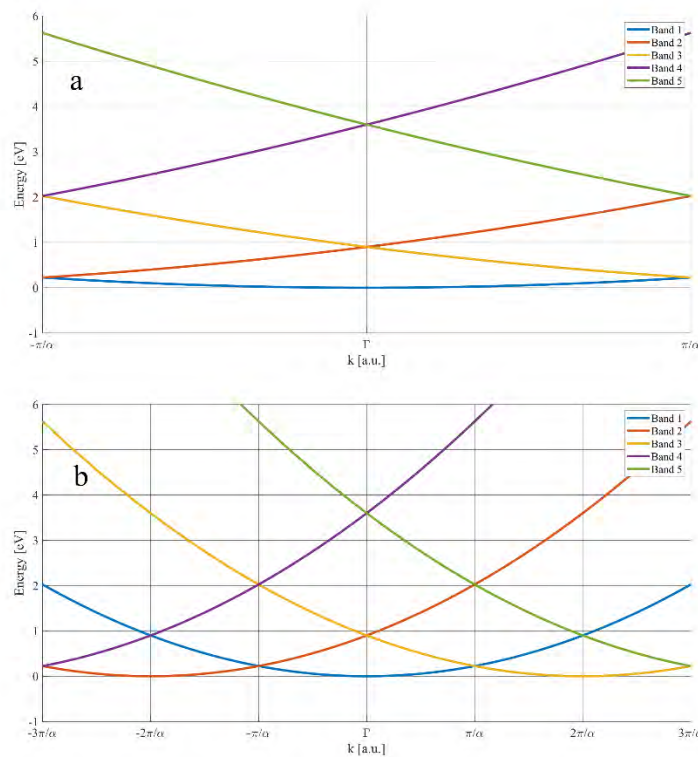


Figure 2.9. The energy dispersion free electrons in a periodic system without any coupling near Bragg planes. a) the reduced Brillouin zone scheme. b) The extended Brillouin zone scheme

The coupling term is the effect of neighboring sites that will break the degeneracy at half of the Bragg points in the reciprocal lattice (Fig. 2.10 a).

<sup>17</sup> Coupling is usually due to the effect of the coulomb potential of the neighboring sites on the crystal.

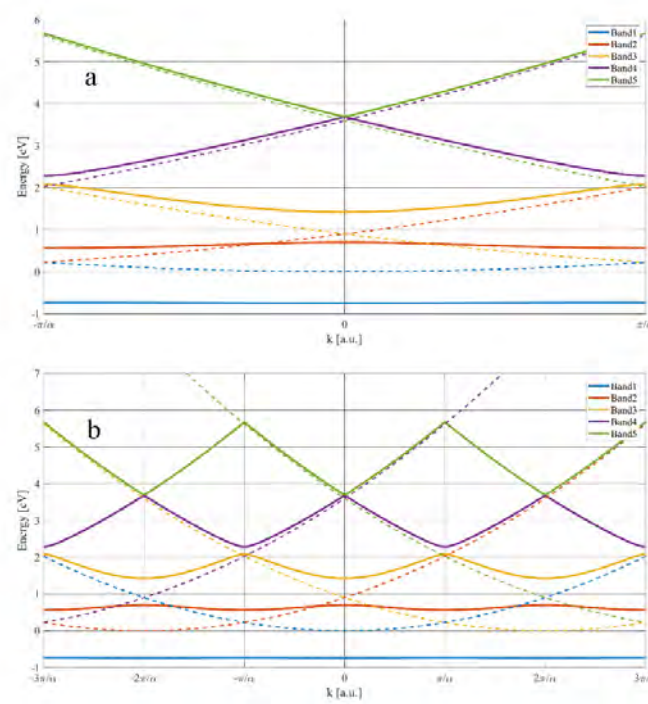


Figure 2.10. The energy dispersion free electrons in a periodic system with the addition of coupling near Bragg planes. a) the reduced Brillouin zone scheme. b) The extended Brillouin zone scheme.

Therefore, in a periodic system those states that have energy relations like Eq. 2.43 are equivalent to  $\psi_1 = \begin{pmatrix} 1 \\ 0 \end{pmatrix}$  and  $\psi_2 = \begin{pmatrix} 0 \\ 1 \end{pmatrix}$  with energy eigenvalues  $E_1 = \frac{\alpha t}{2}$  and  $E_2 = -\frac{\alpha t}{2}$  and states that are separated due to coupling (solid lines in Fig 2.10 b) are like new states in Eq. 2.35. If we use the Bloch acceleration theorem, we can easily see that the evolution of the states is governed by the change of the vector potential.

In a system where the diabatic states are the energy bands of the crystals, the interpretation of the parameter  $\frac{dq}{dt} \frac{\partial}{\partial q} (E_+ - E_-)$  becomes very interesting. This parameter indicates how fast the energy changes with respect to time. In Bloch formalism, the change in energy of the band comes through the temporal change of the crystal momentum to vector potential of the external field (Eq. 2.30). Let's consider a simple dispersion relation band 1 and 2:

$$E_1 = F(k) - E_g/2 \quad 2.45$$

$$E_2 = G(k) + E_g/2 \quad 2.46$$

Where  $F(k)$  and  $G(k)$  are the dispersion relations of the 1<sup>st</sup> and 2<sup>nd</sup> band and  $E_g$  is bandgap of the two bands at edge of Brillouin zone:

$$2|H_{12}| = E_g \quad 2.47$$

According to Bloch theorem the temporal evolution of the energy with is:

$$E_1 = F\left(k + \frac{1}{c}A(t)\right) - \frac{E_g}{2}$$

$$E_2 = G\left(k + \frac{1}{c}A(t)\right) + \frac{E_g}{2}$$

If we take  $q = A(t)$ , then:

$$\frac{dq}{dt} = \frac{dA}{dt} = -F_{\text{ext}}(t) \quad 2.48$$

Also:

$$\begin{aligned} \frac{\partial}{\partial q}(E_1 - E_2) &= \frac{\partial}{\partial A}(E_1 - E_2) \\ &= -\frac{1}{c}A(t) \left[ \frac{\partial F}{\partial A} - \frac{\partial G}{\partial A} \right] \end{aligned} \quad 2.49$$

Therefore:

$$\gamma = \frac{|E_g/2|^2/\hbar}{\left| -\frac{1}{c}F_{\text{ext}}(t)A(t) \left[ \frac{\partial F}{\partial A} - \frac{\partial G}{\partial A} \right] \right|} \quad 2.50$$

As it is evident the probability of the Landau-Zener transition is non-zero somewhere between the extrema of the electric field and the extrema of the vector potential. At extrema of any of them, this transition has zero probability.

Another observation from this result is that the probability of the Landau-Zener transition increases by increasing the field amplitude of the external field. Also, if the effective mass of the electron is higher the chancer of this transition also becomes higher.



# 3. Experimental Setup and measurement procedure.

In this chapter, a detailed description of the experimental system that has been used for this thesis is provided. This includes a brief introduction of the laser source and more detailed information about the attosecond beamline, the AS2000. In the end, data acquisition method and experimental procedures are described.

## 3.1. Laser source

To provide the NIR source for our experiment, we use a Kerr lens mode-locked (for further information about Kerr lens mode-locking please refer to [84, 85, 86, 87]) Ti:Sa oscillator (Rainbow 2, Femtolasers GmbH) with pulse duration of 8 fs, pulse energy of 9 nJ, carrier wavelength of  $\lambda = 780$  nm and repetition rate of  $\nu_{\text{rep}} = 78$  MHz.

Right after the oscillator, there is a commercial CEP stabilization module (CEP4, Femtolasers GmbH) [88]. This module contains a periodically poled lithium niobate (PPLN) crystal. This crystal has been made for a quasi-phased matched generation of DFG of the NIR pulse. The DFG pulse and the low-frequency part of the NIR pulse will interfere. It has been shown [89] that the beat frequency of this interference can be calculated by frequency comb considerations and is equal to:

$$f_{\text{beat}} = f_{\text{CEO}} \tag{3.1}$$

where  $f_{\text{CEO}}$  is the carrier-envelope offset-frequency. This beat signal is sent to the spectrum analyzer module of CEP4 and locked onto the 7.5 MHz. Long-term CEP jumps are compensated by a pair of wedges inside the laser cavity.

For compensation of short-term CEP jumps, the beat signal is amplified to a signal level of 40 dBm and sent to an acousto-optic frequency shifter (AOFS). This device creates an acoustic wave that can change the refractive index of the crystal which will affect the CEP of the pulse and as a result, the diffracted beam will be CEP stable (for more details about this method of CEP stabilization please refer to reference [90]).

After CEP stabilization the resulting pulse is very weak  $E_{\text{pulse}} \approx 4$  nJ. This weak pulse is amplified using the method of chirped pulse amplification (CPA) [91]. The CPA amplifier is a 9-pass commercial system (Femtopower Compact PRO HP/HR, Femtolasers GmbH). First, the pulse is stretched using a pair of wedges. Then a strongly pumped Ti:Sa crystal is seeded by this weak laser pulse. The pump laser is a Q-switched frequency-doubled Neodymium-doped yttrium lithium fluoride (Nd:YLF) laser (DM30-527, Photonics Industries International Inc.), with an average pulse power of 25 W and pulse duration of 9 ns and repetition rate of 3KHz.

At first, the NIR pulse gets amplified during four round-trips. A Ti:Sa crystal with a thickness of 3 mm cannot handle the amplification of 78 MHz pulses any more than this. Therefore, after the 4<sup>th</sup> pass, the pulse is sent to a Pockels cell as pulse picker to reduce the rep-rate of the laser. The output becomes 3KHz (a better overview of our CPA system is given in reference [92]).

The effect of gain narrowing in Ti:Sa crystal reduces the bandwidth of the amplified pulse [93]. To negate this shortcoming, the pulse after the Pockels cell is sent to an acousto-optic programmable dispersive filter (AOPDF), which is commercially called DAZZLER (HR 800, Fastlite). The DAZZLER creates an acoustic wave which through wave mixing can modulate the transmission of the pulse [94, 95]. The wave mixing in DAZZLER can also correct the spectral phase up to the 4<sup>th</sup> order which helps later when we need to compress the output of CPA.

After the DAZZLER, the pulse passes through the Ti:Sa crystal 5 more times. The output pulse energy is  $E_{pulse} \approx 1.2$  mJ. Since the pulse has been stretched before the CPA, it needs to be re-compressed after the amplification. Normally, materials don't have negative dispersion. To create this condition, a pair of transmission gratings are used. This pair can compensate for the 2<sup>nd</sup> order dispersion [96]. After this pair the pulse should have the duration of  $\tau_{pulse} \approx 25$  fs and pulse energy of  $E_{pulse} = 0.8$  mJ.

Further compression of these pulses requires the generation of more bandwidth. We can extend the bandwidth of these pulses by self-phase-modulation (SPM) [97, 98]. After the CPA, the laser beam is focused on a 2 m hollow-core fiber (HCF) filled with Ne gas at a pressure of 1.8 bars. The broadened output of the HCF covers the bandwidth over the range of 450 nm to 1100 nm. The output pulse energy after the fiber is about  $E_{pulse} = 0.5$  mJ.

From the exit window of the fiber tube, the reflected beam is picked up and is focused onto a beta barium borate (BBO) crystal which is set to generate phase-matched SHG of 780 nm. The interference of the SHG signal and the blue part of the fundamental is used for the stabilization of CEP [89]. The CEP jumps are due to the amplification step in CPA. The compensation of the CEP is done by changing the amount of glass in the stretching pair of wedges before CPA.

Now, we have the bandwidth for the creation of pulses as short as 3 half-cycles (more than an octave of bandwidth), we need to compress this pulse with such large bandwidth. This is done using 4 pairs of multilayered broadband double angle chirped mirrors (the angles of incidence on these mirrors are 5 and 19 degrees). Chirp mirrors can only compensate 1 octave of the bandwidth [99, 100, 101]<sup>18</sup>. Therefore, they have high reflectivity only in the wavelength range from 1000 nm to 500 nm. Each pair can compensate for 1 mm of SiO<sub>2</sub> glass (group delay dispersion of  $GDD = 40$  fs<sup>2</sup> at 780 nm) or roughly 2 m of air. The first pair compensates for the exit window of the fiber tube and the second pair compensates for the extra air distance that we have. A third pair compensates for the window of the vacuum system flange. We need the fourth pair because later on, we use a 1 mm beam splitter in the vacuum system. For finer control of the dispersion, chirp mirrors are designed to overcompensate the dispersion. As a result, we shall have negative dispersion, which we shall compensate using a pair of SiO<sub>2</sub> wedges. After full compression, we end up having a short pulse with a duration of  $\tau_{pulse} = 5$  fs and pulse energy of  $E_{pulse} = 250$   $\mu$ J.

The energy and duration of this pulse are now suitable for high-harmonic generation. Since XUV photons are absorbed in air, we send the beam into a vacuum system. In the next section, we will describe the vacuum chambers in detail.

---

<sup>18</sup> It should be noted that 1.5 octave chirp mirrors have been reported [102]. But the reflectivity of such mirrors has a deep around 800 nm where the carrier wavelength of our laser is.

## 3.2. AS2000

Our attosecond metrology setup is an interferometer in which the measurement is performed in a pump-probe manner. One arm of the interferometer contains the pump and the other arm contains the probe. There is always a piezo translation stage that will be used to delay probe versus pump pulse. This beamline is comprised of three chambers: a HHG chamber in which XUV photons are generated and has the beam splitter of the interferometer; a delay chamber where the delay between the pump and the probe pulses is created. Also, it contains the beam combiner; an experimental chamber, where the measurement is performed. We shall describe each of these chambers in detail in the next three subsections.

### 3.2.1. HHG chamber

The NIR pulse produced by our laser first enters the HHG chamber and passes through a motorized iris. This iris is used to achieve phase matching for the different XUV photon energies<sup>19</sup>. After the iris, a beam splitter is placed. The splitting ratio is 90% to 10%. The HHG arm receives 90% ( $\cong 225 \mu\text{J}$ ) and the beam is focused by a 600 mm focal length spherical mirror onto an argon-filled ceramic target (300  $\mu\text{m}$  hole size, 3 mm tube length). The argon backing pressure is chosen between 40 and 70 mbars (depending on the phase matching). The intensity of the pulse for HHG is estimated to be  $I \cong 7.1 \times 10^{14} \text{W}/\text{cm}^2$  which correspond to field amplitude of  $F = 5.1 \text{V}/\text{\AA}$ . This pulse is intense enough to generate cutoff harmonics up to approximately  $E_{\text{xuv}} \cong 80 \text{eV}$  (refer to equations 2.2a and 2.2b). We use a pair of fused silica wedges to control the dispersion for the NIR pulse before the HHG target. We shall call this arm of the interferometer the inject arm.

The remaining 10% of the NIR pulse energy (25  $\mu\text{J}$ ) passes through a separate pair of fused silica wedges. This pulse is directed toward the delay stage in the Delay chamber. We call this arm the Delay arm.

Since we inject argon gas with a backing pressure above 40 mbars into harmonics target, we don't need an ultra-high vacuum condition in HHG chamber. So, one turbo pump can easily maintain the pressure of the chamber at  $P_{\text{HHG}} = 5 \times 10^{-4}$  mbars when there is no gas. When the target is fed with gas, the pressure of the chamber rises to  $P_{\text{HHG}} \sim 1 \times 10^{-3}$  mbar. (For a better understanding of the HHG chamber design, please take a look at figure 3.1)

Since the delay and the injecting beams separated before HHG target, we can put two independent pairs of wedges to control the CEP of injecting and delay pulses independently. The beams from the injecting and the delay arm are later sent to the delay chamber.

---

<sup>19</sup> Please take a look at Kevin Scharl master thesis for more detailed information about the HHG phase matching [104].

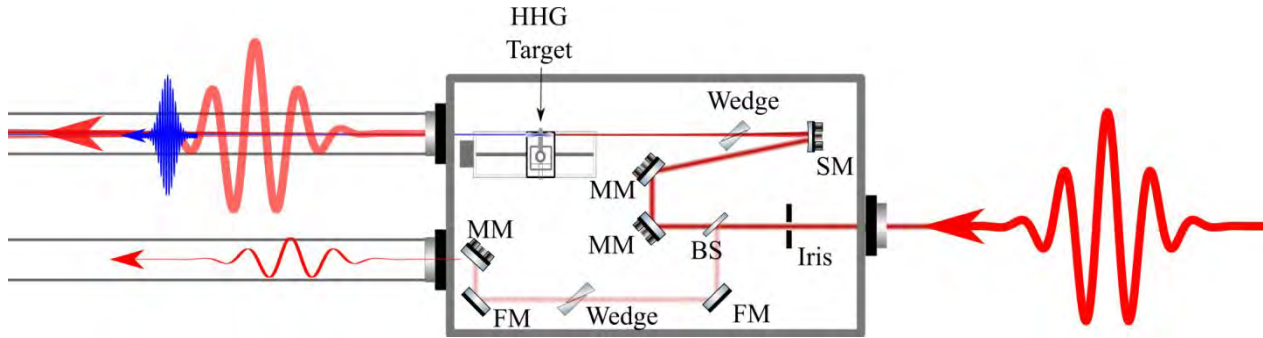


Figure 3.1. Schematic of the HHG chamber in AS2000. MMs are motorized flat silver mirrors. FMs are normal flat silver mirrors. SM is the spherical mirror to focus on the HHG target (focal distance of 600 mm). BS is the beam splitter

### 3.2.2. Delay chamber

As the name of the chamber indicates, it is used to create a controllable delay between the inject and delay arms. Apart from the delay stage, this chamber contains XUV optics. Therefore, it needs a higher level of vacuum than the HHG chamber, otherwise, XUV optics could become oxidized and the intensity of XUV photons would get reduced. The usual performance pressure of this chamber is about  $P_{delay} = 1 \times 10^{-6}$  mbars.

In the inject arm, the generated XUV pulse train passes through a filter. Depending on the measurement, different spectral filters (mounted on a filter wheel) are used. We have a 500 nm thick Al filter for alignment purposes, a 150 nm Aluminum-Scandium (AlSc) filter for isolation of single XUV bursts, and one empty holder for photo-conductive measurements. Right after the filter wheel, there is an off-axis toroidal mirror. This mirror is gold-coated on a monocrystalline silicon toroidal substrate (Pilz-Optics). It is designed to image the harmonic target at point measurement in the experimental chamber. The distance from the HHG target to the toroidal mirror is about 2.5 m. The image point is 80 cm away from the toroidal mirror in the experimental chamber.

In the delay arm, the beam first passes through an iris, that allows the pulses energy to be adjusted between 0.034  $\mu$ J to 23.4  $\mu$ J. Depending on the type of measurement, either a reflective half wave plate (a periscope), a broadband quarter-wave plate<sup>20</sup>[104], or simply nothing can be inserted. Afterward, the beam goes onto the delay stage. This is a silver mirror mounted on a piezo stage. The stage has a translation range of  $\Delta z = 80 \mu\text{m}$  with closed -loop operation. Since the light bounces off a flat silver mirror mounted close to the normal incident, it creates a maximum delay range of  $2 \times \frac{\Delta z}{c} = 533$  fs. The stage can reliably generate delay increments down to  $\Delta\tau = 100$  as. After the reflection from the delay mirror, the beam reflects from a retro-reflector, which consists of two flat mirrors at 45 degrees that are 4 inches away from each other. These two mirrors can be replaced by two off-axis 90 degree parabolic mirrors. In this case, the focus between these two parabolas is served as an intermediate focus, in which extra mediums can be placed. In this thesis, we used this intermediate focus to generate the second harmonic of the NIR pulse (refer to section 5.6).

T In order to focus the light on to the measurement plane of focus in the experimental chamber, we use a 1600 mm radius of curvature (ROC) spherical mirror. For normal experiments (no extra broadening) we use mirrors with a protected silver coating. In cases where we create higher frequencies in between parabolas, based on the intended spectral domain we intend to measure, mirrors with suitable spectral reflectivity would replace the usual protected silver mirrors.

<sup>20</sup> For more detailed information about the design of the broadband fully reflective quarter-wave plate please take a look at the master thesis of Lukas Lehnert [105]

Finally, a perforated flat mirror recombines the injecting and the delay arm. The injection pulse passes through the hole while the driving pulse bounces off the reflecting area around that hole and both beams are sent to the experimental chamber. (An illustration of the Delay chamber is drawn in figure 3.2)

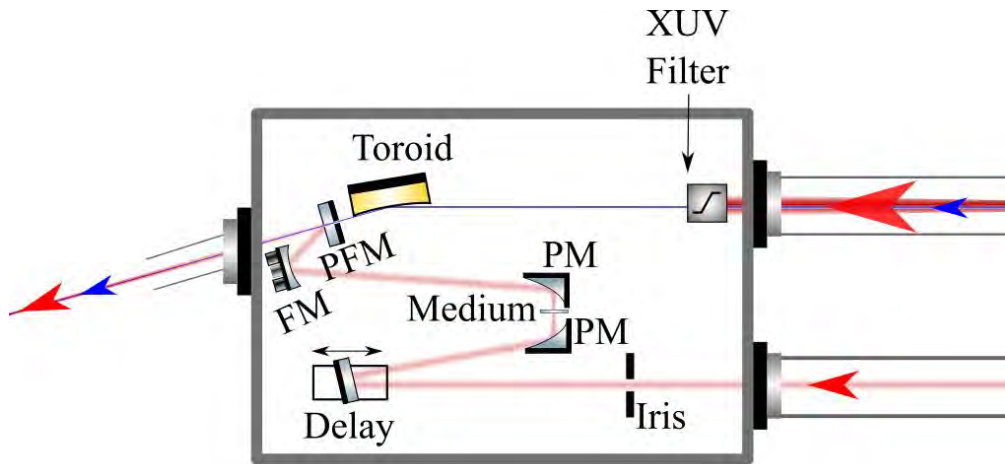


Figure 3.2. Delay chamber of the AS2000. PM mirrors can be flat or 90-degree parabolas. For the purpose of alignment, the upper PM is motorized. The FM is the spherical mirror that that focuses the delay arm. This mirror is also motorized. PFM is the perforated mirror. This mirror is also motorized.

### 3.2.3. Experimental chamber

The experimental chamber should support a vacuum level suitable for attosecond streaking. Therefore, the vacuum level of this chamber should be on the order of magnitude of  $10^{-8}$  mbars. To this end, we need a differential pumping stage from the delay chamber to the experimental chamber.

For the temporal and spatial alignment, in the box used for differential pumping between the delay and the experimental chambers, there is a flip mirror that sends the light to a charged coupled device (CCD) camera. The distance from this camera to the flip mirror is equal to the distance from the focus of the experiment to the flip mirror.

The TOF is placed just above the position of the experimental plane of focus. The gas nozzle and the photoconductive printed circuit board (PCB) are a few mm below the TOF on a two-dimensional translation stage that moves in and out of focus and across the beam.

After the focus, there is a translation stage that moves across the beam. There are three important positions on this translation stage. 1) The transmission mode position: in this position, the light is sent out of the chamber onto a power meter or a grating spectrometer. 2) The profile mode position: at this position there is an unprotected gold mirror. The angle of incidence on this mirror is 80 degrees. The purpose of this mirror is to send the XUV light to an XUV camera. This is meant for better alignment of the NIR pulse onto the HHG target. 3) The monochromator mode position: at this position a toroidal grating is mounted (Horiba). This toroidal grating is blazed for XUV photons of 80 eV. It images the focus of the experimental chamber onto the detector of the XUV camera (GE 2048 BI UV1, Greateyes GMBH). (Please take a look at figure 3.3 for illustration of the experimental chamber).

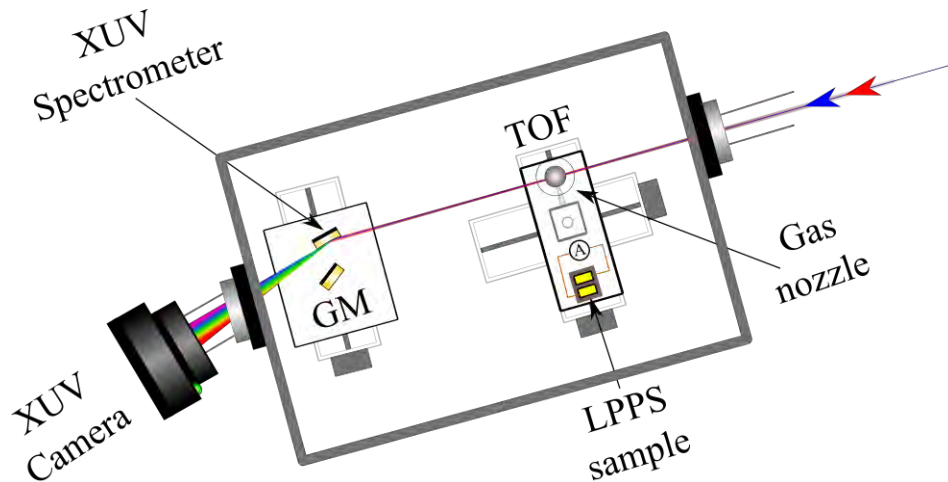


Figure 3.3. Schematic of the experimental chamber in AS2000.

### 3.3. Data acquisition

This section describes the data acquisition tools required for the measurement of the attosecond streaking and the photo-conductive sampling. This includes some technical details about the data acquisition cards, some information about the measurement requirement such as required pressures, voltages, etc. Each measurement technique is described in its subsection.

#### 3.3.1. Photo-conductive sampling

As we have discussed in previous sections, ultra-fast light-driven currents are best detected in large bandgap materials. In this thesis, we are using LiF and SiO<sub>2</sub> (bandgaps 13.6 [106] and 9 [107] eV respectively). For the detection of the current, we have glued 2 stripes of conductive silver epoxy (EPO-TEK H22 Silver Epoxy Glue, Epoxy Technologies Inc.), as our electrodes; on a thin wafer of both LiF (figure 3.4) and SiO<sub>2</sub>. A thin wire connects each electrode to a central pin of a BNC female port. Coaxial cables connected to these BNC ports transfer the current from the PCB to the amplifier. The experimental chamber can act as a giant antenna. It can induce unwanted noise onto the coaxial cables. To reduce this noise a feedthrough-CF flange with float grounding (figure 3.5) is used. The coaxial cables are also antiphonal; therefore, they reduce any mechanical vibration-induced noises.

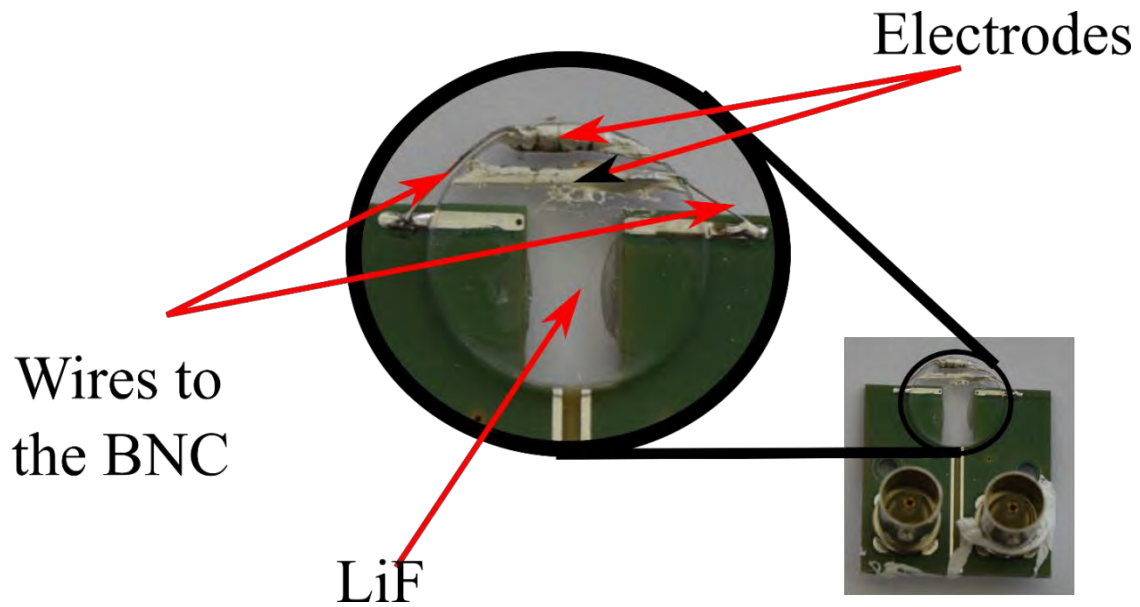


Figure 3.4. The sampling medium is a 1 mm-thick off-the-shelf lithium fluoride VUV window polished for high transmission at 120 nm (Korth Kristalle GmbH) without specified crystal direction. The sample is glued to a PCB. The electrodes are stripes of silver-enriched conductive epoxy glue. Two thin copper wires connect these electrodes to the PCB pins and from there the signal is picked up by the male connector of the BNC terminals.

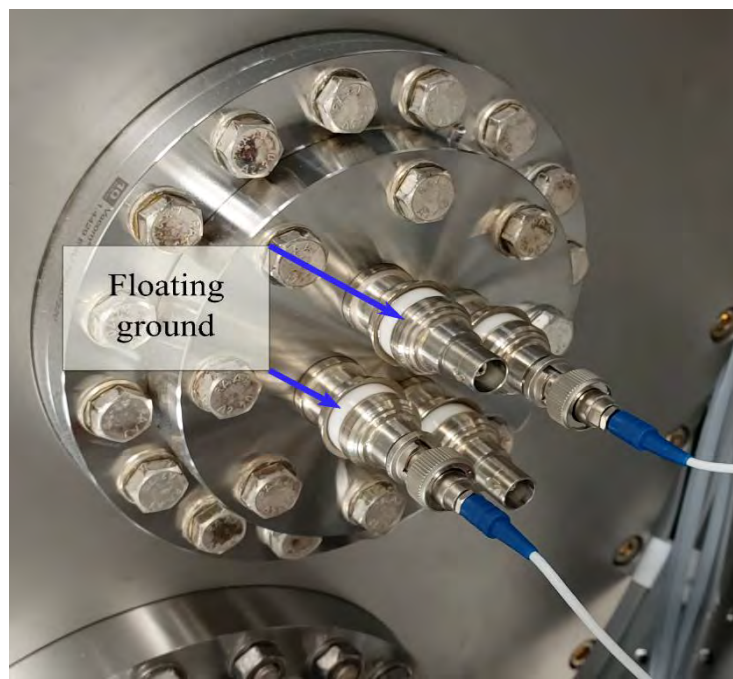


Figure 3.5. Feed-through CF flange. Floating ground has been used to isolate the signal from the body of the experimental chamber.

The current from the medium under study is very small (on the order of picoAmpere). For detection of such small currents, we use a combination of trans-impedance and lock-in amplifiers. For the trans-impedance amplifier, we use a Variable Gain Low Noise Trans-Impedance Amplifier DLPCA-200, which can provide

a gain of up to 9 orders of magnitude<sup>21</sup> (which has amplification bandwidth of 7 kHz). Since the amplifier also amplifies all the noises we use a distorted lock-in measurement. In these kinds of measurements, we modulate the signal with a lower frequency than its rep-rate and lock-in to the frequency of modulation. Due to the fact that lock-in amplifiers integrate the signal with a sine pulse of the same frequency [108], the measured signal would be the difference of the changes of the signal due to the modulation. This difference measurement scheme removes most external noises present in the system.

To modulate our signal, we change the CEP of each neighboring pulse from 0 rad to  $\pi$  rad by the DAZZLER. Because a CEP change by  $\pi$  rad changes the sign of the signal the difference measurement in lock-in will result in doubling the signal amplitude.

To further increase the signal amplitude, we read the signal from two electrodes that are placed on the opposite side of each other with the dipole in their middle. Since the electrodes will be charged with opposite charges, subtracting the measured currents from both electrodes doubles the signal. Further details of this detection method are provided in appendix A.

### 3.3.2. Streaking

The gas we used in this thesis for attosecond streaking is neon. Ionized electrons from neon are collected by a TOF from Stefan Kaesdorf (Kaesdorf ETF11). It is 43 cm long with a MCP to detect electrons. The working voltage of the MCP is 2.15 kV. With this high voltage we cannot increase the pressure of the neon jet beyond the value of  $P_{\text{TOF}} \leq 2 \times 10^{-6}$  mbars, otherwise, electric sparks from the neon gas itself would damage the MPC. For our beamline, this corresponds to a backing pressure of 80 mbars for the gas nozzle.

Data from the MCP are amplified by a 25 dB RF-amplifier and sent to a 100 ps per time bin, multiple-event time digitizer (MCS6A, Fast ComTec GMBH). The MCS6A provides the delay time from the triggering event. The normal acquisition delay that we use is about 21235.2 ns.

For measuring the time of flight of electrons, the zero-channel of electrons has to be found first. The zero-channel is the first spike that appears on the data of the MCP (figure 3.6). It is from the scattering of the XUV photons from the nozzle that reaches the MCP. Since the TOF is 43 cm long, it takes 1.4 ns for these photons to reach the MCP. This is equivalent to 14 amount of time bins on the MCS6A. So, the following equation would give the time of flight of the electrons:

$$t_{\text{TOF}} = (Ch - Ch_0 - 14) \times 10^{-10} \text{ s} \quad 3.2$$

where Ch is the channel number of the electrons and the  $Ch_0$  is the zero channel.

There is an electron lens in the TOF which based on its voltage can focus the electron beams of a certain energy range. Based on the value of the voltage, there are calibration curves that can be used to map the time of flight of the electrons to their kinetic energy (figure 3.7 shows the calibration curve for the 200 V lens value). From the kinetic energy, we calculate the final velocity, and then we can find out the full information about the vector potential and consequently the electric field of the driving pulse.

---

<sup>21</sup> Highest achievable amplification is  $10^{11}$  but it only has 1 Hz bandwidth of amplification which is not ideal for our case where the rep-rate of laser is 3 kHz

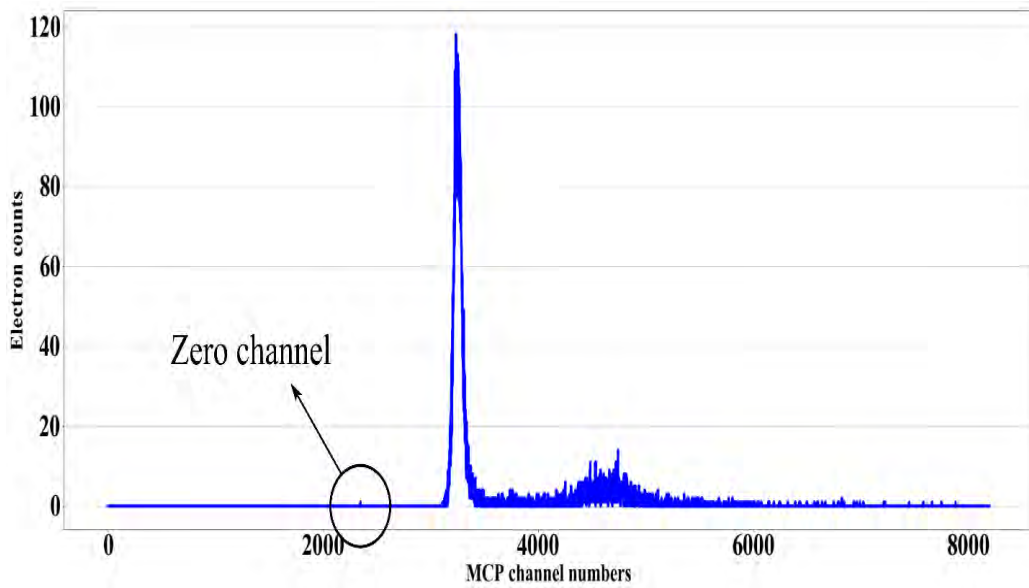


Figure 3.6. Electron counts vs TOF channels. The first spike at the 2346<sup>th</sup> channel is the zeros channel of electrons. For example, the time of flight of the maximum electron counts at the 3234<sup>th</sup> channel, according to Eq. 3.2 the time of flight is  $t_{TOF} = 87.4 \text{ ns}$ . Based on the calibration curve for 200 V of lens this time of flight corresponds to the kinetic energy of 52.5 eV.

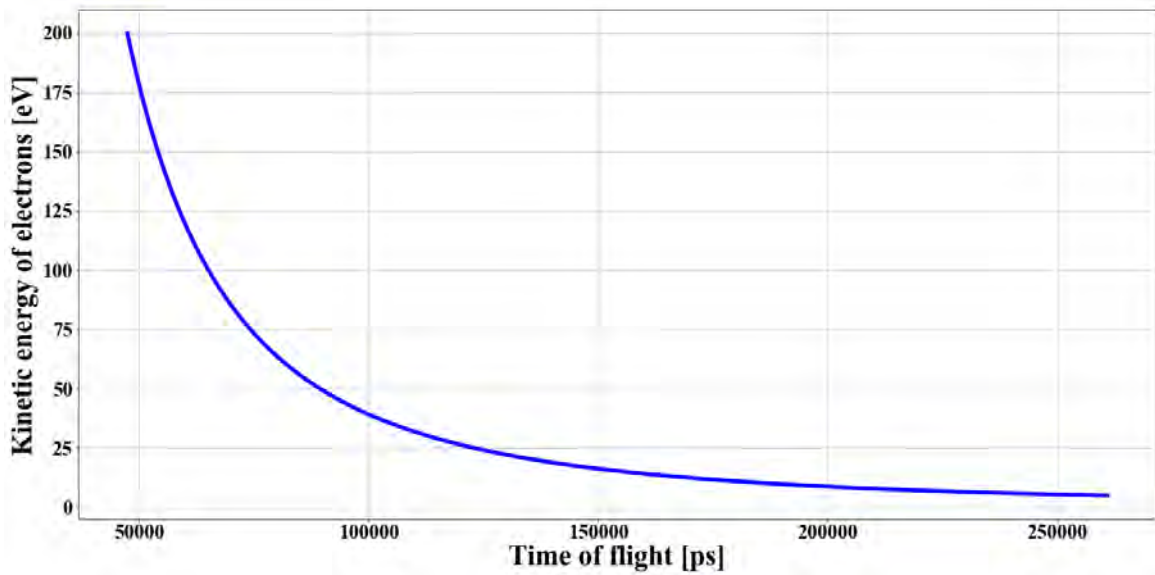


Figure 3.7. Calibration of electron kinetic energy with the time of flight at 200 V of lens. It should be noted that the drift tube of the TOF should be off for this calibration to be used.

## 3.4. Experimental procedure

In this section, we will describe the measurement procedure for the streaking and the photo-conductive sampling. Like in the previous sections, each of these techniques has its own separate subsections for the description.

### 3.4.1: Streaking

An attosecond streaking experiment is a pump-probe measurement. An isolated XUV pulse is the inject pulse and the few-cycle NIR pulse is the probe. The spatial and temporal overlap between the injecting and the driving pulse is made possible by the NIR leakage from the harmonics target. For this purpose, the filter wheel on the injecting arm is set to the no-filter position.

After overlaps are set, the CEP of the pulse should be tuned such that the spectrum of the transmitted XUV photons has no modulation in the cutoff region. This means the NIR pulse that generates harmonics is a cosine-like pulse (i.e. CEP = 0).

### 3.4.2. Photo-conductive sampling

The linear petahertz photo-conductive sampling (LPPS) experiment procedure is almost similar to the attosecond streaking measurement. The main difference is that in streaking we are interested in the XUV photons of the cutoff region (in the case of AS2000 with argon as HHG gas it's about 70 eV photons). On the other hand, in the case of photo-conductive sampling, the situation is different. It turns out (check section 4.2) that we need to use low-energy photons near the energy of the bandgap of the medium (9 eV for SiO<sub>2</sub>, 13.6 eV for LiF). Therefore, to maximize the counts of these photons we need to phase-match for low energy harmonics. We know that to phase match low energy photons we need to increase the argon pressure in the HHG target. We found out that the perfect backing pressure of the target for the generation of these photons is 70 mbars.

Another difference in these measurements is that we need to remove our XUV filters to see the signals since we don't have any good XUV filter for regions between the 9 and 13.6 eV, since none of our filters have transmission below 21 eV.

# 4. LPPS in solids

One of the main topics that we want to understand in this thesis is how ultra-fast electronic wave-packets are driven in by optical transients in solids. One of the established methods for the study of these currents is NPS. In NPS an ultra-short nonlinear interaction creates carriers in the CB and VB of a large bandgap material and a delayed weak field optical transient drives these carriers. Extracting full information about these currents requires a well-understood initial condition of the Bloch waves in CB. The nonlinear nature of the injection in NPS doesn't provide such conditions (see section 1.3). To simplify these complications, we proposed ultra-fast linear injection. Linear injection with high energy photons (i.e. above 9 eV) has two additional advantages: 1) the complete decoupling of the injecting and the driving step. This will remove the necessary condition that injecting and driving pulse should be orthogonally polarized. 2) The injection step does not damage the sample. In this section, we shall investigate how this experiment works and provide results for bandwidth and dynamic range of the photo-conductive sampling by linear injection.

## 4.1: Theory of ultra-fast currents

The HHG radiation that we generate has an energy bandwidth from 1.57 to 70 eV. This bandwidth is large enough to inject electrons from the VB of large bandgap materials to their CB. Since the injection is linear<sup>22</sup> and the dispersion relation for the bands in LiF and SiO<sub>2</sub> is symmetrical for both negative and positive  $k$  points, we shall have a symmetrical population of electrons around  $\Gamma$  point in CB and also symmetrical holes distribution around the  $\Gamma$  point in VB (figure 4.1). Since the group velocity of the electrons in a symmetrical band structure is opposite for the different signs of  $k$ , a symmetrical electron-hole population around  $k = 0$ , will result in no currents [see Eq. 2.31].

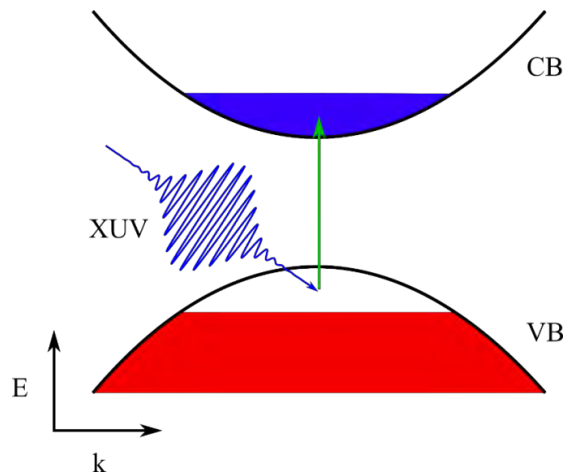


Figure 4.1. Linear photo-injection. In a large bandgap system (i.e.  $E_{gap} > 9$  eV). Populating the conduction band with charge carriers can be achieved by dipole transition using high-energy photons ( $E_{\gamma} \sim E_{gap}$ ). The red shaded area is the states that have electron population in VB and the white area is where the holes are. The blue shaded area in CB is where the electrons from the VB were transited to. While the population carriers in the CB can easily make the solid conductive, it cannot create any current by itself. Since the population of the charge carriers is symmetric around the  $\Gamma$  point of the band structure.

<sup>22</sup> It should be emphasized here that the lack of symmetry of the carrier distribution is the cause of the total net current. There are cases such as the photovoltaic effect where linear photo-injection creates currents. The difference is that due to breakdown spatial symmetry at the PN junction the injected photo-carrier will experience an electric field and flow through the barrier from P side to N and the respective hole will flow in a reverse way.

If an optical field interacts with this system, then according to the Bloch acceleration theorem, it can move the distribution of the charge carriers away from the  $\Gamma$  point (figure 4.2). The resulting asymmetry in the population distribution means that the sum over  $k$  vectors in Eq. 2.31 will not cancel out, which in return means we will have a light-driven current.

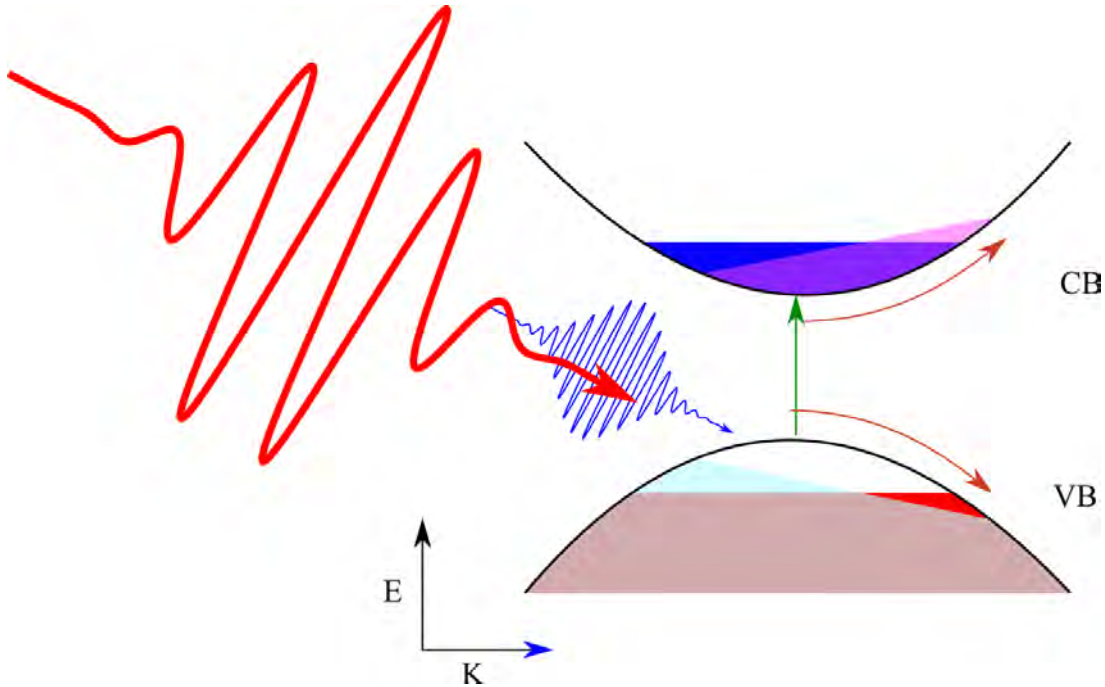


Figure 4.2. The two-color scheme for the creation of ultra-fast currents in large bandgap solids. The high-energy photons (the blue field) will create some population in CB (blue shaded area in CB) and leave some holes in the VB initially (white area in VB).

Then a secondary field (the red field) will move the charge carriers in both valence band (light blue shaded area shows how the electrons in VB fill the position of the holes there) and CB (where light violet shaded area shows the journey of the carriers in the CB). The breakdown of symmetry in the population of the carriers with respect to crystal momentum will result in the net value of group velocity for both electrons and holes which in return creates the ultra-fast currents.

In real space, an XUV pulse creates electron-hole pairs in the material. Furthermore, the delayed drive pulse pushes these pairs away from each other. The resulting dipole moment induces some charges on the electrodes that are grounded. As a result of charging the electrodes, a small current is detected by the Ammeter (figure 4.3).

Using some simplifications, we can estimate the size of the induced charges on the electrodes. Let's assume, based on counts of XUV photons on the XUV camera, that we have  $5 \times 10^7$  XUV photons that will be completely absorbed within less than 100 nm a medium like LiF. It is also safe to assume that the coherent buildup of the dipole moments is responsible for the signal. Therefore, any contribution to the final signal should come from the excursion of the charge carriers before any scattering takes place [109]. From the statistical point of view the longest length that a charge carrier can travel before an event of scattering happens is defined as mean free path. In this case looking at the mean free pass of the medium gives us an upper limit of how far electrons can travel away from their initial point, which for the case of the LiF is about 1 nm for electrons<sup>23</sup> which are excited at the bottom of the CB. Therefore, the size of macroscopic dipole is:

<sup>23</sup> It should be noted that this value is for inelastic electronic mean free path[110].

$$D_{\text{tot}} = 5 \times 10^7 \times 1\text{nm} \times 1.6 \times 10^{-19}\text{C} = 8 \times 10^{-21}\text{ Cm}$$

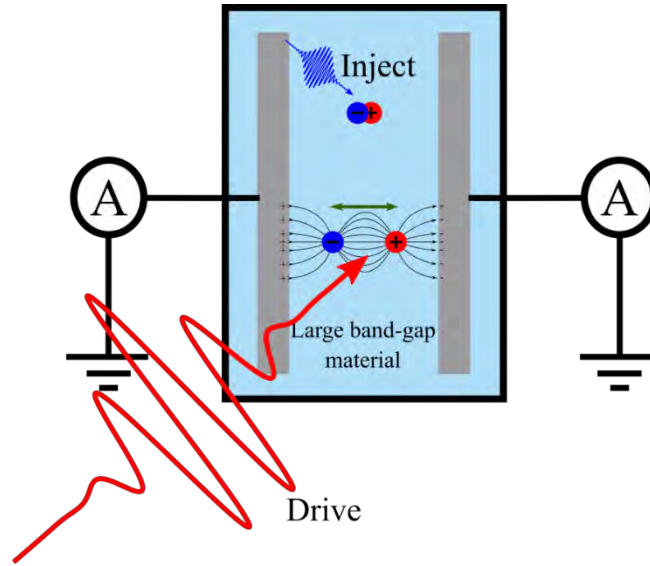


Figure 4.3. Macroscopic picture of the detection of the ultra-fast currents. The VUV pulse separates the electrons hole pairs. Moreover, the NIR pulse pushes these pairs further from each other. The electric field from this dipole is screened by the electrodes. As a result, the electrodes are charged up. Using proper amplification, we can measure the currents that charge up these electrodes.

Using the model of dipole charge between two infinite grounded plates, we can assume that the total induced charge is equal to:

$$Q_{\text{tot}} = \frac{D_{\text{tot}}}{L}$$

where  $L$  is the distance between the total dipole and electrodes. If we assume that this distance is around  $100\ \mu\text{m}$ , then the total charge is about  $Q_{\text{tot}} = 8 \times 10^{-15}\text{ C}$ . For a laser source that has a repetition rate of  $3\text{ KHz}$ , the asymptotic current from charging these electrodes is equal to:

$$I_{\text{asy}} = Q_{\text{tot}} \times 3000 = 12 \times 10^{-12}\text{ A}$$

That's why we use a combination of CEP flipping, trans-impedance amplifiers, and differential lock-in measurements to detect these very weak currents.

## 4.2. LPPS in $\text{SiO}_2$ and $\text{LiF}$

The first sample that we used was non-crystalline  $\text{SiO}_2$  ( $E_{\text{gap}} = 9\text{ eV}$ ). The XUV radiation was filtered by a  $500\text{ nm}$  aluminum filter (transmission bandwidth from  $21$  to  $73\text{ eV}$ ). The immediate observation is that there is no signal. But signal appears by removing the aluminum filter. Since the removal of XUV filter unblocks the NIR in the inject arm as well, we need to confirm that the injection of carriers is not due to

nonlinear transitions from this NIR pulse. Therefore, we block the XUV radiation by turning off the gas jet of the HHG target. We quickly see that the signal vanishes (table 4.1 summarizes these findings). The same results are observed in LiF ( $E_{\text{gap}} = 13.6$  eV) as well.

Table 4.1: dependence of LPPS signal on the injection bandwidth and the HHG gas pressure

Filter	Gas pressure	Spectrum	Signal
<b>500 nm Al</b>	70 mbar	21 to 73 eV	No signal
<b>No filter</b>	70 mbar	1.57 to 73 eV	Signal
<b>No filter</b>	0 mbar	1.57 eV	No signal

To understand this result, we recall that from the theoretical section, the induced drift current is equal to Eq 2.31:

$$\mathbf{J}(t) = \sum_{\mathbf{k}} \sum_n q_n \times \rho_n(\vec{\mathbf{k}}(t)) \times \mathbf{v}_g(n, \vec{\mathbf{k}}(t))$$

This sum is over all the VBs and CBs that contribute to the dipole transition by the XUV pulse.  $\mathbf{v}_g(n, \vec{\mathbf{k}}(t))$  is the group velocity of each band and is proportional to gradient over  $\mathbf{k}$  of the energy dispersion relation of a band:  $\mathbf{v}_g(n, \vec{\mathbf{k}}(t)) = \frac{1}{\hbar} \vec{\nabla}_{\mathbf{k}} \varepsilon(n, \vec{\mathbf{k}}(t))$ . Figure 4.4 shows energy bands and respective group velocity of last 3 VBs (dashed line) and the first 8 CBs (solid lines) of the LiF. Since aluminum filter blocks XUV photons below 20 eV, linear transition happens from VBs to parts of CBs that 20 eV apart (figure 4.5a shows these bands). Let us assume a simple where case where  $\rho_n(\vec{\mathbf{k}}(t))$  is same<sup>24</sup> for bands. If we perform the sum over those bands depicted in figure 4.5a in Eq. 2,31, we get results depicted in figure 4.5b with solid red lines. Comparing these results with the summation over all bands (Blue solid curve in figure 4.5b), we see a slight attenuation of current. Considering 500 nm aluminum filter has transmission of 30 % for photons above 20 eV, we will see that the current attenuates by 75 % (yellow solid curve in figure 4.5b). This picture is flawed because it assumes all the bands have the same charge density. The largest probability amplitude of the transition is from highest VB to the lowest CB, which further suppresses the contribution of currents from upper bands. As a result, the detected current should be only from the contribution of charges in first conduction band.

From this discussion, we conclude that only optical transitions with photon energies equal to the bandgap of the medium result in any measurable microscopic photoconductive optical driven currents. LiF has the

<sup>24</sup> Note that this assumption is made to make the summation over bands easier. Under no physical circumstance, this assumption is true. In dipole approximation  $\rho_n(\vec{\mathbf{k}}(t))$  depends on the magnitude of dipole transition matrix between the state initial state VB and the final state in CB and the occupation number of the final state.

bandgap of  $E_{\text{gap}} = 13.6$  eV. To create electron-hole pairs photons with energy above 13.6 eV are required. These photons lie in the vacuum ultraviolet region (VUV). From now on, we use the term VUV for injections sources in solids.

Using broadband linear injection allows us to properly control the bandwidth of injection through proper filtering and proper phase matching of the harmonics. This is one of the advantages of linear injection over nonlinear injection.

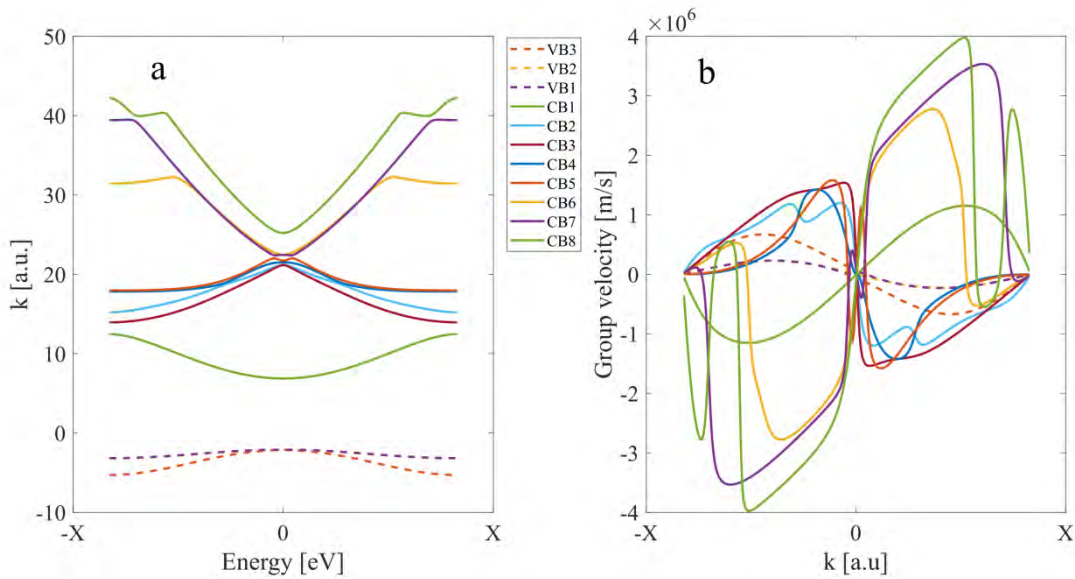


Figure 4.4. Density functional theory (DFT) calculations for LiF band structure along  $x$  cut of the crystal. a) Energy dispersion curve for the last 3 VBs (dashed curves) and first 8 CBs (solid curves) of LiF. b) Group velocity dispersion curve for the last 3 VBs (dashed curves) and first 8 CBs (solid curves) of LiF. The bandgap calculation is courtesy using the Vienna ab-initio simulation package [113]

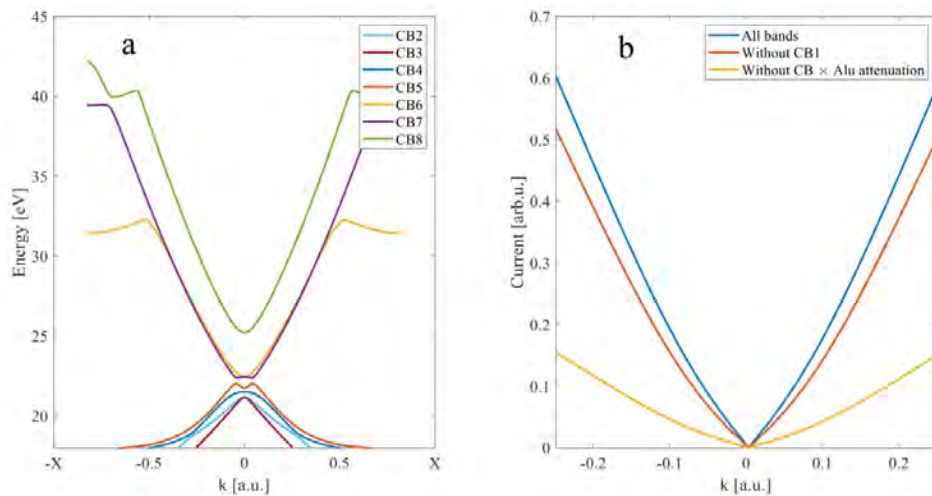


Figure 4.5. Density functional theory (DFT) calculations for LiF band structure along  $x$  cut of the crystal. a) Energy dispersion curve for the last CBs that are 20 eV above the last VB for LiF. b) Summation of the current contributions for all bands (blue curve), for all bands except CB1 (red curve) and for all bands except CB1 times the attenuation by aluminum filter. The bandgap calculation is courtesy using the Vienna ab-initio simulation package [113]

### 4.3. Benchmarking of LPPS in solids vs attosecond streaking

As we discussed before, the signal is only due to the injection of carriers in the first CB. If the dispersion relation in the first CB is parabolic, then according to Bloch theorem, the evolution of the group velocity of the carriers in an external field is proportional to vector potential of that field:

$$\left. \begin{aligned} v_g(\mathbf{k}) &= \frac{1}{\hbar} \nabla_{\mathbf{k}} \varepsilon(\mathbf{k}) \\ \varepsilon(\mathbf{k}) &\propto k^2 \\ k(\tau) &= k(0) + \frac{1}{2} A(\tau) \end{aligned} \right\} \rightarrow v_g(\mathbf{k}) \propto A(\tau) \quad 4.1$$

We can verify this postulate by in-situ measurement of the LPPS and the attosecond streaking (figure 4.6 shows the schematic of this benchmarking experiment).

In this measurement we made sure that the TOF and the gas nozzle are at the same focus as the LPPS sample. The x stage (see figure 3.3) in the experimental chamber moves the nozzle and the dielectric sample across the beam. It is used to put the nozzle of the LPPS sample in the focus. So, for streaking, we push in the nozzle in the focus and for LPPS we push the sample in the focus. The gas that we use for streaking is Ne ( $I_p = 21.52$  eV). For the photoionization we use high pass filtered XUV bursts, which means we again use a 500 nm Aluminum filter.

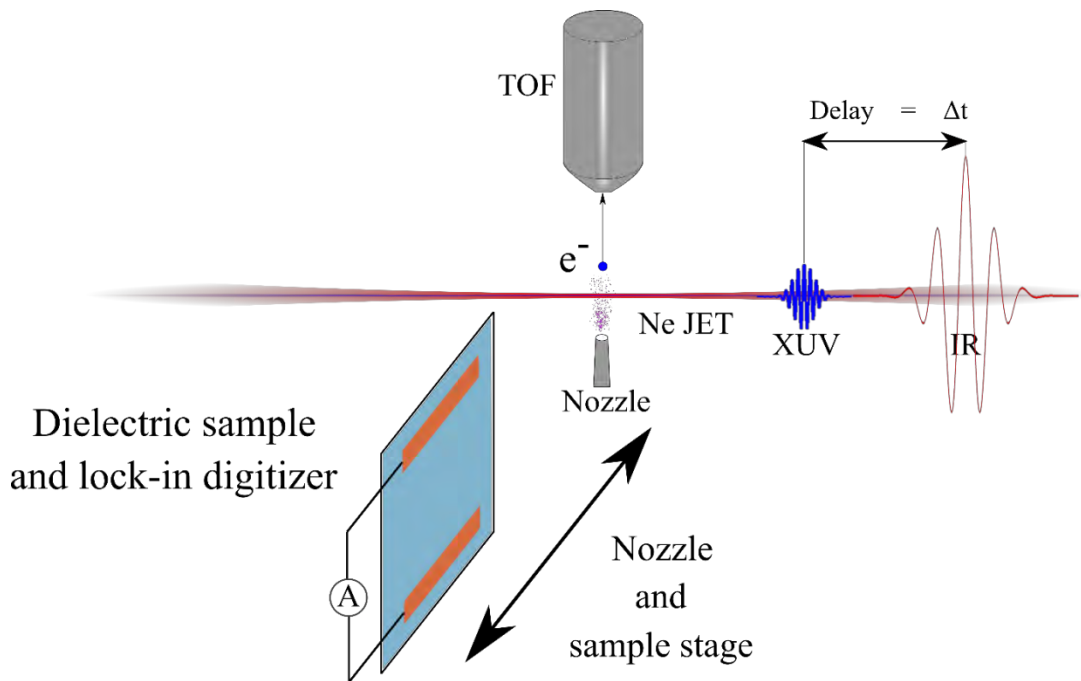


Figure 4.6. Benchmarking setup for LPPS. Benchmarking is performed with respect to attosecond streaking. The gas nozzle and the dielectric sample are placed on a linear stage. When we want to perform streaking, we place the nozzle under the TOF and when we want to perform LPPS we push in the dielectric sample to the same focus under the TOF.

Figure 4.7 shows the result of the benchmarking for the  $\text{SiO}_2$ . We extract the vector potential by means of the center of energy averaging of the harmonic's electron spectra for each delay (black curve in figure 4.7.a). The comparison of the measured vector potential and LPPS current is shown in figure 4.7.b. Both data are normalized to the maximum of their temporal envelope. Since the recorded LPPS currents resembles the streaking data, it proves that the induced currents are in fact proportional to the vector potential of the driving field. The benchmarking for the LiF also shows the same resemblance to attosecond streaking (figure 4.8).

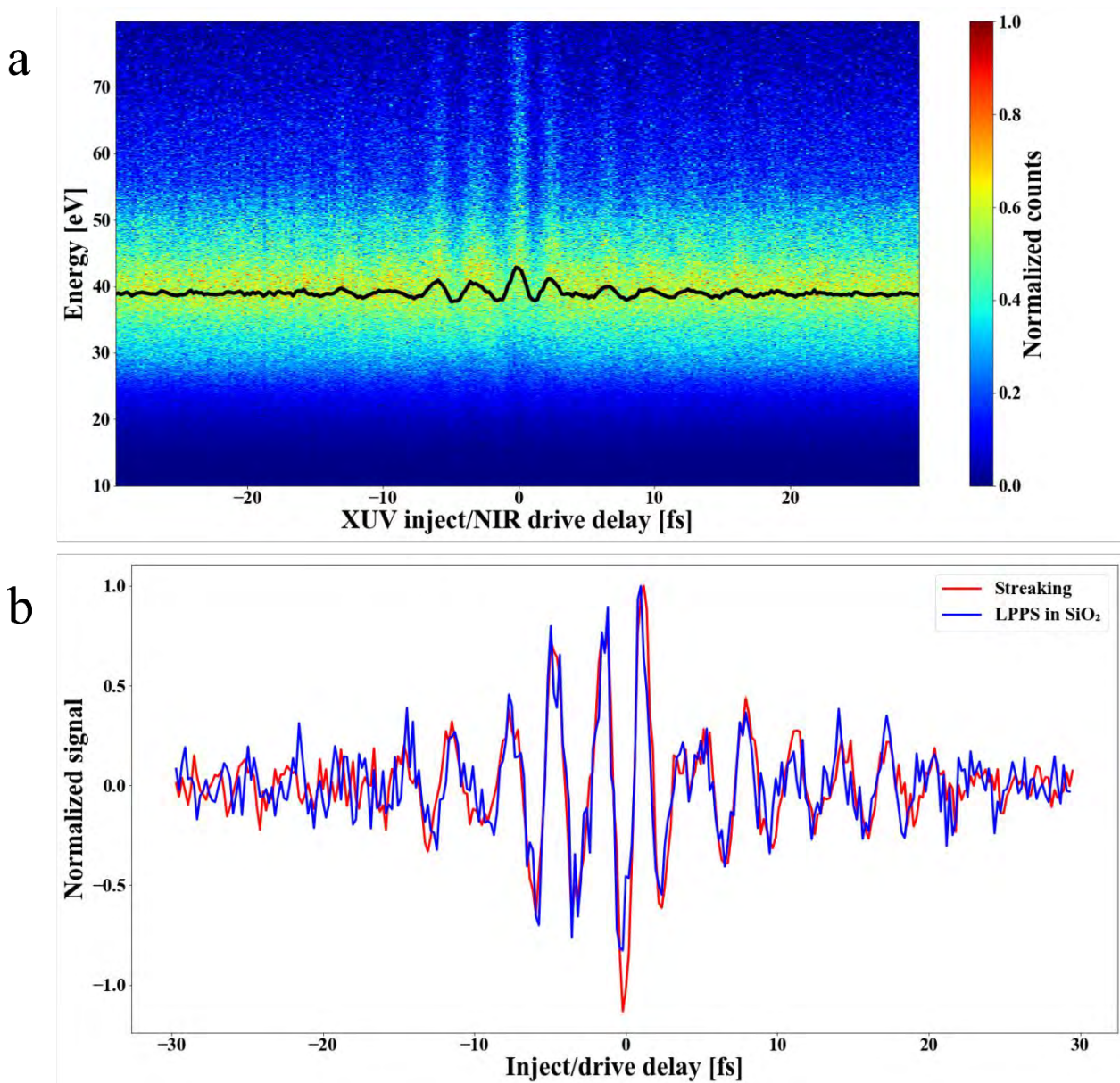


Figure 4.7. Benchmarking of the LPPS in  $\text{SiO}_2$  with streaking in Ne. a) spectrogram of the streaking vs delay. the black curve shows the average energy of the electrons in each delay. this energy has been used to calculate the final momentum of the electrons and as a result the vector potential of the driving pulse. b) comparison of the streaking result (red curve) with the LPPS in  $\text{SiO}_2$  (blue curve)

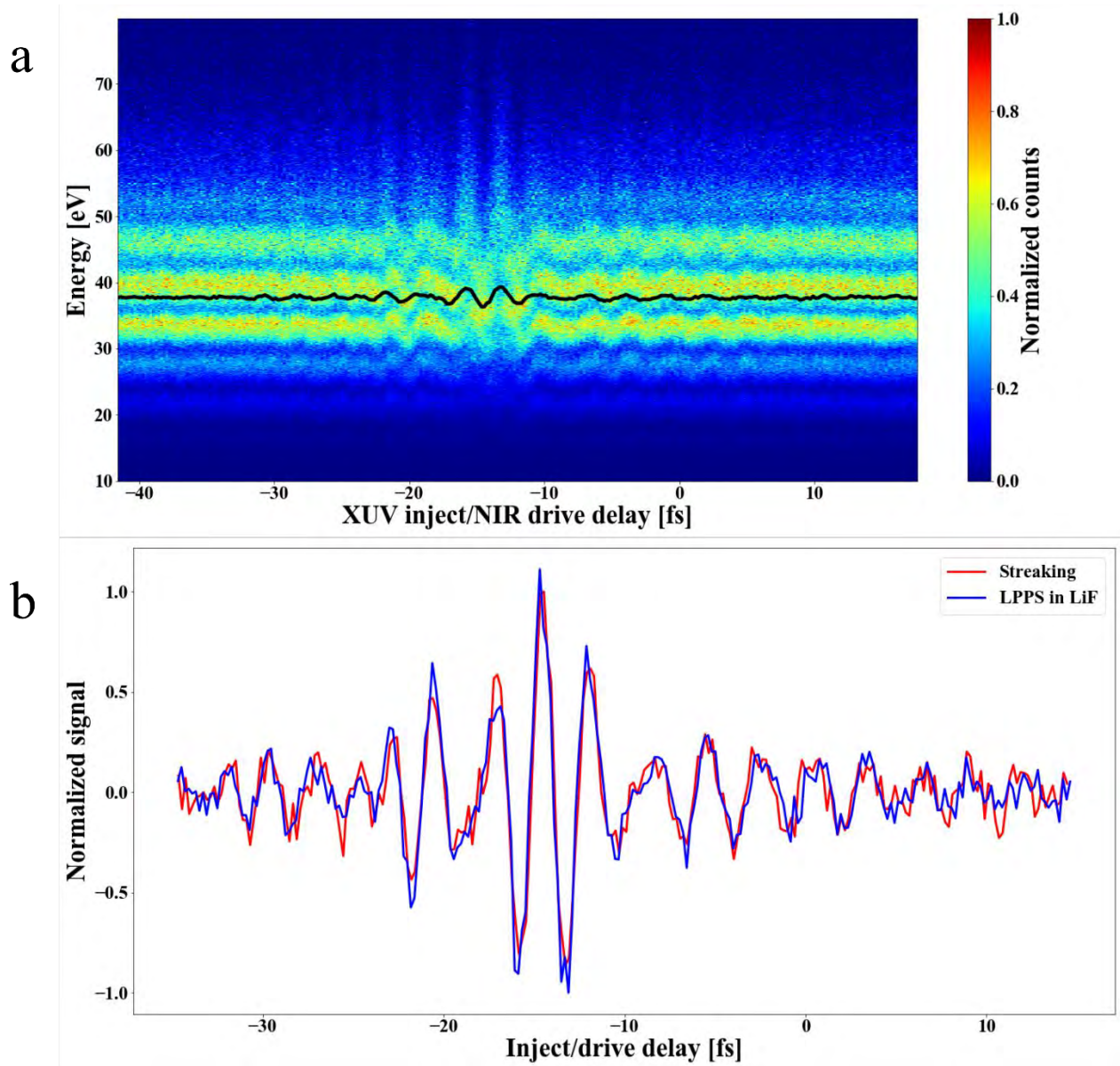


Figure 4.8. Benchmarking of the LPPS in LiF with streaking in Ne. a) spectrogram of the streaking vs delay. the black curve shows the average energy of the electrons in each delay. this energy has been used to calculate the final momentum of the electrons and as a result the vector potential of the driving pulse. b) comparison of the streaking result (red curve) with the LPPS in LiF (blue curve)

#### 4.4. Bandwidth of detection of LPPS in solids

A perfect electric field sampling technique should have a wide bandwidth of detection. The spectrally broadened NIR transient from the HCF has a bandwidth of 1100 to 450 nm. This bandwidth covers more than one octave, which means our multi-layered broadband dielectric chirp mirrors (PC1941), cannot compress the full spectrum. In this case, the cutoff for the compression is 500 nm. To have a good frequency resolution of the NIR transient we must perform a long measurement (500 fs).

First, we compare the results of photo-conductive sampling with a grating spectrometer. We should take note that the measured current is proportional to the vector potential and the measured spectra from the grating spectrometer is proportional to the square modulus of spectral electric field in wavelength. For comparison we need to first find the relation between the spectra of the vector potential and the spectra of the in electric field. Since the electric field is the time differential of the vector potential, we have:

$$E(t) = \frac{dA(t)}{dt} = \frac{d}{dt} \int A(\omega)e^{-i\omega t} d\omega = \int E(\omega)e^{-i\omega t} d\omega \quad 4.2$$

$$\rightarrow E(\omega) = -i\omega A(\omega)$$

For the second problem, we should remember that the amplitude spectral intensity in the range of  $\lambda$  and  $\lambda + d\lambda$  is not equal to spectral intensity in the range of  $\nu$  and  $\nu + d\nu$ , but the sum over the total bandwidth is equal:

$$\int I(\lambda)d\lambda = \int I(\nu)d\nu \quad 4.3$$

Since the spectrum is saved in wavelength, we should do a calibration to turn it into the spectra in frequency, which is as follows:

$$|d\lambda| = \frac{1}{\nu^2} c |d\nu| \quad 4.4$$

$$\rightarrow I(\nu) = \frac{c}{\nu^2} I(\lambda)$$

The next step is then to calculate the square modulus of the  $|E(\omega)|^2$  and compare the normalized behavior of that with respect to the calibrated spectra from the spectrometer.

Figure 4.9 shows this measurement for the  $\text{SiO}_2$ . The blue curve in Fig 4.9.b is the spectral intensity vs frequency of this scan. The red curve is the measured spectrum from a grating spectrometer (MAYA10034 ocean optics). As it is evident there is a clear cutoff at 700 nm. When we replace the  $\text{SiO}_2$  sample with the LiF (13.6 eV) we immediately see that we can extend the bandwidth to 600 nm (figure 4.10).

To understand the reason for the cutoff frequency, we recall that the microscopic current that we measure is a convolution integral of the injection envelope and the driving vector potential [37]:

$$J(\tau) = \int_{-\infty}^{\infty} A(t)W(t - \tau)dt \quad 4.5$$

Convolution theorem states that the Fourier transform of the convolution of two functions is the product of their Fourier transforms, i.e.:

$$J(\omega) = A(\omega)W(\omega)$$

4.6

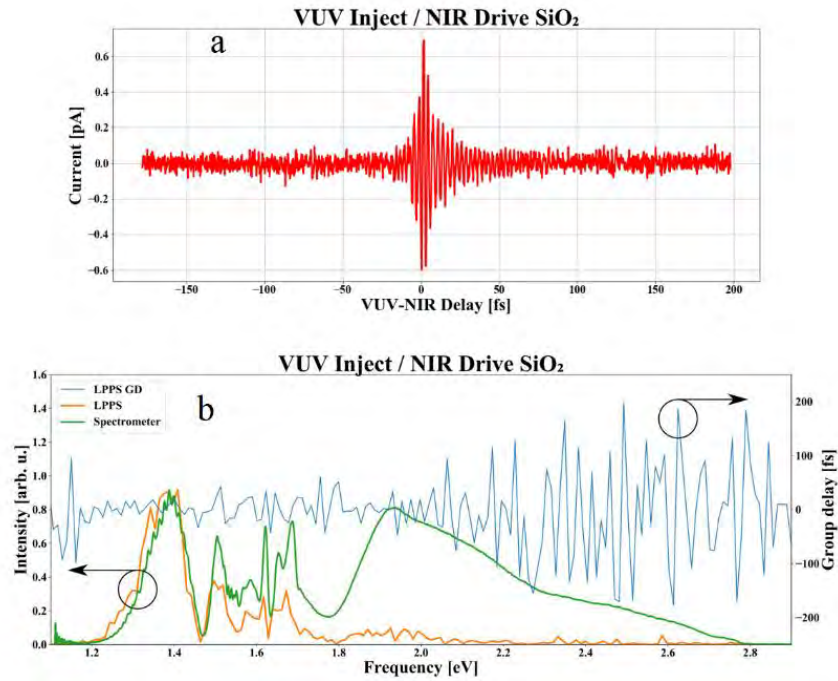


Figure 4.9. Frequency sensitivity of the LPPS in SiO<sub>2</sub>. a) long scan for better spectral resolution. b) Comparison of the spectrum of the NIR field measured by LPPS (orange curve) and the spectrum from the spectrometer (green curve). The right axis is for the calculated group delay of the detected field by LPPS (blue curve).

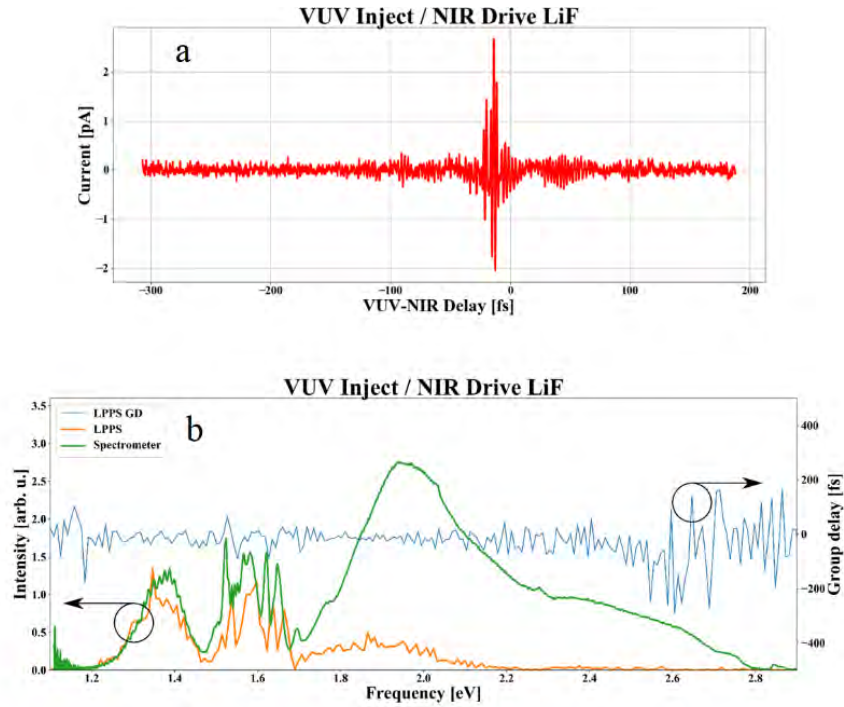


Figure 4.10. Frequency sensitivity of the LPPS in LiF. a) long scan for better spectral resolution. b) Comparison of the spectrum of the NIR field measured by LPPS (orange curve) and the spectrum from the spectrometer (green curve). The right axis is for the calculated group delay of the detected field by LPPS (blue curve).

Therefore, the spectral shape of the injection probability will affect the spectral sensitivity of the detected current.

In the time-domain, this means that, if the injection time is equal to the duration of one complete oscillation of electric field, different parts of the electronic wave packet will experience different signs of the driving electric field which result in a zero sum of group delay [figure 4.11]. This means that if the injection time is longer than one period of electric field the detected current is zero. This is another way to express the Nyquist-Shanon theorem, which says that sampling frequency should be twice the frequency of measured signal [111, 112].

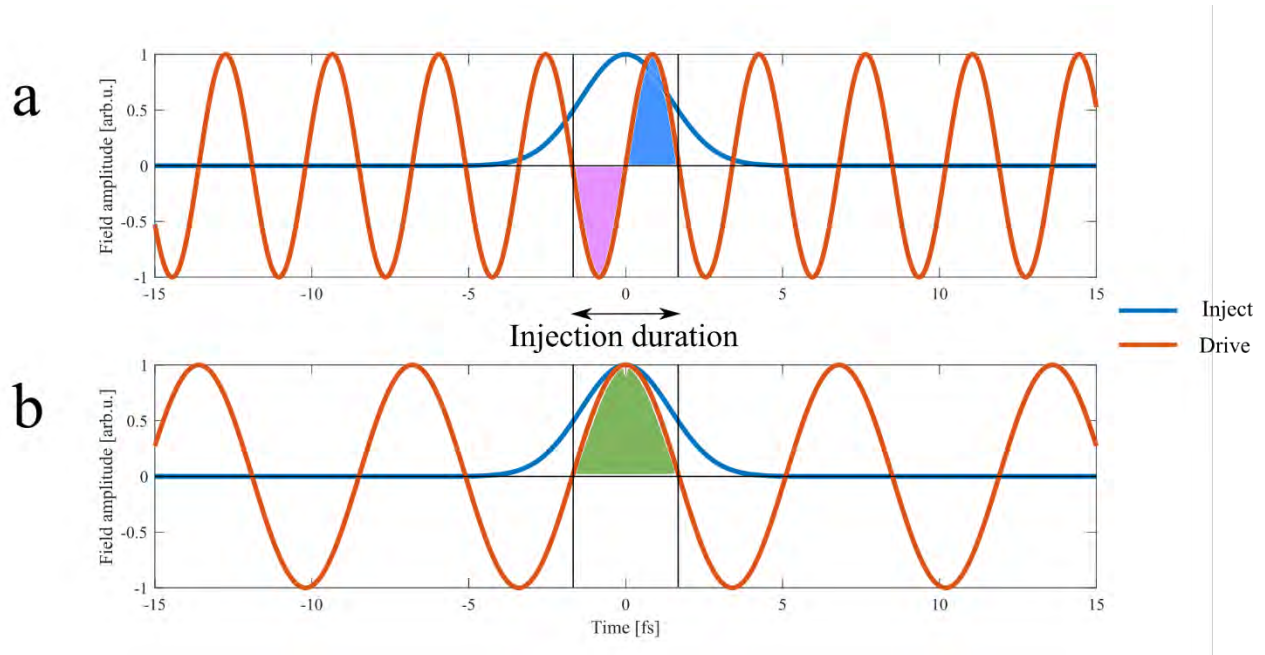


Figure 4.11. Illustration of the effect of injection time on the bandwidth of measurement in LPPS. a) FWHM of the injection envelope (blue curve) is equal to one full cycle of the oscillation of the field (red curve). The half-cycle that is marked by pink shade has a different sign from the one with blue shading. Since both half cycles are summed over in Eq. 4.5, the resulting current will smear out. b) FWHM of the injection envelope (blue curve) is equal to one half-cycle of the oscillation of the field (red curve). This half-cycle is marked by green shade. Since there is no half cycle with opposite under the envelope of injection, we shall have a signal.

Baring this in mind, if we calculate the  $J(\omega)$  from the long LPS measurement and  $A(\omega)$  from the streaking, then we can calculate the  $W(\omega)$ . The inverse Fourier transform of  $W(\omega)$  gives the time-dependent injection probability envelope. The temporal width of this function puts an upper limit for the duration of the temporal domain injection envelope. These calculations in the case of LPPS in LiF have resulted in 1.2 fs injection time. (See figure 4.12)

This is to our knowledge the first demonstration of switching conductivity within one femtosecond by linear absorption. We claim to create an Auston switch with near-petahertz bandwidth, and hence as a consequence, we name the method linear petahertz photoconductive switching (LPPS). In analogy to attosecond streaking [69], the injection pulse duration should be shorter than the duration of half of an optical cycle of the gate field. In our experiment, we find that our method provides a linear transfer of gate signals down to about 650 nm ( $\sim 1.1$  fs half-cycle time), in good agreement with the deconvolution. Beyond this limit, the spectral sensitivity rolls off (take a look at the blue curves for the spectral phase in figure. 4.9 and 4.10) while the temporal phase can be retrieved up to significantly higher frequencies using same methods employed in [37].

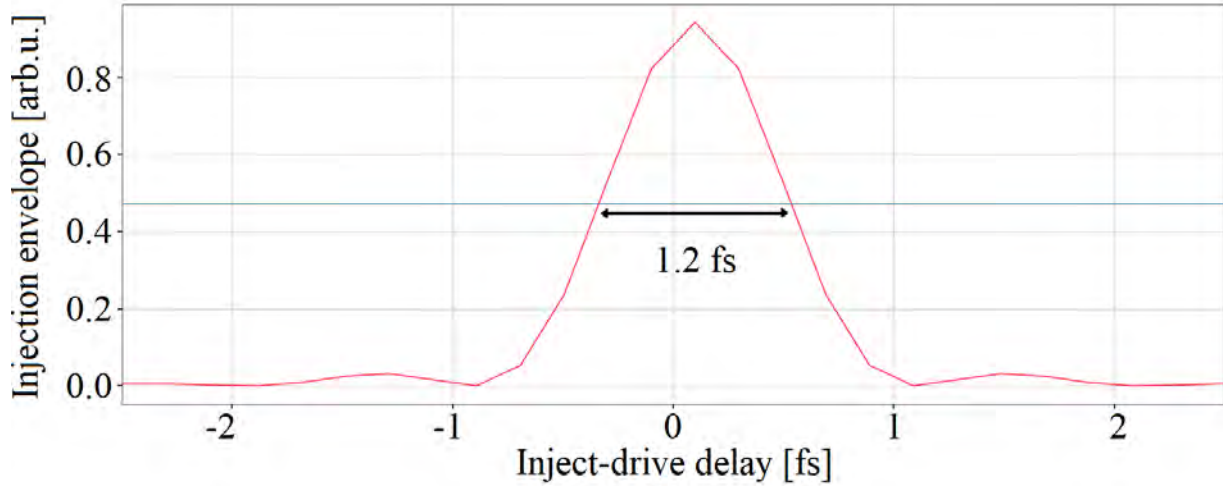


Figure 4.12. Calculated temporal intensity profile of the VUV pulse that injects the carriers into the CB of the LiF.

The experimental results show, that increasing the bandgap of the medium results in the extension of the detected bandwidth. This is a direct consequence of the HHG mechanism, higher harmonics are created by stronger electric fields, and stronger electric-field is confined in shorter time scales. Consequently, the higher harmonics inherit this shorter generation duration.

## 4.5. Dynamic range of LPPS in solids

Next, we investigate the dynamic range of this measurement technique. We need to determine the lowest and highest limit of linear field measurement. The noise floor of the measurement limits the lowest detectable field strength. On the other hand, finding the upper limit is easier. The first detectable deviation from linear behavior:

$$S(\tau) = J(\tau) - J_{\text{ref}}(\tau) \quad 4.7$$

, can be regarded as the upper limit of the dynamic range.

For the determination of the dynamic range, we need to change the amplitude of the driving field. This is done by opening and closing an iris in the delay arm of the Delay chamber.

We mentioned before that LPPS current in both LiF and SiO<sub>2</sub> comes from the photo-conduction by VUV photon which energy bandwidth around energy band-gap of these solids, i.e. 13.6 eV and 9 eV. Finding a proper filter to select these photons with transmission above 10 % is impossible. Therefore, we didn't use any filter. As a result, the NIR transient, which generates the vacuum ultraviolet (VUV) source is present at the point of measurement, with the field amplitude of 0.08 V/Å. In total, we have the injecting VUV photons plus the driving the NIR photons which come from the Delay arm and the NIR photons from the VUV arm. For the power scan of LPPS current traces of the NIR driving field, we need to ensure that the NIR field itself does not inject any charge carriers nonlinearly. For this purpose, we perform two measurements in the following order, 1<sup>st</sup>) the LPPS current is measured when the VUV and NIR in the VUV arm and the NIR in the delay arm are impinged on the sample, 2<sup>nd</sup>) the LPPS current is measured when only the NIR in the VUV arm and the NIR in the Delay arm are impinged on the sample. Then the current from the second

measurement is subtracted from the first measurement. We postulate that this subtraction reduces the effect of the photo-carriers injected by nonlinearly by the NIR in the drive arm on our result. The reason can be seen by examining Eq. 4.5. From the three available fields in this experiment, the VUV field and the NIR field in the Delay arm can inject carriers. Thus, the total injection probability,  $W_{\text{tot}(t)}$ , consist of two terms: the injection probability from the VUV by  $W_{\text{VUV}}(t)$  and the nonlinear injection probability by the NIR field in delay arm as  $W_{\text{NIR}}$ , i.e.  $W_{\text{tot}(t)} = W_{\text{VUV}}(t) + W_{\text{NIR}}(t + \tau)$ . The total vector potential that steers the electrons  $A_{\text{tot}}(t)$  also consists of two parts: the vector potential of the NIR in the VUV arm,  $A_{\text{NIR-VUV}}(t)$ , and the vector potential of the NIR field in the Delay arm,  $A_{\text{NIR-delay}}(t)$ , i.e.  $A_{\text{tot}} = A_{\text{NIR-delay}}(t) + A_{\text{NIR-VUV}}(t - \tau)$ . By inserting these defined terms for  $A_{\text{tot}}$  and  $W_{\text{tot}(t)}$  in Eq. 4.5 we have:

$$J_1(\tau) = \int_{-\infty}^{\infty} [A_{\text{NIR-delay}}(t)(W_{\text{VUV}}(t - \tau) + W_{\text{NIR}}(t)) + A(t - \tau)_{\text{NIR-VUV}}(W_{\text{VUV}}(t - \tau) + W_{\text{NIR}}(t))] dt \quad 4.8$$

This integral is for the case one. For the case two we set  $W_{\text{VUV}}(t)$  to zero. Therefore, we have:

$$J_2(\tau) = \int_{-\infty}^{\infty} [A_{\text{NIR-delay}}(t)W_{\text{NIR}}(t) + A(t - \tau)_{\text{NIR-VUV}}W_{\text{NIR}}(t)] dt \quad 4.9$$

Then subtracting the current from both measurements will result in:

$$J(\tau) = \int_{-\infty}^{\infty} [A_{\text{NIR-delay}}(t)W_{\text{VUV}}(t - \tau) + A(t - \tau)_{\text{NIR-VUV}}W_{\text{NIR}}(t - \tau)] dt \quad 4.10$$

The first term in the integral Eq. 4.10 is the current that we would like to measure and the second term adds a constant offset to the current. In this manner, it is made sure that any contribution to the final result of the power scans current measurements is due to linear injection of the carriers to CB.

Figure 4.13 shows the results of the power scans. The reference scan at  $0.12 \text{ V/\AA}$  average power is benchmarked again a streaking measurement, and the rest of the scans are normalized according to their respective field amplitude vs the reference scan. The shaded area in the plots depicts the deviation currents,  $\Delta S(\tau)$ , from each power with respect to the reference scan. It is evident that with increasing NIR field amplitude, the difference between the measured current and the reference current increases.

The study of these delay-dependent discrepancies shows that there are two types of differences. The type 1s differences are those that increase with the amplitude of the vector potential, and type 2s differences are those that do not appear at the extrema of the vector potential.

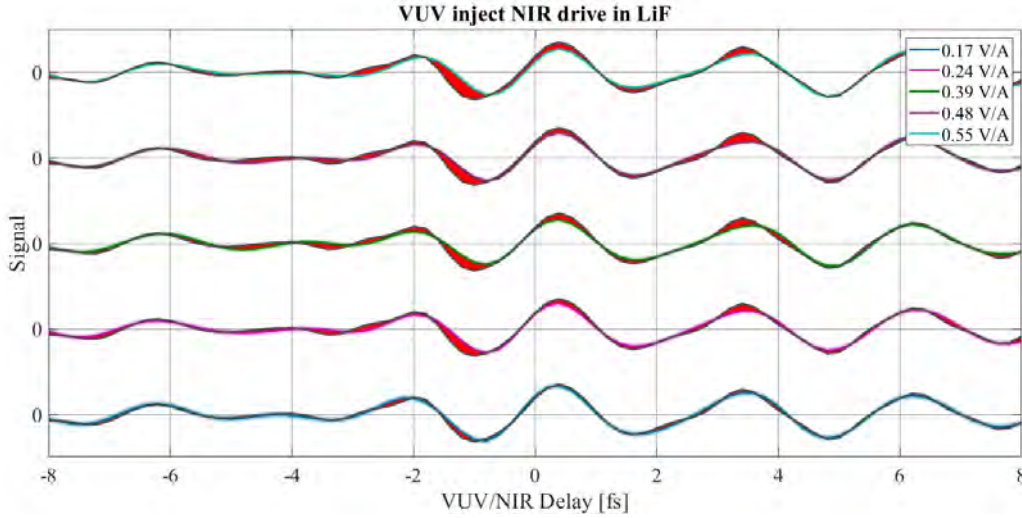


Figure 4.13. Intensity-dependent LPPS measurements in LiF. The current due to different field amplitude are depicted by different colors and the reference scan is depicted by grey color. The shaded areas show the deviation of the currents vs the reference scan.

To understand the type 1 discrepancies, we should investigate Eq. 2.31 again. In this equation, the current is proportional to the group velocity of the electron Bloch wave packet,  $\mathbf{v}_g$ . Remember that we explained that the changes in  $\mathbf{v}_g$  are proportional to vector potential if the dispersion of CB is parabolic, i.e.  $\mathcal{E}(k) \propto k^2$  (Eq. 4.1). If the NIR field drives the Bloch wave to non-parabolic parts of the CB then  $\mathbf{v}_g$  will deviate from the vector potential of the NIR field. Therefore, stronger fields lead to bigger discrepancies in current vs vector potential. This intra-band current contribution, due to the flattening of the dispersion, results in the reduction of the height of the peaks of the LPPS signal with an increase of the driving field strength. As this effect depends only on the instantaneous vector potential  $A(\tau)$  at the moment of carrier injection, due to the Bloch theorem, it should be most pronounced at the strongest driving field vector potential extrema.

Let's first consider only this mechanism for the current deviations from linear behavior. So, the assumption is that we fill some states symmetrically in the CB and move the electrons around the  $k$  points in the reciprocal lattice. If we only have one electron that is placed in the  $\Gamma$  point of the band, how strong should the electric field be to drive this electron into the non-parabolic regions band structure? To answer this question, we should calculate the dispersion relation of the band and use the Bloch acceleration theorem.

There is no proper definition about which range of  $k$  values is considered parabolic. The way we define it is the following: the parabolic region is the region where the difference between the group velocity of the actual band and the parabolic band is less than 15 percent group velocity of the parabolic band (this is number is based on our experimental results, see figure 4.14) of the actual group velocity of the parabolic band:

$$|V_g(k)_{\text{Lif}} - V_g(k)_{\text{parabola}}| \leq 0.15 \times |V_g(k)_{\text{parabola}}| \quad 4.7$$

Applying this formula to the dispersion relation of LiF, calculated by DFT for the X cut direction<sup>25</sup>, we find that if we move by  $\Delta k = 0.4$  a.u., we go out of the parabolic region (figure 4.15). Using the Bloch acceleration theorem, we find out that any field amplitude above the  $2.3 \text{ V/\AA}$  drives the electrons out of the parabolic region.

<sup>25</sup> This calculation is done in the local-density approximation (LDA) using the Vienna ab-initio simulation package (VASP)[113]

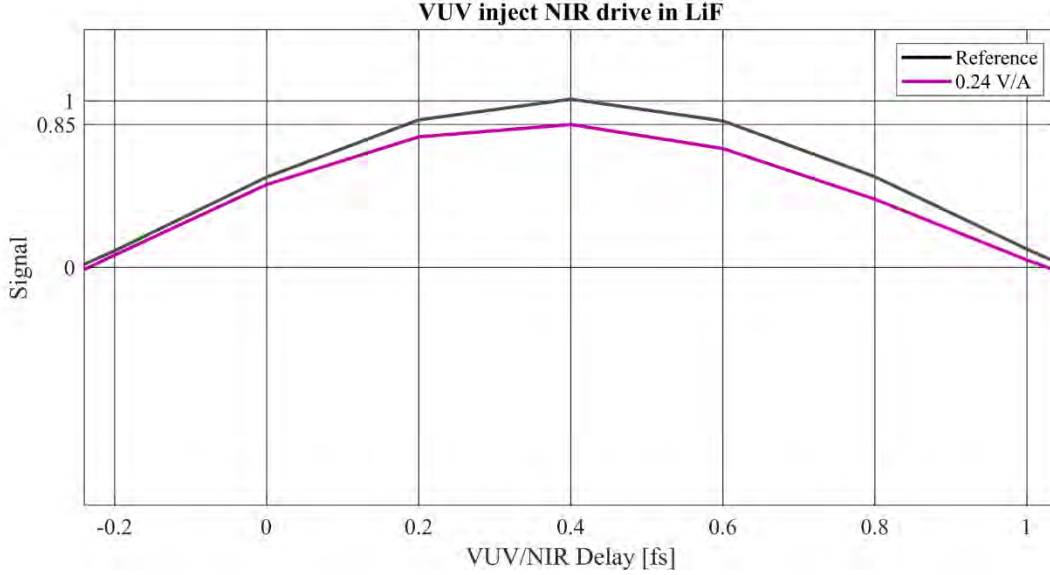


Figure 4.14. Deviation from vector potential at driving field amplitude of  $F_{drive} = 0.24 \text{ V/\AA}$ . Almost 15 percent deviation of current (pink curve) is observed at the position of the maxima vector potential (dark grey curve). This value is used to calculate the extent of the parabolic region of CB in LiF. The bandgap calculation is courtesy of using the Vienna ab-initio simulation package [113].

$2.3 \text{ V/\AA}$  is a huge amplitude. Our data shows that deviations already start at field amplitudes of  $0.24 \text{ V/\AA}$ . This huge difference is due to the fact that we only considered one electron occupying the  $\Gamma$  point of the CB of the LiF. Considering that XUV radiation has a large bandwidth we know that CB cannot only be filled at the  $\Gamma$  point.  $0.24 \text{ V/\AA}$  can add  $\Delta k = 0.04 \text{ a.u.}$  to the crystal momentum of the electronic wave packet. If a  $k$  value of  $0.4$  is the edge of the parabolic region, then it means that the last occupied electronic state from XUV transition should be filled at  $k_{ini} = 0.36 \text{ a.u.}$ . According to the dispersion relation of the LiF this state should have energy of  $E(k_{ini}) \approx 8.6 \text{ eV}$ . The lowest point of the CB (i.e.  $\Gamma$  point) for the LiF has energy of  $E(\Gamma) = 6.87 \text{ eV}$ . Therefore, the range of energy that promotes the electrons population in the CB of LiF is about  $\Delta E = 8.6 - 6.87 = 1.73 \text{ eV}$ . Translating this to photon energies we find that we shall have:

$$\Delta E_{\gamma}(13.6 \text{ eV}) = 1.73 \text{ eV}$$

This roughly means that the Fourier limited duration of the injection around  $13.6 \text{ eV}$  photons is:

$$\Delta t_{inject} \approx 1.3 \text{ fs}$$

This result is in good agreement with our calculations of the injection time in the previous section. The difference can be attributed to the fact that in this analysis we consider that the population from the  $\Gamma$  point to the highest filled state at  $k = \pm 0.36 \text{ a.u.}$  is constant.

This result shows that the injection time for the detectable signal is not only dependent on the bandgap of the material. One simply can achieve shorter injection times. The result of such a short injection is that we not only populate the non-parabolic regions of the first CB but also the higher CBs. Both of these in return reduce the amplitude of the current. We find that the extent of the parabolic region is another important factor on the duration of the photo-injection that results in a linear detectable current.

In fact, for coherently manipulating and steering a momentum-non-dispersive Bloch wave packet, only the lower portion of CB1 should be initially populated, reducing the available bandwidth to about half of  $\Delta E_{CB_1}$ .

The observed excitation time of  $\Delta\tau \approx 1.2$  fs in our experiment is indeed consistent with initially populating only the lower half of CB<sub>1</sub>, reconfirming that, future ultrafast optoelectronic devices may be efficiently operated up to frequencies approaching the petahertz frontier.

If we only consider the above reasoning as the source of discrepancies, then we should only see that increasing the drive amplitude will increase the differences. But what we see is that above certain field strength, there are cases that the biggest disagreement between recorded current and the reference current happens right before the maxima of the vector potential of the reference current, i.e. 1.5 fs. This means, there is a second mechanism that affects the induced currents above certain field strength.

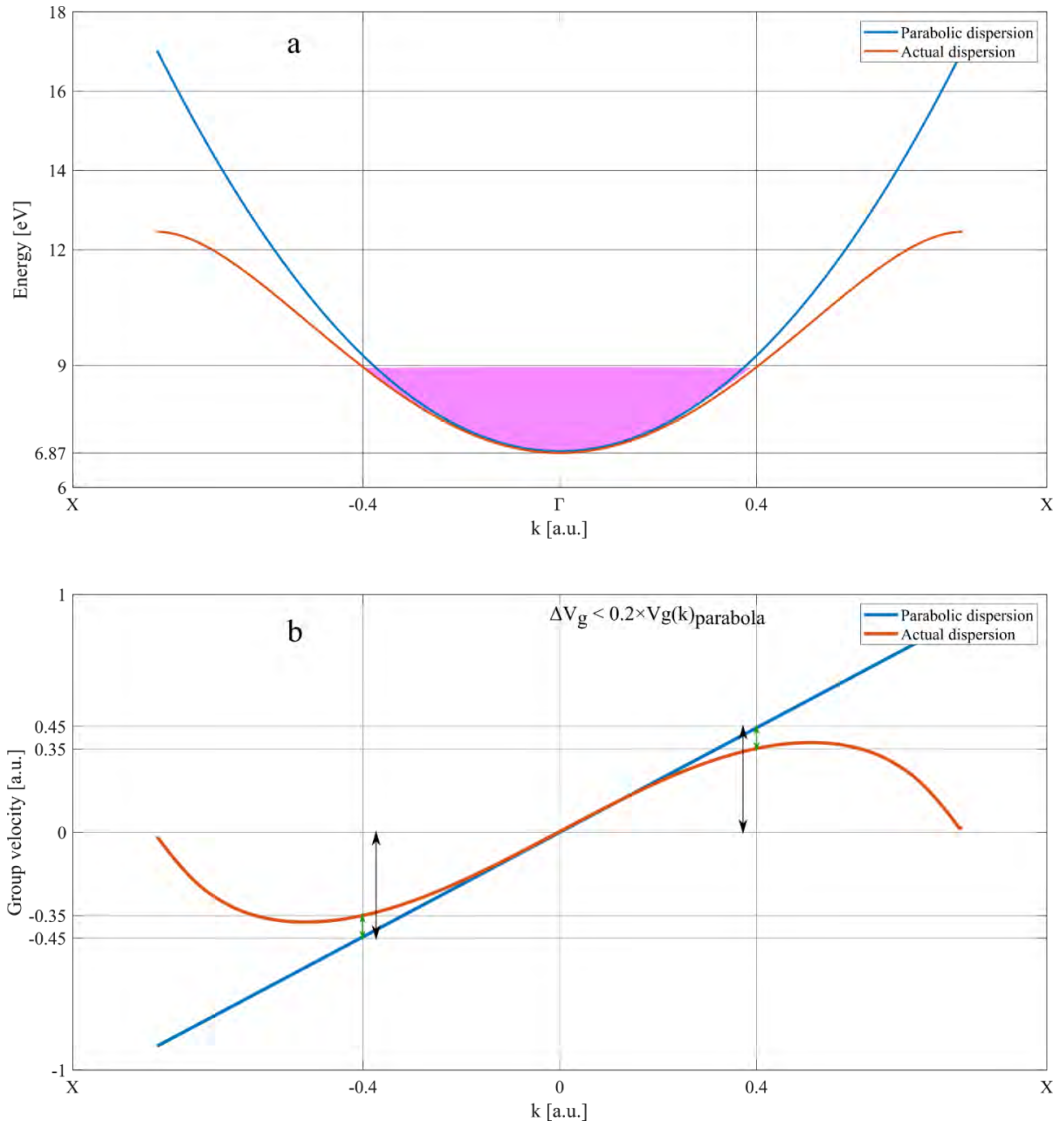


Figure 4.15. The extent of parabolic dispersion region for the first CB of the LiF. a) Energy dispersion of actual band (red curve) vs the parabolic band (blue curve). b) Group velocity dispersion of actual band (red curve) vs the parabolic band (blue curve). The boundary is defined as the k point where the difference between the parabolic dispersion group velocity and the actual band group velocity is below 20 percent. The bandgap calculation is courtesy of using the Vienna ab-initio simulation package [113].

Up to now, we have only considered the Bloch acceleration theorem, when we dealt with the interaction of the NIR field with the electrons in CB. For materials like LiF and SiO<sub>2</sub>, around their  $\Gamma$  point, this is a fair

approximation. Near the  $\Gamma$  point, the energy difference of the first CB and second CB (which from now on we call  $CB_1$  and  $CB_2$ ) are around 7 eV (figure 4.16). This means that if the electron remains in the vicinity of the  $\Gamma$  point, the NIR field cannot cause any transition from  $CB_1$  to  $CB_2$ . But as we have said earlier, if the NIR field drives the electrons further away from the  $\Gamma$  point toward the edges of the Brillouin zone, then there would be a case that the energy difference between  $CB_1$  and  $CB_2$  is going to be comparable to the energy of one photon transition from the NIR field.

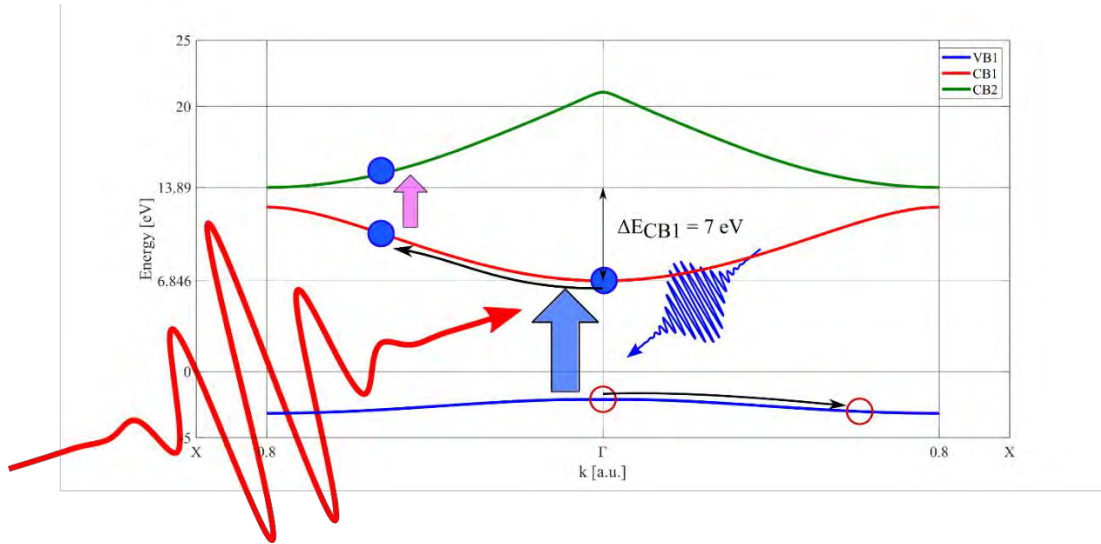


Figure 4.16. Demonstration of the mechanisms that cause deviations from vector potential like the behavior of the optically driven currents. Mechanism one is shown by the black curved arrows. Driving of the charge carriers toward non-parabolic parts of the CB. Since in these regions the dispersion curve of the band flattens, the group velocity of the wave-packets reduces and as a result, current amplitude is underestimated. Since these currents are due to Bloch acceleration their respective deviations are supposed to increase by increasing the amplitude of the vector potential. Mechanism 2 is shown by the pink arrow. As we drive the carriers closer to the edge of the Brillouin zone, the coupling between the first and the second CB becomes stronger. When the coupling between two bands becomes stronger, the Landau-Zener transition probability increases. Since this transition is non-zero when both electric field and vector potential are non-zero, the deviation of the current due to these transitions do not occur at the extrema of the vector potential

The group velocity of the  $CB_2$  has an opposite sign of the group velocity of the  $CB_1$  (figure 4.17). Once again, if we use the Bloch acceleration term for the current (Eq. 2.31) for the first two CBs like the following:

$$J(\tau) = \rho_{CB_1} \left( k_0 - \frac{1}{c} A(\tau) \right) \times V_g(k_0 - 1/cA(\tau))_{CB_1} + \rho_{CB_2} (k_0 - 1/cA(\tau)) \times V_g(k_0 - 1/cA(\tau))_{CB_2} \quad 4.8$$

since  $\text{sign } V_g(k_0 - 1/cA(\tau))_{CB_1}$  is opposite of  $V_g(k_0 - 1/cA(\tau))_{CB_2}$ , then the signal gets leveled off with respect to the vector potential.

When the transition is complete and part of the electron wave packet is in the higher bands. Electronic wave packets in all occupied bands will continue to propagate again as the acceleration theorem predicts. Deviations like these are most pronounced in the half-cycle before the highest extrema of the vector potential. These transitions don't happen at points of the vector potential extrema, since these points are

zero crossing of the electric field. If we remember from the theoretical discussions about the Landau-Zener transitions, The probability of the transition is non-zero when both the electric field and the vector potential are non-zero. If we take into account these kinds of transitions then in time the following is the sequence of the things that will happen:

1. Linear injection by XUV photons will put electrons in  $CB_1$
2. Weak half cycles of the vector potential will drive electrons in the parabolic regions
3. Stronger half cycles of the vector potential will drive electrons further into the non-parabolic regions
4. Before the strongest half cycle of the vector potential, electrons can transit into  $CB_2$

The main Landau-Zener transition happens 1.5 fs before the maxima of the vector potential of the NIR field. The half-cycle after this transition is not as significant as before. One reason for this is the existence of the population in the upper band. The existence of electronic population in the  $CB_2$  will reduce the transition probability in this half cycle. Therefore, due to Pauli blocking, the probability of this transition decreases (figure 4.17). Therefore, we don't see much deviation of the second kind after the first deviation happens.

This result can be understood in the following way: in order to have a one-photon transition from  $CB_1$  to  $CB_2$  the electron should be in a position in the band where the energy difference between the two bands is equal or less than the photon energy of the driving field. This point in LiF is located at  $k = 0.7$  a.u.. Based on the Bloch equation amplitude of vector potential that can send the electron from  $\Gamma$  point to  $k = 0.7$  a.u. is about

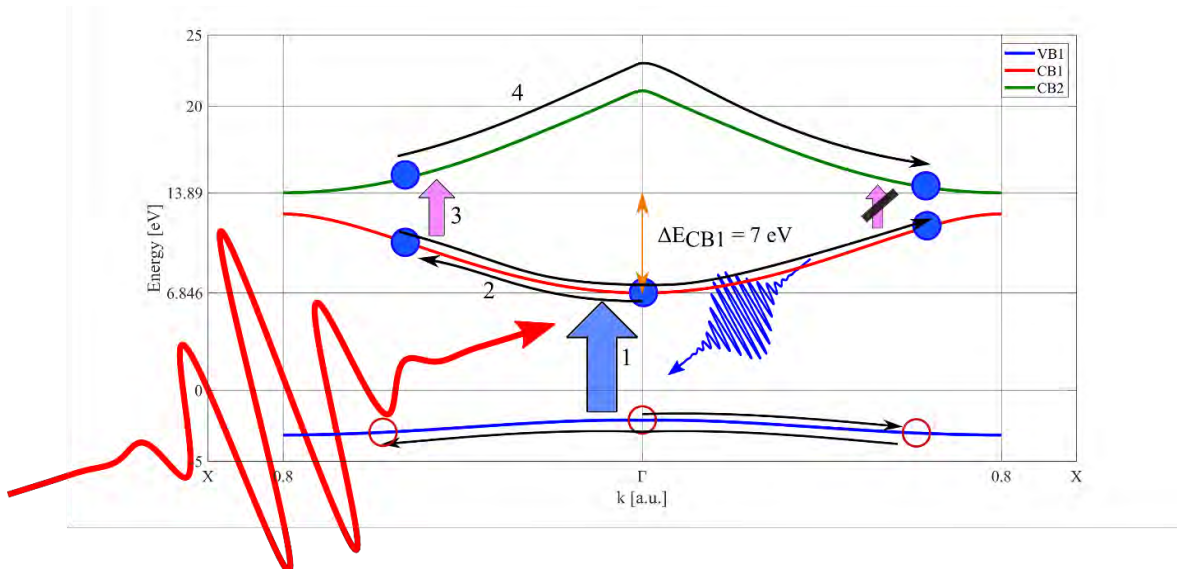


Figure 4.17. All the steps that lead to the final current. Step 1: photoconduction by the XUV pulse creates an electron-hole pair. Step 2: NIR pulse drives the electron and hole in the  $CB_1$  and  $VB$  respectively. Step 3: part of the electronic wave packet is sent to the  $CB_2$  via Landau-Zener transition. Step 4: both parts of the electronic wave-packet are driven to the opposite side of the band structure. Due to the existence of the electron population in  $CB_2$  the transition from  $CB_1$  to  $CB_2$  is blocked. Therefore, we do not see large deviations.

## 4.6. Conclusion of LPPS in solids

From all these results we conclude that steering of linearly induced photo-carriers can result in a measurable macroscopic current if this linear injection is fast. One way to achieve this is to use large bandgap materials. But this is not the full picture for ultra-fast linear switching. Another important condition is a broadband initial spread  $\Delta E$  of the conduction charge carriers. The addition of these two facts together can create enough conditions for a fast switching-time. The speed of excitation build-up alone is controlled by the joint density of states and can include many valence and conduction bands of the active material. However, as observed in the experiment, the occupation of multiple conduction bands will result in the reduction of the magnitude of the detected current. Since different bands have different signs of group velocity for the carriers. Therefore, increasing the bandwidth of linear injection does not necessarily help to achieve a faster switching time. Therefore, a future device should avoid populating multiple conduction bands. It is most feasible to have a large first conduction band and fill only this band for best switching conditions. If the  $CB_1$  is filled it also creates problems regarding current detection. Since steering electronic wave-packet in non-parabolic parts of the CB decrease the current. On the other hand, it will increase the chance of Landau-Zener transition to the upper bands which in return decreases the current further. For the lower frequency component of the driving field, this transition happens closer to the edge of the Brillouin zone than the higher frequencies. Since Landau-Zener transition for higher frequency components can happen closer to the  $\Gamma$  point of the CB, they can only be detected if the population is less broadband. On the other hand, less broadband injection bandwidth means longer injection time which in return limits the bandwidth of detection. We conclude that for better linear switching we need to have larger linear transition energy and a larger extent of the final state. This can only be achieved by inert gases, which will be described in the next chapter.

# 5. LPPS in gases

Our results from LiF experiments suggest that, in order to detect higher frequencies with the LPPS technique, we need to have a shorter injection time as well as a final state with infinite parabolic dispersion relation. Since we cannot push the linear carrier injection time in LiF we need to find another material with higher transition energy. Since LiF has the highest bandgap in solids, we have to use gases for this purpose.

Like in the case of Attosecond streaking, inert gases are perfect candidates. Furthermore, we want to have as high transition energy as possible. Therefore, we choose Ne with Ionization energy of  $I_p = 21.56$  eV In this chapter we will investigate the feasibility of LPPS in neon and present the result of those measurements<sup>26</sup>.

## 5.1 Measurement procedure

The measurement procedure is similar to LPPS in LiF. A few-cycle NIR pulse with the central wavelength of 800 nm and pulse energy of  $E_p = 266 \mu\text{J}$  and pulse duration of  $\tau_p = 4$  fs is split into two pulses. 80 % is focused on a HHG target, to create the source pulse. The other 20% will be sent to the Delay arm, as our gating pulse. The HHG pulse train is focused using the toroidal mirror. The delayed NIR pulse will be focused by a spherical mirror ROC = 800 mm. These two arms are finally recombined through a perforated mirror and sent to our electrodes.

To detect these electronic currents, we use a copper plate as our electrode. We also place the gas nozzle almost 3 mm away, right above the copper plate and below the TOF, at the attosecond streaking focus. Same as the case of LPPS in solids we collect the currents from the electrode and amplify this current with a transimpedance amplifier and we send this amplified current to a Lock-in amplifier for digitization. (figure 5.1)

In LiF measurements, we had to phase-match our HHG radiation to have maximal photon counts around 13 eV. In order to have a better signal to noise ratio, we need to phase-match for radiations above the ionization energy of Ne ( $I_p = 21.56$  eV). We found out that best phase-matching for these photon energies is achieved by setting the backing pressures of argon gas in the HHG target at 40 mbars.

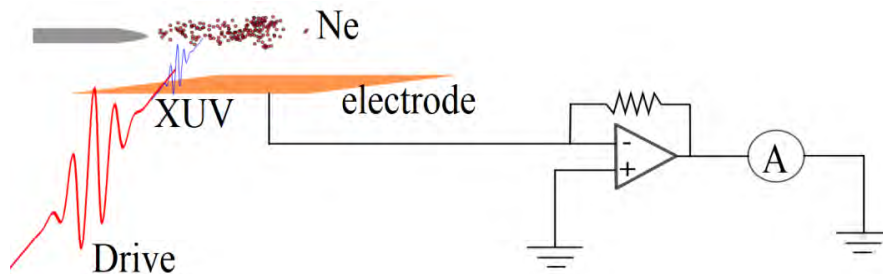


Figure 5.1. Data acquisition for LPPS in gases. The current from the collected electrons is amplified by a transimpedance amplifier and detected by a lock-in amplifier.

<sup>26</sup> Helium has higher ionization energy than neon; but, we choose neon because when ionized it will mainly go to an s-wave. Therefore, the final state is isotropic.

After achieving the suitable condition for better electron ionization, we observe under the same gating pulse amplitude that, with respect to the case of LiF, the signal amplitude is 158 times stronger. We need to identify the reason for this huge increase in amplitude (figure 5.2).

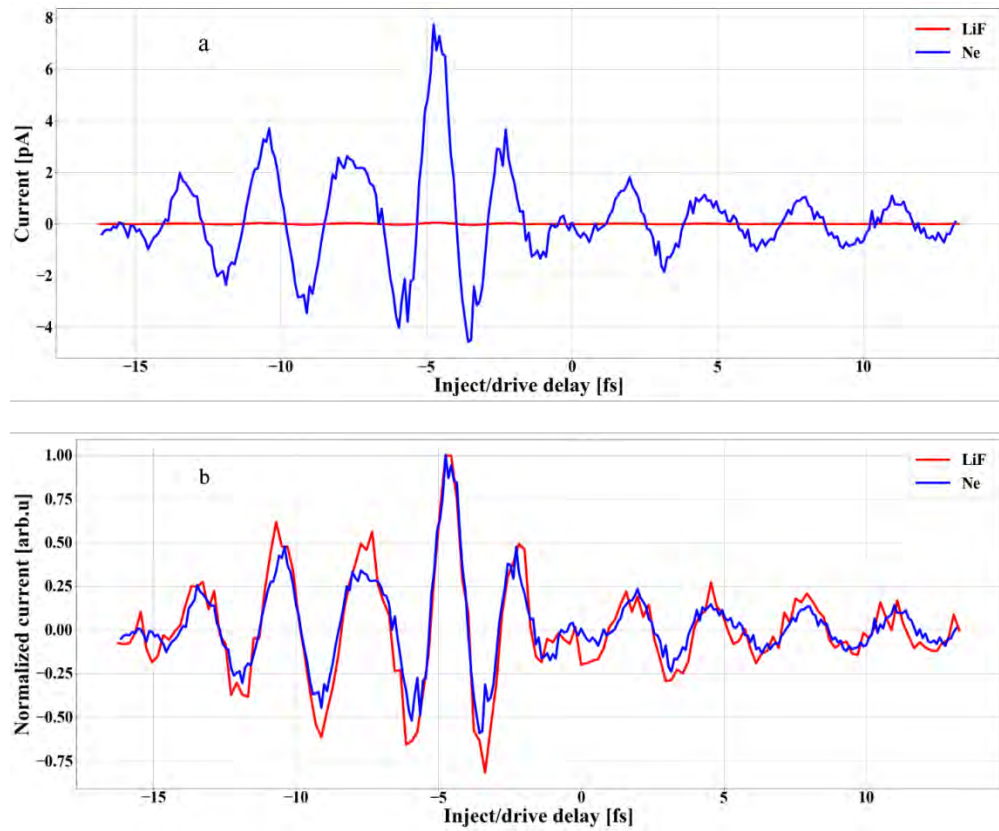


Figure 5.2. The comparison of the signal amplitude of the LPPS in Ne (blue curve) and in LiF (red curve) at drive power 20 mW. a) detected currents. b) normalized currents (the normalized currents are shown to prove that both methods measure the same signal)

## 5.2: Source of signal

In the case of the LiF, the source of the current signal is from the macroscopic dipole that is formed in the medium due to the charge separation caused by our NIR driving field. The asymptotic dipole then induces some charges on the external electrodes. The very famous example of charges in between two grounded infinite metallic plates serves as a good example of how these currents are formed. So, the signal we measure is directly proportional to this dipole.

### 5.2.1: comparison of dipole magnitude in LiF and Ne

As we know, dipole magnitude is the product of charge and charge separation. First, let us take a look at the charge that we create. In the lattice structure of LiF, the atomic density is very high. The lattice constant of LiF is  $a_{\text{LiF}} = 403.51 \text{ pm}$ . Since we are exciting one electron per molecule of LiF, per volume  $V = a^3 = 0.066 \text{ nm}^3$  we have 4 electrons. So, the electron density is  $\rho_e = 6.08 \times 10^{28} \text{ m}^{-3}$ . In section 4.1 we described a method to calculate the charge separation. In chapter 4.1 we showed that the maximum charge separation for one dipole would be  $d_{\text{LiF}} = 1 \text{ nm}$ . So, the dipole moment created by one single charge would be:

$$p = e \times d = 1.6 \times 10^{-28} \text{ Cm}$$

In the case of Ne, we need to first calculate the gas pressure a couple of millimeters away from the nozzle. Since our gas nozzle releases the Ne with the backing pressure of almost 1.5 bars to vacuum, the jet of Ne atoms is supersonic.

We use a simple model of a Mach cone to describe the expansion of this jet [114], to calculate the angle of expansion:

$$\theta = 2 \times \text{asin}\left(\frac{v}{u}\right) \quad 5.4$$

where  $v = 343 \text{ m/s}$  is speed of sound and  $u$  is speed of the jet.

To calculate the speed of the jet bursting out of the nozzle, we use Bernoulli's equation:

$$P = \frac{1}{2} \rho u^2 \quad 5.5$$

With  $P$  being the backing pressure of the nozzle and  $\rho$  the density of the gas. Neon has a density of  $0.9 \text{ kg/m}^3$  in STP<sup>27</sup> (i.e.  $\rho_0 = 0.45 \text{ g/L}$  at 0.5 bar). So  $u = 471.4 \text{ m/s}$ . Putting this value in Eq. 5.4, we get:

$$\theta = 2 \times \text{asin}(0.71)$$

We estimate that the region of interaction is about 2 mm away from the nozzle. Therefore, the radius of the Mach disk 2 mm away from the nozzle will be:

$$R = 2 \times \sin(u/v) = 2.07 \text{ mm}$$

---

<sup>27</sup> STP stands for standard temperature and pressure. According to IUPAC these standards are 273.15 K for temperature and 1 bar for pressure [115]. Therefore, if neon has  $0.9 \text{ kg/m}^3$  density at STP, then it has  $\rho_0 = 0.45 \text{ g/L}$  at 0.5 bar.

We estimate that the nozzle hole has a radius of  $r = 25 \mu\text{m}$ . Then the density of the neon jet 2mm away from our nozzle would be  $\rho = \rho_0 \left(\frac{r}{R}\right)^2 = 6.3 \times 10^{-5} \text{kg/m}^3$ . Since, the atomic mass of neon is  $m_{\text{ne}} = 3.35 \times 10^{-26} \text{kg}$ , the atom density will be  $n = 1.86 \times 10^{21} \text{m}^{-3}$ .

The particle density of Ne, in our case is about  $3.3 \times 10^9$  times smaller than the LiF. The charge separation in Ne is much larger because long after the electric field is gone the electron can go on without any disruption. So, the charge separation, in this case should be calculated up until the detection time of our external circuit. This time is approximately on the order of nanoseconds. The highest energy of ionized electrons in this case is about  $E_{K0} \cong 40 \text{ eV}$ . For some, the same driving field amplitude (i.e.  $0.2 \text{ V/\AA}$ ), the final velocity of the electron is  $V_f = \sqrt{2E_{K0}/m_e} + \frac{eA(\tau)}{m_e}$ . In case of our laser amplitude of the vector potential is  $A_0 = 8.27 \times 10^{-7} \text{kg} \cdot \frac{\text{m}}{\text{sC}}$ , thus the final velocity is  $V_f = 3.89 \times 10^6 \text{ m/s}$ . In one nanosecond this electron can travel  $d_{\text{ne}} = 3.89 \times 10^{-3} \text{ m}$ . The dipole moment is:

$$p_{\text{ne}} = e \times d_{\text{ne}} = 6.22 \times 10^{-22}$$

As you can see the dipole moment in neon is  $0.85 \times 10^8$  times larger than in LiF and the density is  $3.3 \times 10^9$  times smaller. As a result, we should have an even smaller signal if the induced current on the electrodes are from the screening of electric field of macroscopic the induced dipole in neon. So, the source of this huge signal should be the transport of these electrons.

The picture that we have about the transport effect is the following: XUV light ionizes the Ne atoms and generates bunches of electrons with initial kinetic energy of  $0 \text{ eV} \leq E_{K0} \leq 40 \text{ eV}$ . These electrons with the initial kinetic energy above  $5 \text{ eV}$  easily reach the electrodes in less than a nanosecond. Therefore, we will always have an offset signal in our detectors. At lower energies, the increase or decrease in kinetic energy of these electrons by the driving field can be enough to allow them to reach the electrodes or not.

This picture is still incomplete because this means that the delay-dependent signal should only be proportional to the spectral density of electrons. But as we can see that, the signal goes we with vector potential (for a detailed discussion, refer to the benchmarking section). So, what is the reason behind this dependence?

### 5.2.2: Population transfer

The XUV ionization of the Ne atoms creates a spherical electronic cloud (figure 5.3.a). In case of no extra accelerating field, electrons that are in the upper half-sphere will always reach the upper electrodes and vice versa. The addition of an accelerating field, in this case, the NIR, will add extra momentum to all electrons (which is proportional to the vector potential  $A(\tau)$  of the field at the moment of electron ionization). Depending on how slow the electrons are, the additional momentum from the NIR can change the final direction of the electrons. Therefore, if  $|eA(\tau)| > |P_{\text{ini}}|$ , then electrons with initial momentum less than  $|P_{\text{ini}}|$  will change direction and are added to the population of the other half-sphere (figure 5.3.b).

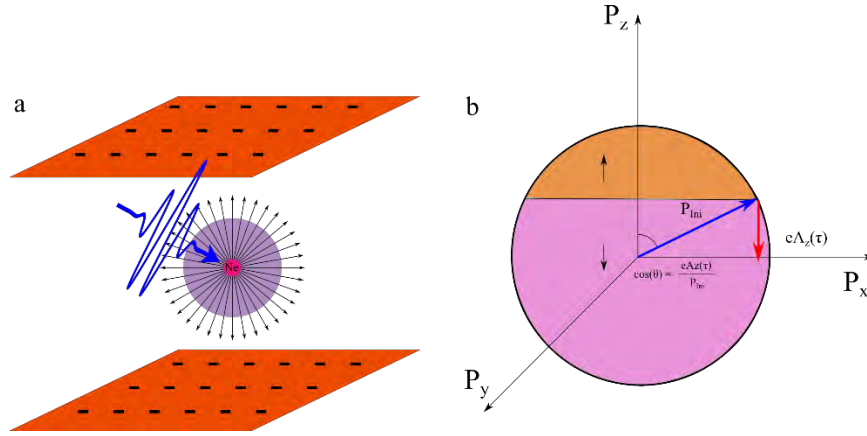


Figure 5.3. Population transfer mechanism. a) Creation of spherical S-waves by ionization of the Ne atoms with XUV pulse. In the absence of the driving field population ionized electrons of the upper sphere ( $\theta < \pi/2$ ) is equal to population ionized electrons of the lower sphere ( $\theta > \pi/2$ ). b) Electron density in momentum space. The blue arrow shows the initial momentum of electrons. The red arrow is the added momentum from the driving field. The pink shaded area is electrons that will move downward and the orange shaded area is electrons that will move upward.

The total number of electrons that are being release in  $4\pi$  angle is:

$$N = \int_0^{P_{\max}} n(\mathbf{P}) d^3\mathbf{P} \quad 5.6$$

where  $n(\mathbf{P})$  is the electronic population density that has absolute momentum between  $\mathbf{P}$  and  $\mathbf{P} + d\mathbf{P}$ . If the accelerating field is polarized in  $z$  direction, then at a certain delay  $\tau$  the shift in momentum from the NIR is  $eA_z(\tau)$ . Consequently, the total amount of electrons that will change their direction will be:

$$\Delta N = \int_0^{P_{\max}} \int_{\frac{eA_z(\tau)}{P}}^0 \int_0^{2\pi} n(\mathbf{P}) P^2 dP d\cos(\theta_P) d\phi_P \quad 5.7$$

If we assume that  $n(\mathbf{P}) = \text{const}$ , then we shall have:

$$\Delta N = \frac{3}{2} N \frac{eA_z(\tau)}{P_{\max}} \quad 5.8$$

Calculation of this integral for the initial electron energies between 0 to 60 eV has been performed for 3 different driving field amplitude 0.01, 0.5 and 1.0 V/Å f. The calculated delay-dependent integrals are presented in the figure 5.4. The result shows that at 0.01 V/Å the population transfer acts like a sign function (figure 5.4.a). At very low amplitudes, the driving field cannot change the final direction of electrons, except extremely slow electrons and for electrons that are born with 0 kinetic energy any field amplitude can either completely send them up or down depending on the sign of  $A(\tau)$ . Therefore, most of the signal comes from the electrons which were born at 0 eV kinetic energy. Increasing the driving field, we can manipulate the faster electrons, and that is the reason why at 0.5 V/Å the signal resembles the vector potential more. So, this means if we increase the driving amplitude then we get closer and closer to a signal that behaves like vector potential.

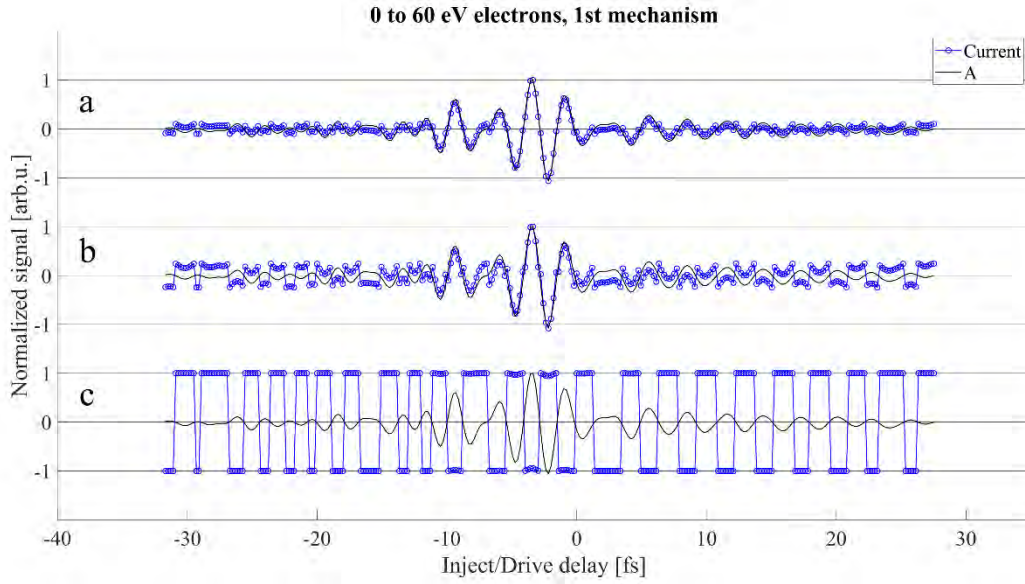


Figure 5.4. Comparison of the signal from population transfer mechanism (blue circled curve) and the vector potential of the driving field (black curve) at 3 different electric field amplitudes. a)  $1.0 \text{ V/\AA}$ , b)  $0.5 \text{ V/\AA}$ , c)  $0.01 \text{ V/\AA}$

One might ask why this behavior is not seen in the integral of Eq. 5.8. The answer comes from the fact in solving that integral we are neglecting the fact that  $\cos(\theta_p) = \frac{eA_z(\tau)}{P}$ , where  $P = 0$  is undefined. Extra care should be taken when in the second integral in Eq. 5.8 the boundary has a singularity in it.

The calculated results show that the mechanism of the population transfer works perfectly when we neglect the effect of ultra-slow electrons. The addition of these electrons results in having deviation from the vector potential like currents (especially, at weak driving fields). Therefore, we conclude that this mechanism is not the only reason that LPPS in gases behaves like vector potential.

### 5.2.3: Metallic barrier transmission probability

Consider a one-dimensional step potential like this:

$$V(x) = \begin{cases} 0 & x < a \\ -w & x \geq a \end{cases} \quad 5.9$$

where  $x = a$  is the barrier between metallic surface and vacuum, and  $w$  is the work function of this metal. When an electron wave packet that propagates from negative  $x$  values to positive values, reaches this step, a part of its wave function will be transmitted through the step and the other part will be reflected.

The transmission probability of the wave function is:

$$T = \frac{\psi_t^* \nabla \psi_t - \psi_t \nabla \psi_t^*}{\psi_i^* \nabla \psi_i - \psi_i \nabla \psi_i^*} \quad 5.10$$

Where the  $\psi_i, \psi_t, \psi_i^*$  and  $\psi_t^*$  are the incident, the transmitted wave function and their complex conjugates respectively [116].

By solving the Schrodinger equation for this system we find that T is:

$$T = \frac{4k_1 \times k_2}{(k_1 + k_2)^2} \quad 5.11$$

where  $k_1 = \frac{\sqrt{2m_e E}}{\hbar}$  and  $k_2 = \frac{\sqrt{2m_e(E+w)}}{\hbar}$  and  $E$  is the kinetic energy of the incident electron on to the potential step.

The incident energy is:

$$E = E_{k_0} + \frac{(eA)^2}{2m_e} + \frac{\sqrt{2m_e E_{k_0}} eA}{m_e} \quad 5.12$$

For the electric field with amplitude of  $F = 0.2 \text{ V/\AA}$  and  $E_{k_0} < 40 \text{ eV}$ , in the Eq.5.12 the second term is about 0.06 eV and less than 1.61 eV for the third term. So, we can drop out the second term:

$$E \cong E_{k_0} + \frac{\sqrt{2m_e E_{k_0}} eA}{m_e} \quad 5.13$$

Inserting this in  $k_1 = \frac{\sqrt{2m_e E}}{\hbar}$  we have:

$$k_1 \cong \frac{1}{\hbar} \times \sqrt{2m_e \left( E_{k_0} + \frac{\sqrt{2m_e E_{k_0}} eA}{m_e} \right)} \quad 5.14$$

and for  $k_2 = \frac{\sqrt{2m_e(E+w)}}{\hbar}$  we have:

$$k_2 \cong \frac{1}{\hbar} \times \sqrt{2m_e \left( E_{k_0} + \frac{\sqrt{2m_e E_{k_0}} eA}{m_e} + w \right)} \quad 5.15$$

In the case of very low energy electrons, we can neglect the first term and the third term and we will have  $k_1 \cong \frac{eA}{\hbar}$  and  $k_2 \cong \frac{1}{\hbar} \times \sqrt{2m_e \left( \frac{(eA)^2}{2m_e} + w \right)}$ . For normal metals, the work function is about  $w = 5 \text{ eV}$ , so we can throw away the quadratic term,  $\frac{(eA)^2}{2m_e}$ , in  $k_2$ :

$$k_2 \cong \frac{1}{\hbar} \times \sqrt{2m_e w} \quad 5.16$$

Then for the case of low energy electrons we have:

$$T = \frac{eA \times \sqrt{2m_e w}}{(eA + \sqrt{2m_e w})^2} \quad 5.17$$

Figure 5.5 shows the Eq. 5.17 for the same driving field amplitudes as in the case of the previous mechanism (0.01, 0.5 and 1.0 V/\AA). These results show that for very low driving field amplitude (0.1 V/\AA) the model perfectly fits the vector potential behavior, but as the driving field becomes stronger and stronger the deviations from the vector potential-like behavior gets more and more. So, this mechanism works perfectly at small driving field amplitude and does not fit the vector potential at high driving fields.

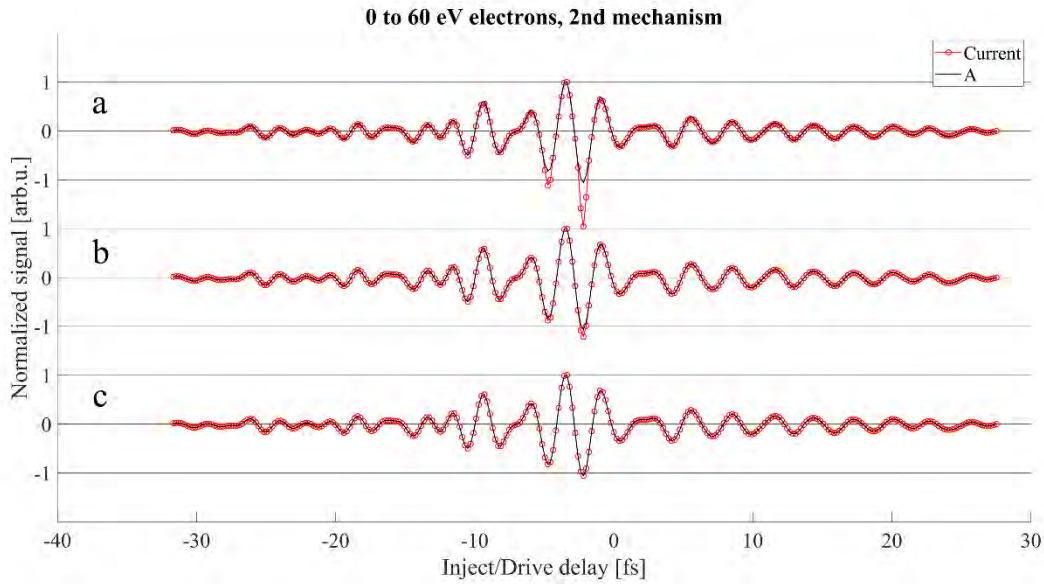


Figure 5.5. Comparison of the signal from the metallic barrier transmission probability mechanism (red circled curve) and the vector potential of the driving field (black curve) at 3 different electric field amplitudes. a)  $10 \text{ V/nm}$ , b)  $5 \text{ V/nm}$ , c)  $0.1 \text{ V/nm}$

Figure 5.6 shows the situation where both mechanisms are considered. These results show that, while the first mechanism fails at low driving field amplitudes, the second mechanism compensates for this failure. On the other hand, failure of the second mechanism at high driving field amplitudes is compensated by the first mechanism. Therefore, currents that were calculated by consideration of both mechanisms fit the vector potential-like behavior.

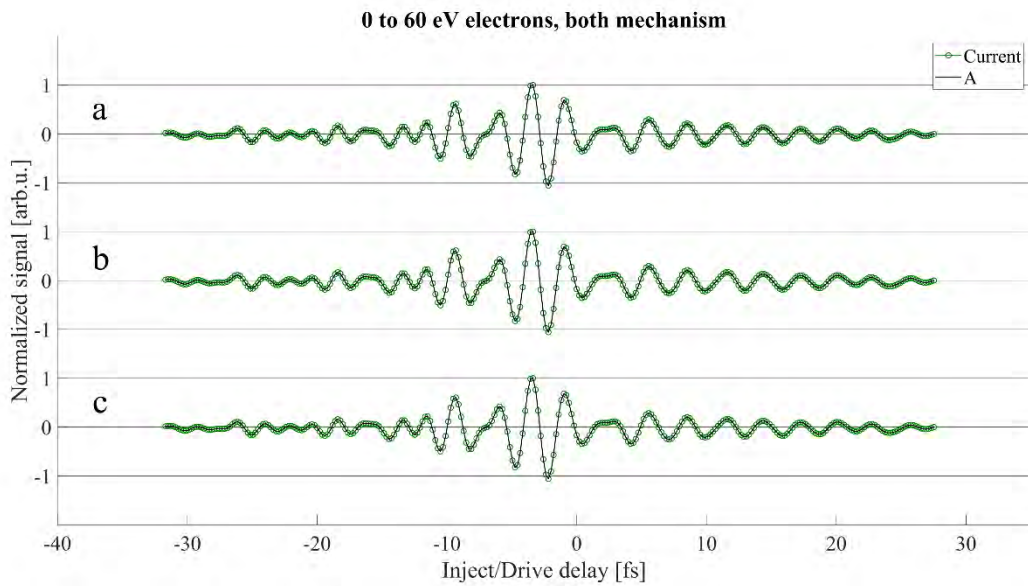


Figure 5.6. Comparison of the signal from both mechanisms (green circled curve) and the vector potential of the driving field (black curve) at 3 different electric field amplitudes. a)  $10 \text{ V/nm}$ , b)  $5 \text{ V/nm}$ , c)  $0.1 \text{ V/nm}$ .

### 5.3. CEP dependence of the signal

In the previous section, we proved that the main contribution to signal comes from the low energy harmonics near the ionization energy of Ne. In this case, the photons near the ionization energy of Ne (21.56 eV) are responsible for the generation of the signal.

From the experimental results, we can see that when the CEP of the NIR pulse that generates this VUV radiation, changes, the SNR of the detected current drops at some specific CEP (figure 5.7 blue curve). Since we can only measure the relative value of this CEP, we call the CEP of the lowest SNR,  $\pi/2$ . We can also see that changing this CEP by  $\pi/2$  maximizes the SNR (figure 5.7 Red curve).

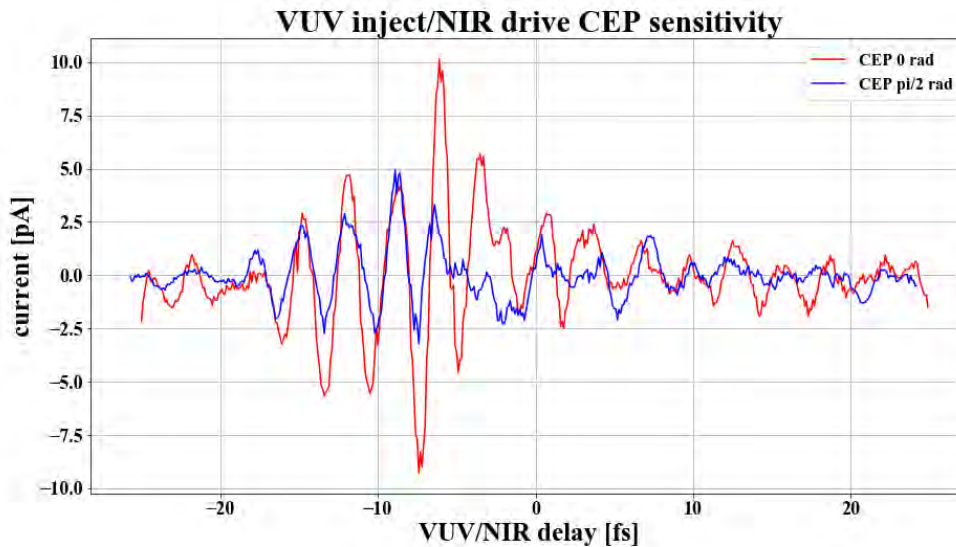


Figure 5.7. Comparison of the LPPS signal at 2 different injection CEP of 0 rad (red curve) and  $\pi/2$  rad (blue curve)

Since the measured current is the convolution of the vector potential and the injection probability envelope, knowing the injection envelope provide explanation for these results.

We simulate the HHG spectra with HHGMAX code [117, 118]. For the NIR field that generates HHG, we use an electric field that we measured with attosecond streaking and we scale the amplitude to get the field strength required for HHG cutoff frequency around 80 eV.

The calculated time-domain electric field of the high harmonic radiation for CEP 0 and  $\pi/2$ , for photons with energy spectra between 21 to 26 eV, are shown in figure 5.9. The red curve shows that at CEP =  $\pi/2$  rad, we have two instances of injection that are separated by one half-cycle of the NIR field. This means that each instance of injection of the VUV pulse will experience electric field of the driving pulse with opposite signs. In other words, the integrand in the integral of Eq. 4.5, has different signs in the neighboring half cycles of the driving pulse. Thus, integrating over one full cycle suppresses the value of the integral in Eq. 4.5. As a result, the measured current will be smeared. However, in the case of the CEP = 0 (blue curve in figure 5.8), there is only one instance of injection. Therefore, the measured current will be stronger. Hence the SNR is higher.

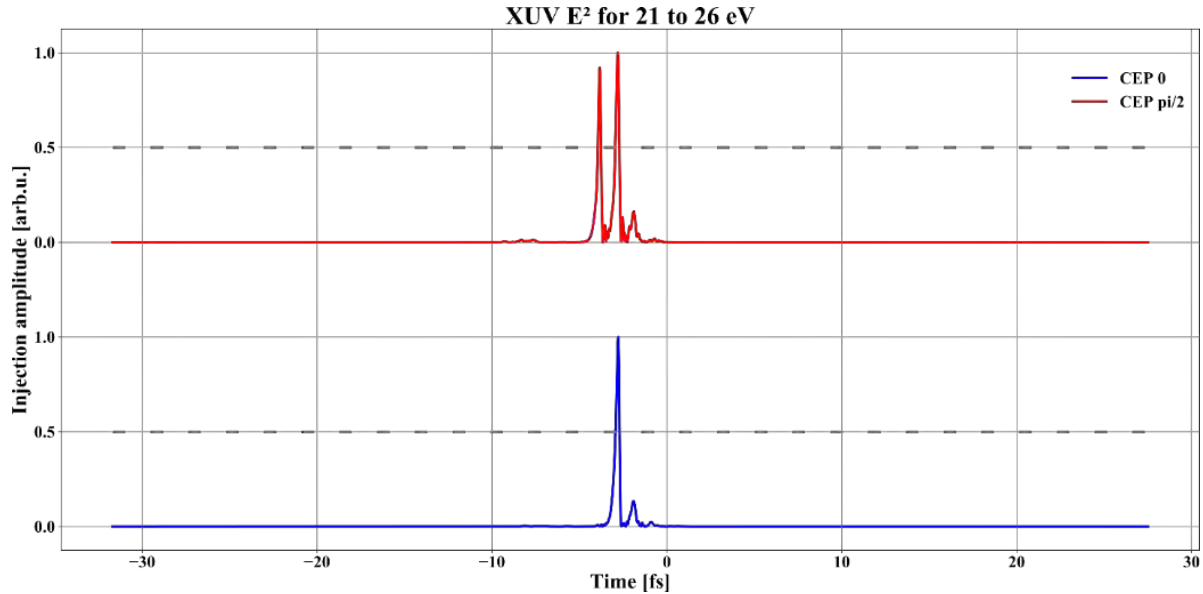


Figure 5.8. Envelope of the injecting pulse at 2 different CEPs: 0 rad (red curve) and  $\pi/2$  rad (blue curve)

## 5.4. Benchmarking

We have shown theoretically that our measured current resembles the vector potential of the driving field with a constant of proportionality. Similar to cases of the LiF and SiO<sub>2</sub>, we performed in-situ attosecond streaking measurements to sample the driving NIR field. The Ne gas nozzle is placed below the TOF and above the copper electrode. For the case of the attosecond streaking measurement, an aluminum scandium filter is used to create a single burst of XUV light. Later on, for the photo-conductive, this filter is removed and the current is measured.

Figure 5.9 shows the final spectrogram and averaged final kinetic energy of the electrons in this measurement. The normalized current beautifully fits the reconstructed vector potential (figure 5.10). The spectral response of both measurements (figure 5.11 blue and red curve left axis) and the respective spectral group delay (figure 5.11 green and black curve, right axis) of both measured waveforms fit perfectly to each other. These results are strong evidence that photo-conductive in gases can be used as a perfect tool to measure the electric field of the NIR field from 1100 nm down to 500 nm (the cutoff of our laser). This result shows LPPS in neon exactly acts like attosecond streaking in the sense that all the temporal and spectral information of the measured field in both cases are equivalent, up to the cutoff of our laser. Therefore, if we calibrate the LPPS measurements with respect to attosecond streaking once we can replace measurements that require attosecond streaking with LPPS in neon.

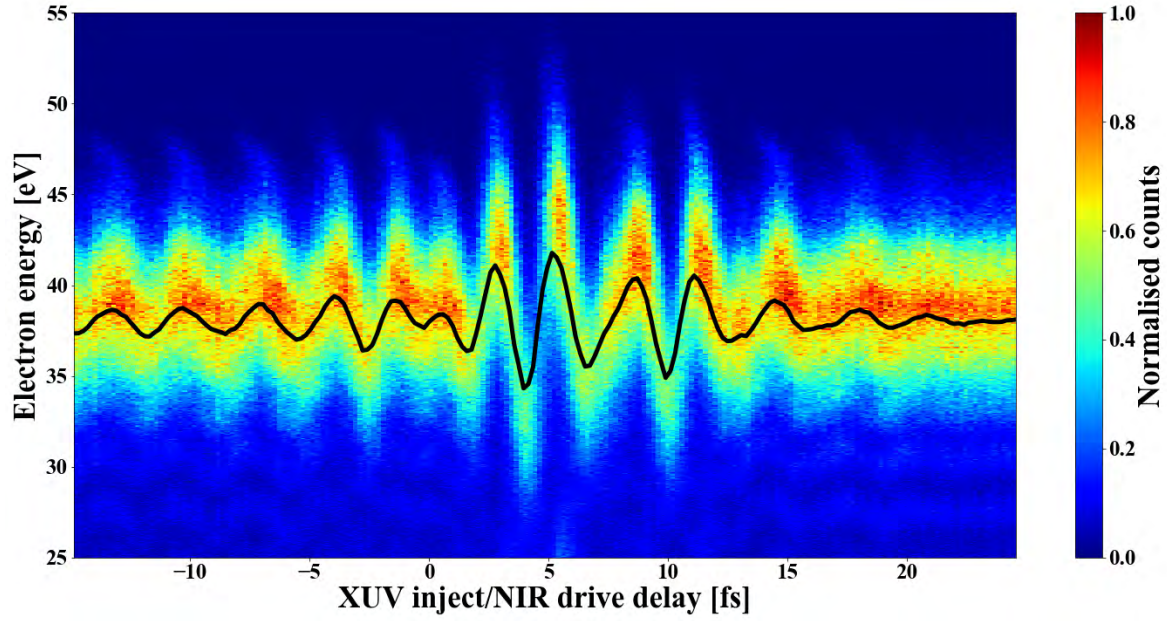


Figure 5.9. Streaking spectrogram for the bench marking. the black curve depicts the average energy of the electronic wave packet.

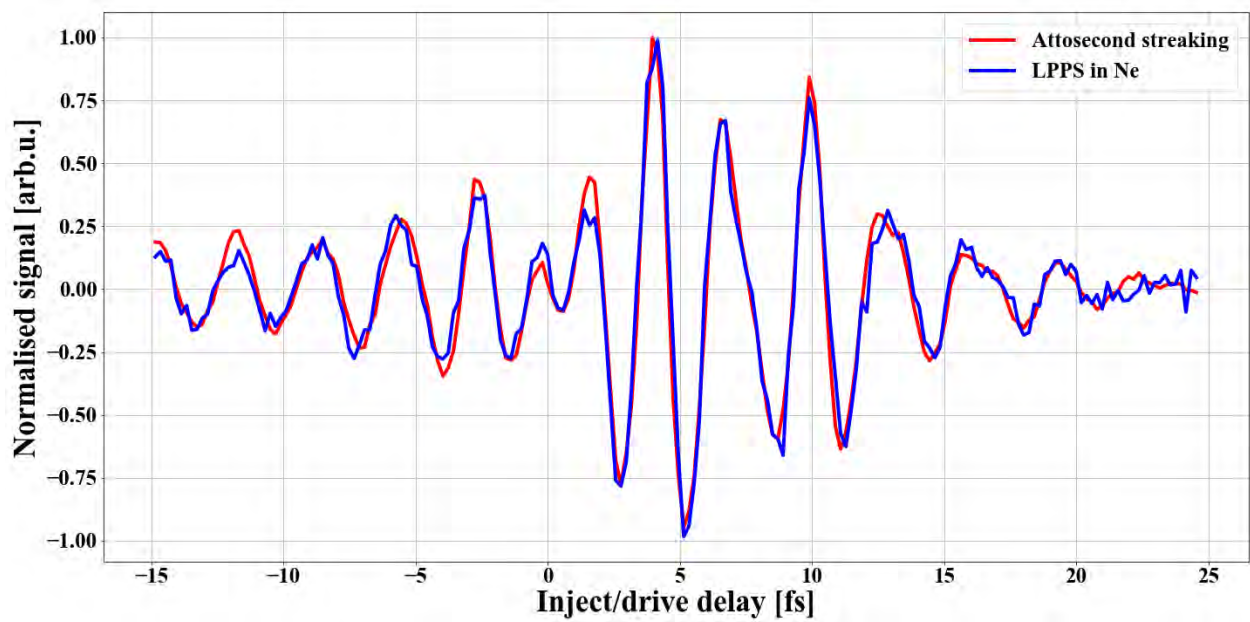


Figure 5.10. Comparison of the retrieved vector potential from the streaking (red curve) with the detected current from LPPS in Ne.

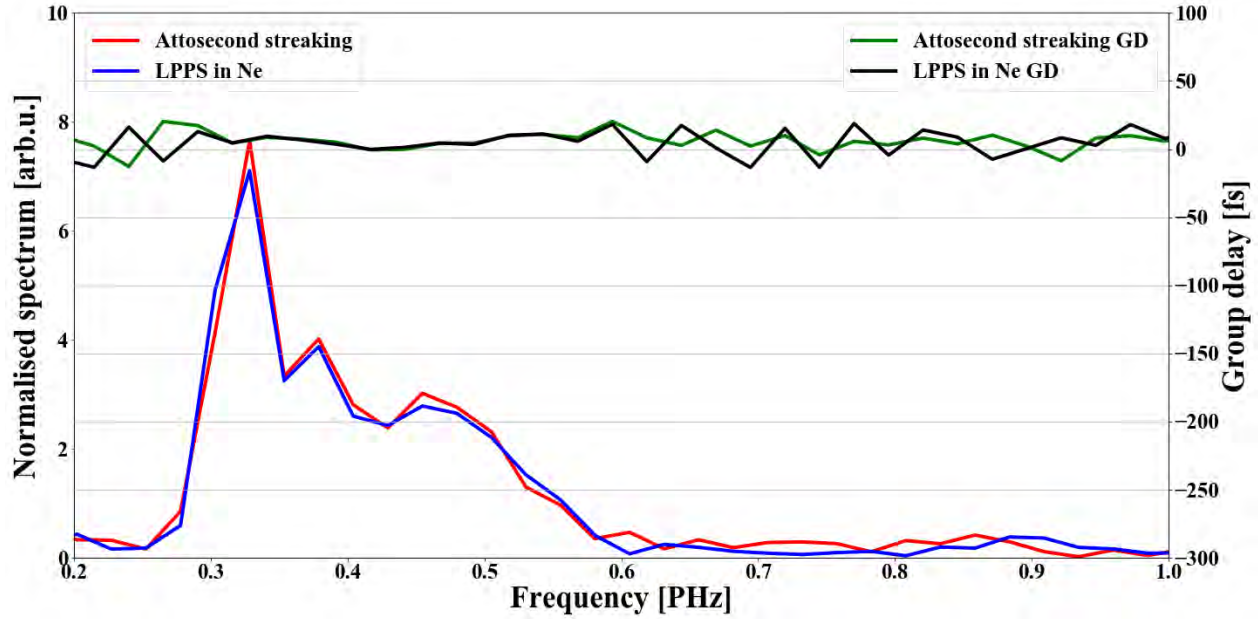


Figure 5.11. Comparison of the spectrum of the detected signals (left y-axis) and their respective group delays (right y-axis). The Red and the blue curve are the spectrum of the streaking and the LPPS in Ne respectively. The green and the black curve are the group delays of the streaking and the LPPS in Ne respectively.

## 5.5. Dynamic range

Furthermore, we set out to find the dynamic range of measurement. Again, similar to the case of LiF/SiO<sub>2</sub>, we control the driving field amplitude using an iris in the delay chamber. Since only 10% of the NIR pulse energy is sent to the Delay arm and the spot radius of this beam at the point of measurement is roughly 110  $\mu\text{m}$ , we can only have field amplitudes up to 0.73 V/Å (note that, this value is an estimate of field envelope amplitude). The lowest field envelope amplitude we can reach (almost totally closed iris) is about 0.1 V/Å.

For the reference scan, attosecond streaking of a NIR transient with field amplitude of  $F_0 = 0.199 \text{ V/Å}$  is performed. The extracted vector potential is compared with LPPS current at different field amplitudes. The results of comparison between reference streaking scan and LPPS currents at field amplitudes of 0.142, 0.244, 0.345, 0.404, 0.456 and 0.502 V/Å is presented in figure 5.12.

The perfect resemblance of these scans to the reference shows that at this vast range LPPS in Ne is linear. We define the dynamic range as the ratio of the amplitude of the largest oscillation at last scan ( $F_0 = 0.502 \text{ V/Å}$ ) to the amplitude of the smallest field oscillation in the first scan ( $F_0 = 0.142 \text{ V/Å}$ ). The latter field amplitude is about 0.003 V/Å (figure 5.13). As a result, we report up to 44 dB of dynamic range in field intensity. We estimate we can reliably measure the electric field of NIR pulses, up to the point of multiphoton injection NIR pulse in Ne.

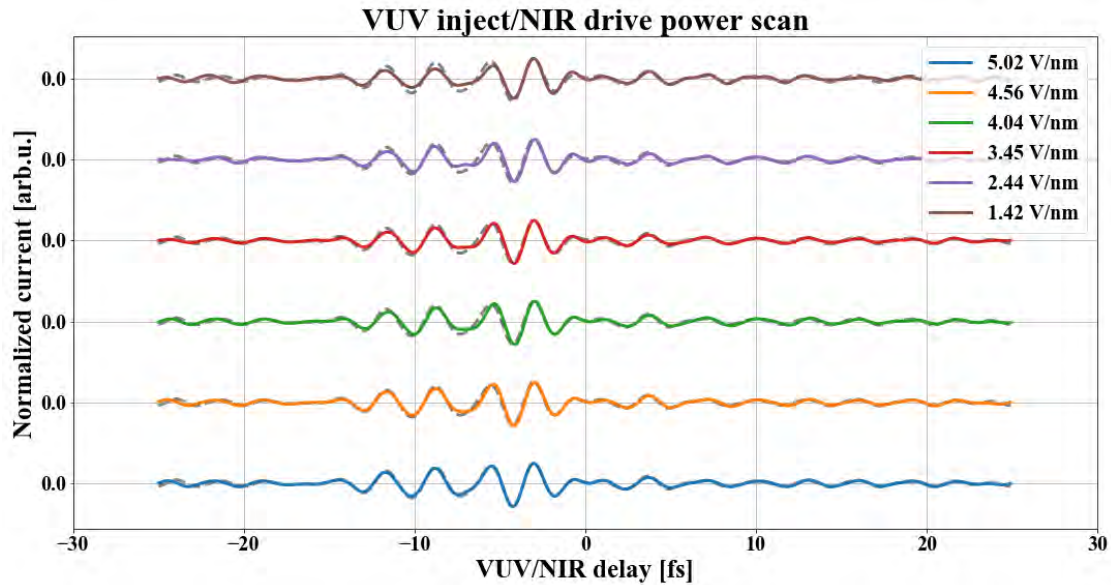


Figure 5.12. Comparison of the LPPS signal in gas for 6 different field amplitudes (solid curves) with the reference signal (dashed grey curve).

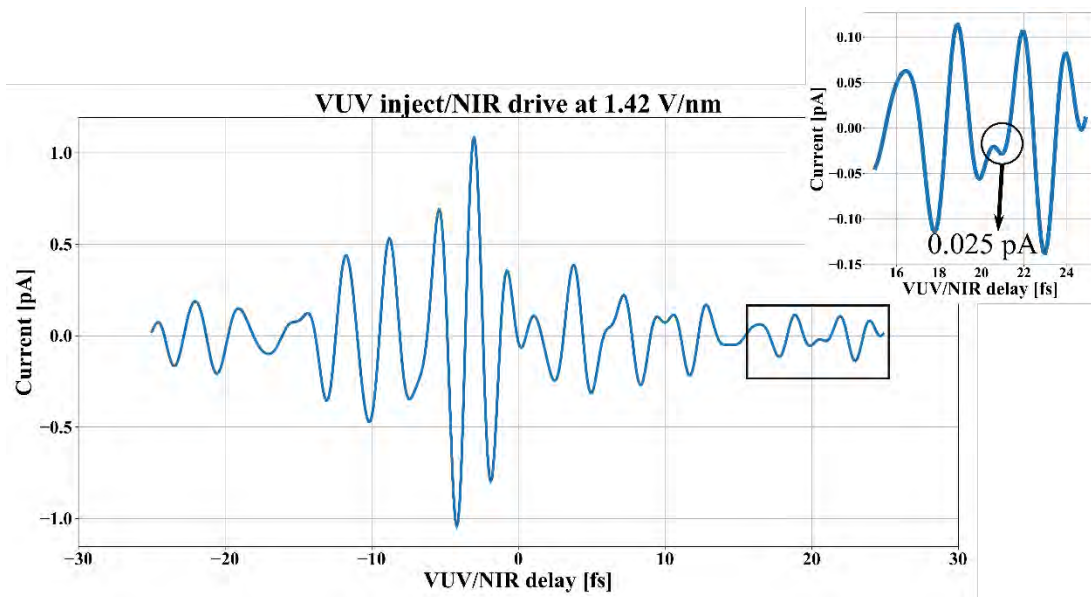


Figure 5.13. The lowest detectable current (i.e. vector potential) oscillation by LPPS in Ne. The largest half-cycle has 1.1 pA amplitude, which correspond to amplitude of electric field equal to  $F_0 = 1.42 \text{ V/nm}$ , while the lowest oscillation has the absolute value of the 0.025 pA (inset plot shows the zoomed view of the vicinity of that oscillation), which has  $F = 0.03 \text{ V/nm}$ . The largest detectable oscillations were with electric field amplitude of  $F_0 = 5.02 \text{ V/nm}$  (Brown curve in Fig. 5.13)

## 5.6: Extension of bandwidth of detection in LPPS by Ne

The spectral bandwidth of detection is an important factor in establishing a new method for sampling the electric field of optical pulses. The most desired time-resolved sampling method should be able to detect

from the MIR to the VUV spectral region. Up to now, we have established that the LPPS in Ne can cover the whole bandwidth of the Ti:Sa source (i.e. 1000 nm to 500 nm). To investigate what the highest detectable frequency is for LPPS, we need to generate higher frequencies employing nonlinear effects such as SGH.

### 5.6.1: UV light generation

Since our NIR source has the bandwidth down to 500 nm, to test the extent of bandwidth of LPPS we need to broaden our NIR source further toward the UV. Any broadening process is a nonlinear, since only 10% of our 800  $\mu$ J few-cycle pulse is sent to the delay arm, in order to achieve strong nonlinearities in broadening medium, we need to create an intermediate focus, in the Delay arm. Therefore, we exchange the PM mirrors in the Delay chamber (see figure 3.2) with two off-axis 90-degree parabolic mirrors with reflective focal length  $RFL = 2$  inches. For the nonlinear medium, we use 0.5 mm thick beta barium borate (BBO) with  $\theta = 29^\circ$  and  $\phi = 90^\circ$  (BBO-1204-10H Eksma optics, UAB). This crystal is phase-matched to generate the second harmonic down to 266 nm.

The original spectral range of our laser is between 1000 nm to 500 nm. In this case, normal silver protected parabolic mirrors (MPD129-P01, Thorlabs) can be used. However, silver mirrors do not have ideal reflection below 300 nm; therefore, the collimating parabola, the spherical focusing mirror, and the perforated mirror should be replaced with UV enhanced Aluminum mirrors, when we aim to broaden the bandwidth of the optical transient. For the collimating parabola, we use the commercial Off-Axis Parabolic Mirrors, UV-Enhanced Aluminum RFL 2-inches parabola (MPD149-F01, Thorlabs). Also, the spherical mirror has the same kind of coating, 1500 mm ROC, 2-in diameter spherical mirror (CM508-750-F01, Thorlabs). For the case of the perforated mirror, we use a TFAN coating (OFBP-50C08-10-TH1.5-45, OPTOSIGMA EUROPE SAS).

### 5.6.2: Signal modulation

Previously we have mentioned that for the detection of LPPS currents, we use CEP flipping of the pulses, and we lock into the rep-rate of this flipping. While this procedure works perfectly for the fundamental signal, it fails to work for the second harmonic signal, since flipping the CEP of the fundamental pulse from 0 to  $\pi$  results in the flipping of the CEP of the second harmonic from 0 to  $2\pi$ . As a result, when the lock-in amplifier subtracts the neighboring pulses at 3 kHz it will result in zero signal.

Although it seems reasonable to assume that we can use a CEP change of 0 to  $\pi/2$  (since it will change the second harmonics CEP from 0 to  $\pi$ ), this scheme doesn't work. We change the CEP using the DAZZLER in the CPA (please refer to section 3.1 about the laser source). This will also change the CEP of the NIR pulse that generates the HHG. This change in the CEP, changes the time-dependent envelope of the injection pulse from one shot to another. Consequently, the detected signal in lock-in amplifier will be noisy.

To solve this problem, we use a chopper in the Delay arm. The chopper is locked at 1.5 KHz. As a result, instead of having a 3 kHz signal from driving field we will have a 1.5 kHz signal. Further details of chopper detection scheme are discussed in appendix A.

### 5.6.3: Measurement geometry

Since we are using type 1 phase-matching for the generation of the second harmonic, we need to alter the polarization of the fundamental from S to P, remember that the electron transport to the electrodes is the source of the signal so having the S polarization of the fundamental means P polarization for the second harmonics which will not be detected by the electrodes.

We rotate the polarization of the fundamental by placing a periscope in the Delay arm of the delay chamber right after the iris (see figure 3.2). The change in polarization is set in a way that still 10 percent of the intensity of the fundamental remains in the direction of S polarization, we are going to use this remaining component of polarization for analysis of the detected second harmonics. Therefore, when we measure the signal after the BBO we expect to have the spectrum from the fundamental and the second harmonics (see figure 5.14 for clarification).

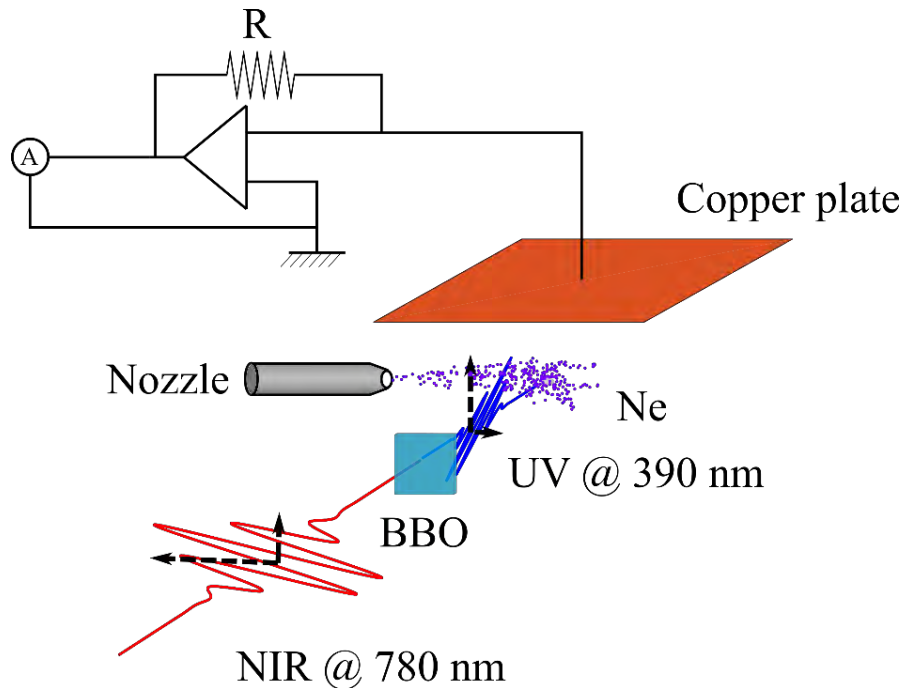


Figure 5.14. Schematic optical geometry of the LPPS setup for detection of the second harmonics. the polarization of the NIR pulse that is chosen to be not purely P (the dashed horizontal arrow). As a result, we will have a bit of the S polarization of NIR (the solid vertical arrow) that we can detect. this residual NIR is used to characterize the generated second harmonics (see section 5.6.6.). as a result of this small rotation of polarization, the generated second harmonics will have S (the dashed vertical line) and a P (solid horizontal line) polarization.

#### 5.6.4: Streaking of UV pulse

First, we set to detect this pulse with attosecond streaking. The retrieved vector potential and its Fourier transform (i.e. spectra of vector potential) are depicted in figure 5.15.a and b.

Looking at the spectral amplitude, we see that above 0.5 PHz (600 nm) there are not enough strong oscillations. If we zoom in the spectral region between 0.5 to 1 PHz, where the second harmonics signal should appear for frequencies between 0.25 to 0.5 PHz, we see a small spectral amplitude (see the inset in figure 5.15.b). If you look at the spectral components above 1 PHz you can still see some peaks and we need to understand how to distinguish whether these peaks are noise or signal.

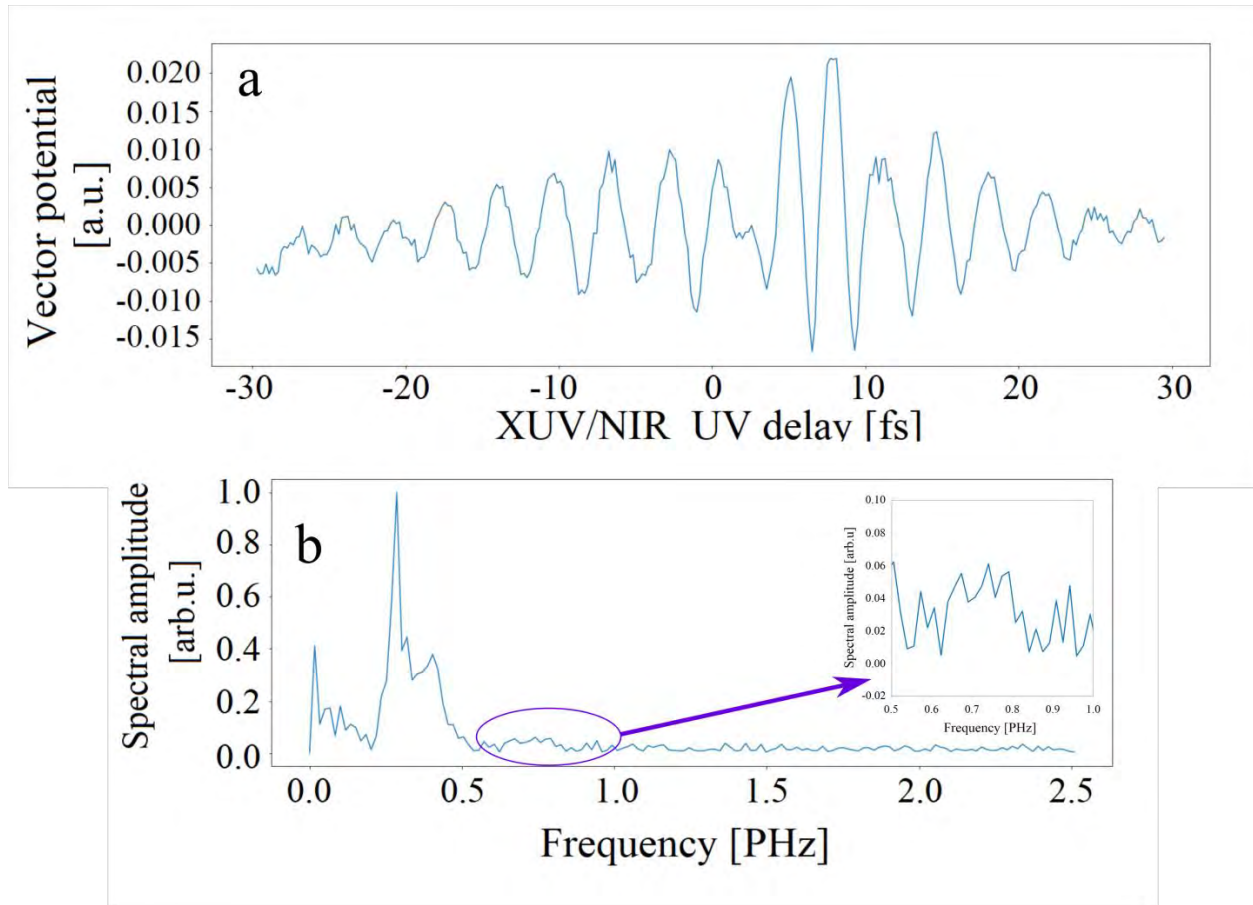


Figure 5.15. Results of Attosecond streaking for detection of the second harmonics of the NIR pulse from Ti:Sa source. a) The retrieved vector potential. b) Fourier transform of the vector potential. The inset in b is the plot of the spectral region that we expect the second harmonics should exist.

### 5.6.5 Differentiating between noise and signal at high frequencies

Both streaking and LPPS measure the vector potential of the electric field. In the spectral domain the relation between the electric field and vector potential is:

$$E(\omega) = i\omega A(\omega)$$

The absolute value of spectral components of the noise has a constant offset. When noise is multiplied with frequency the absolute value of the noise will rise linearly. But if the peak is due to a signal from the second harmonic, it should have a Gaussian envelope (figure 5.16 demonstrates this situation). As you can see, the spectral components between 0.5 to 1 PHz do not rise linearly. So, there is a possibility that this part of the spectrum is from the second harmonic radiation.

To further make sure that these components are in fact signal, two different spectral filters are applied to the signal. The first filter is from 0.25 PHz to 0.5 PHz (for the fundamental signal), the second is from 0.5 PHz to 1 PHz (for the second harmonics). Later, we perform the inverse Fourier transform on these two filtered signals, back to the time-domain (figure 5.17a show the inverse Fourier transform of these selected band). Next, we plot the second harmonics vs the fundamental (figure 5.17b). We can easily fit a parabolic function to it ( $E_{2\omega}(t) = \chi E_{\omega}^2(t)$ ).

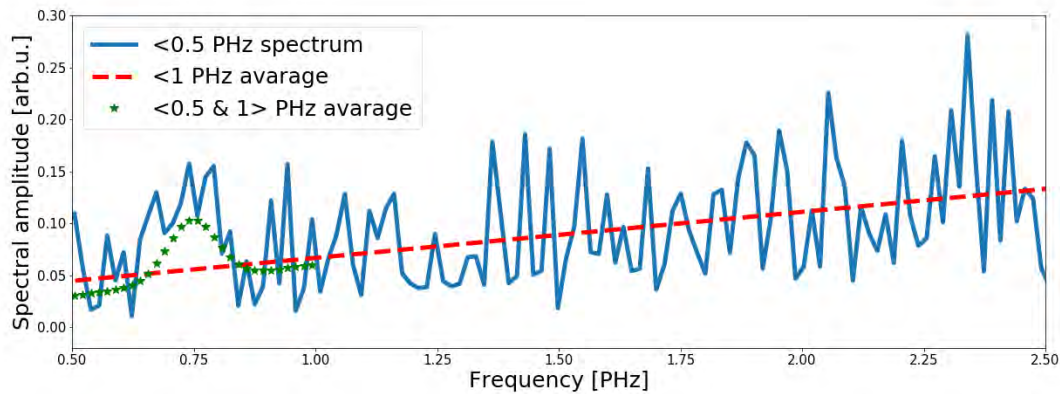


Figure 5.16. Higher frequency parts of the time derivative of the streaking signal of the generated second harmonic. The solid blue line is the spectral amplitude. The dashed red line is the linear fitting, which is used as an indicator that noise frequencies will get a linear increase when differentiated with respect to time. The green stars indicate that the part of frequency which should be the actual signal would have Gaussian behaved envelope.

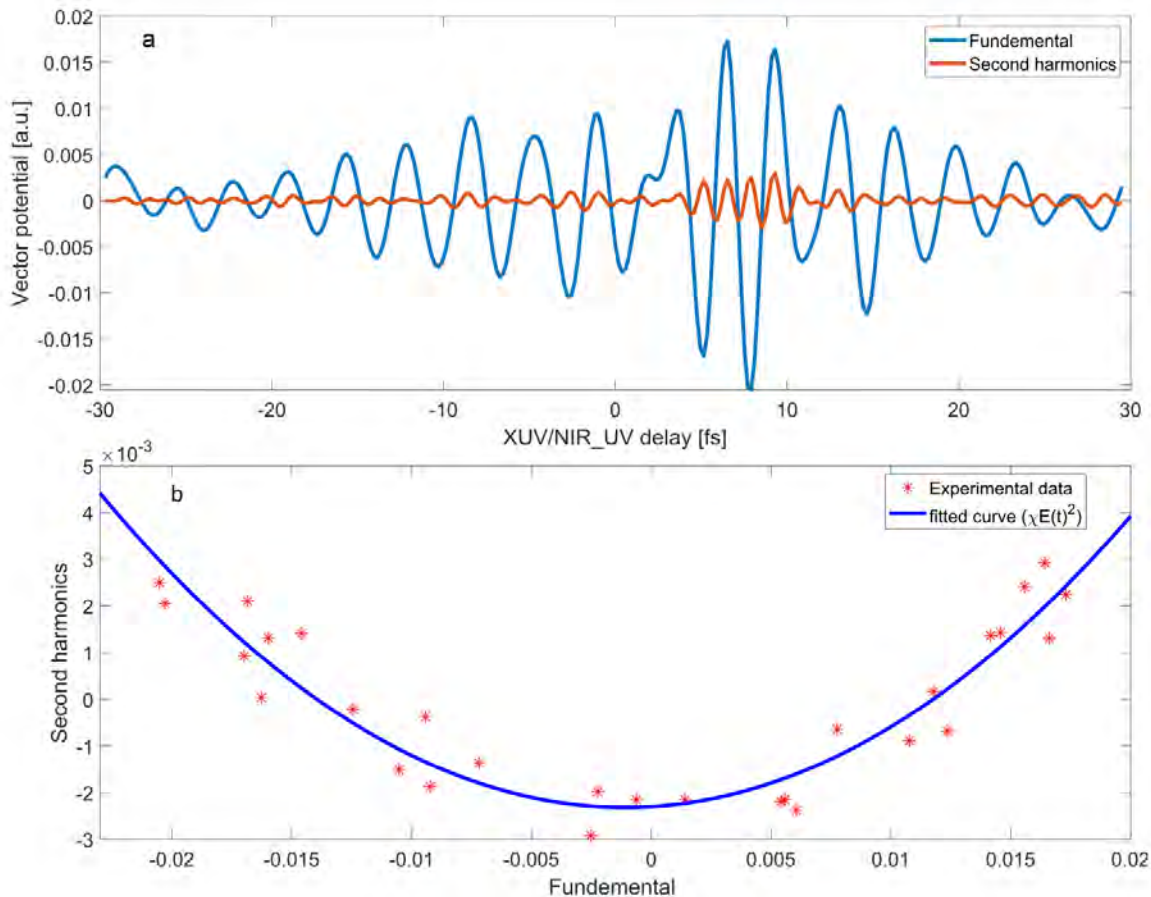


Figure 5.17. Comparison of the extracted second harmonics field with the fundamental field. a) the first comparison is performed in the time-domain, where the blue solid line is the retrieved vector potential, of the fundamental field (NIR, 780 nm), and the red solid line is the retrieved vector potential of the generated second harmonics field phase (phase-matched for 390 nm). The fundamental and the second harmonics trace are separated by applying a Fourier filter to the original data. b) comparison of the time derivative of the second harmonics signal vs the time derivative of the fundamental signal (i.e. electric field). The star data points are the experimental data and the blue solid line is fitted quadratic curve. This fitting is another indicator that the detected signal is the second harmonics of the fundamental signal since the amplitude scales quadratically.

Furthermore, for a more accurate selection of the bandwidth of the second harmonic signal, first, we choose a fundamental bandwidth. Then we calculate the time-domain second harmonics signal for this bandwidth range. Let  $f(t)$  be your signal (figure 5.18.a) and  $F(\nu)$  be the corresponding Fourier transform (figure 5.18.b). Let  $\nu_1$  and  $\nu_2$  be lower and upper limits of your fundamental signal (in this case  $\nu_1 = 0.2$  PHz and  $\nu_2 = 0.55$  PHz). The time-domain fundamental signal is:

$$f_{\text{fund}}(t) = \frac{1}{2\pi} \int_{\nu_1}^{\nu_2} F(\nu) e^{-i2\pi\nu t} d\nu \quad 5.18$$

Next, we take a square of the fundamental signal, and perform a Fourier transform of this signal to the frequency-domain.

$$f_{\text{sqr}}(t) = f_{\text{fund}}(t) \times f_{\text{fund}}(t) \quad 5.19$$

$$F_{\text{sqr}}(\nu) = \int_{-\infty}^{\infty} f_{\text{sqr}}(\nu) e^{i2\pi\nu t} d\nu$$

This spectrum consists of two spectral regions. The low-frequency part is due to optical rectification (OR) and DFG (figure 5.18.e the red triangles). The high-frequency part is due to SHG and SFG (figure 5.18.e the green hexagons). The SHG signal is extracted, by applying a high pass filter to this spectrum and then inverse Fourier transforming this spectrum to time-domain (figure 5.18.b blue curve).

Let  $\nu_3$  and  $\nu_4$  be the lower and upper limit of the  $F_{\text{sqr}}(\nu)$  for SHG, in this case above 0.5 and below 1 PHz, then  $f_{2\text{nd}}(t)$  is defined:

$$f_{2\text{nd}}(t) = \frac{1}{2\pi} \int_{\nu_3}^{\nu_4} F_{\text{sqr}}(\nu) e^{-i2\pi\nu t} d\nu \quad 5.20$$

Now that we know the bandwidth range of the second harmonics signal, we can take a Fourier filter of our original pulse and extract the SHG part of that signal. So, in  $F(\nu)$  we choose the bandwidth range  $\nu_3$  and  $\nu_4$  (i.e 0.5 to 1 PHz) and perform the inverse Fourier transform it back to time-domain (figure 5.18.b red curve).

Attosecond streaking results show, the second harmonic is detectable between 0.5 PHz to 1 PHz. In other words, in LPPS data if any spectral components between 0.5 PHz to 1 PHz are seen, these are definitely due to the electric field generated from SHG. Furthermore, these results show that the amplitude of the second harmonic signal is half of the component of polarization of fundamental signal that is parallel to the polarization of the second harmonics<sup>28</sup>.

---

<sup>28</sup> Recall that in order to have a reference between the fundamental and the second harmonics, we rotated the polarization of the fundamental such that, it has a some amplitude along the y-axis, while maintaining most of it amplitude along the x-axis (figure 5.15)

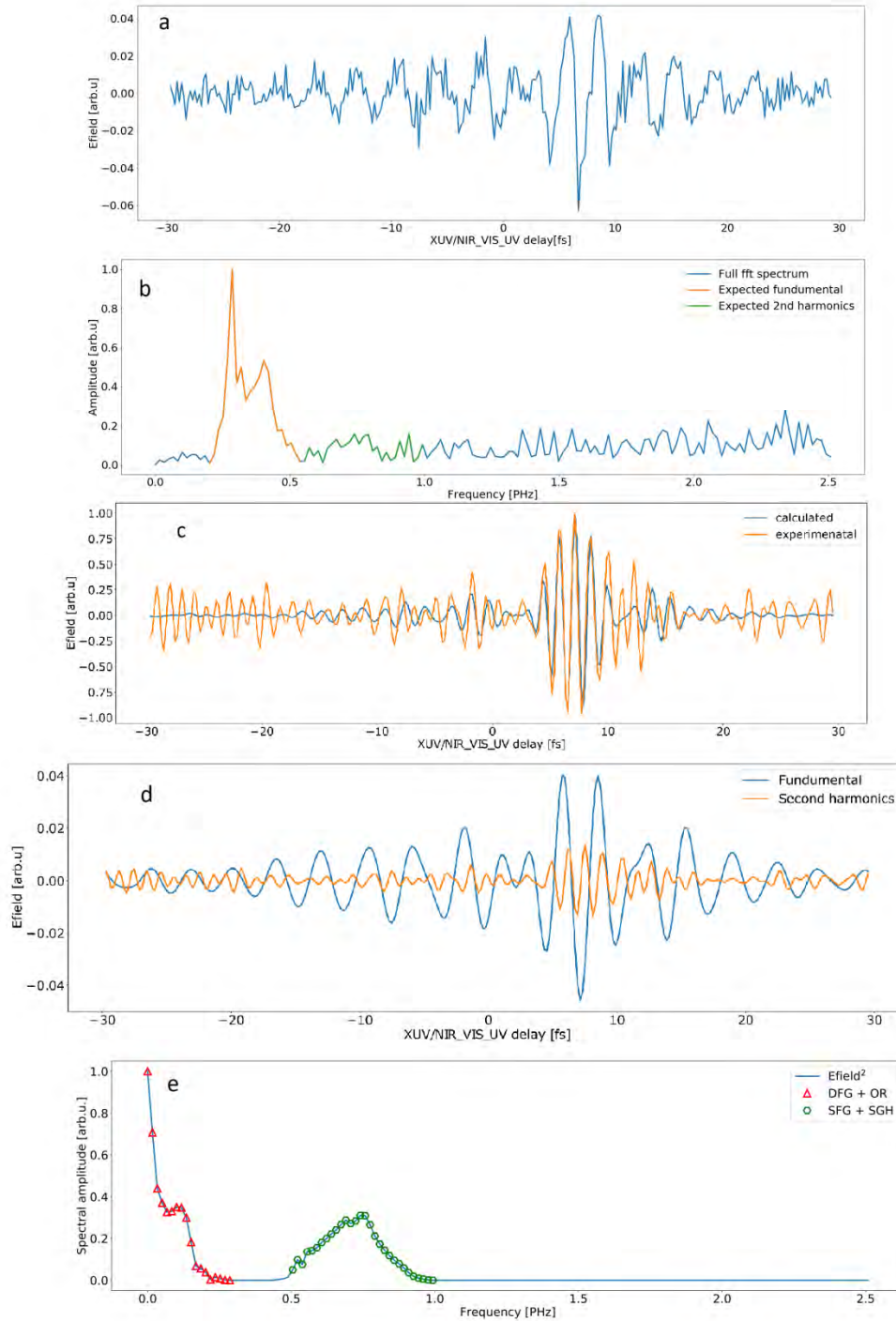


Figure 5.18. The final test for separating the signal from the noise of the second harmonics signal. a) Take the actual signal and differentiate it with respect to time. b) Calculate the square of the signal and perform the Fourier transform of it (blue the solid line is the Fourier transform of the, red triangles indicated DFG and OR parts, green hexagons indicate SFG and SHG. c) Apply a high pass spectral filter (choose only the hexagons) and perform an inverses Fourier transform it back in time-domain, meanwhile choose the same bandwidth (green hexagons) and apply it to the time derivative of the signal (the green sold region in the plot 5.22.d), the blue solid lines indicated the former and the red solid lines indicate the latter. As you can see, the two curves match each other perfectly where we have the strongest half cycles of the fundamental signal. This test is the final proof that what we have between 0.5 PHz and 1 PHz is in fact the current induced by the electric fields that is generated in our BBO.

### 5.6.6 Second harmonics detection by LPPS

The results from attosecond streaking show, the electric field amplitude of the measured second harmonics signal is half of the fundamental signal. Now that we know what is the frequency bandwidth of the second harmonics signal and how big is its amplitude, we set to detect the signal by LPPS in gases.

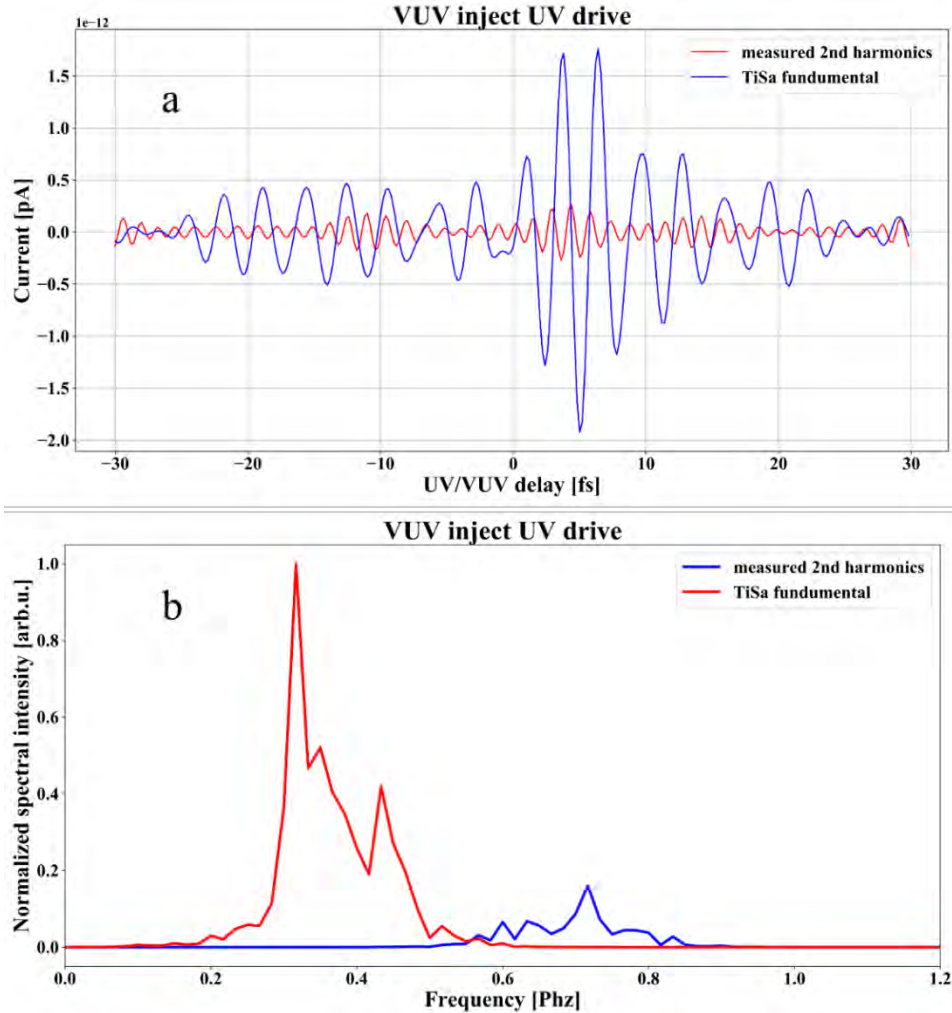


Figure 5.19. The measured LPPS current of the second harmonics field (@ 390 nm) and the fundamental field at (@ 780 nm). a) the time-domain current, where the blue solid line is the trace of the fundamental field and the red solid line is the trace of the second harmonics field. b) the Fourier transform of two spectral region blue the detected second harmonics part with spans from 0.5 to almost 0.9 PHz and the red solid curve indicates the spectral region of the fundamental field which is the same as the usual output from a Ti:Sa source (1000 to 500 nm).

The experimental results show (figure 5.19) that the amplitude of the detected second harmonics current is very weak with respect to the amplitude of the detected fundamental current. We expect to detect a stronger amplitude since we are using a phased-matched BBO crystal for second harmonics of 780 nm ( $\theta_{\text{BBO}} = 29.2^\circ$ ,  $\phi_{\text{BBO}} = 90^\circ$ ). The first reason is that; the current is proportional to the vector potential of the measured pulse. For the same electric field amplitude, the second harmonic vector potential amplitude ( $A_{2\omega}$ ) is half of the fundamental field's vector potential ( $A_\omega$ ).

The second reason is the direct result of the duration of injection. Using the simulation with HHGMax code we find out that the duration of injection for VUV injection between 21 and 26 eV photons is about 1 fs (figure 5.20.a). Looking at the result of the calculation of spectral sensitivity for this injection envelope (figure 5.20.b), it is evident that the sensitivity of the measured current drops almost by half in the blue part of the spectrum (above 0.7 PHz).

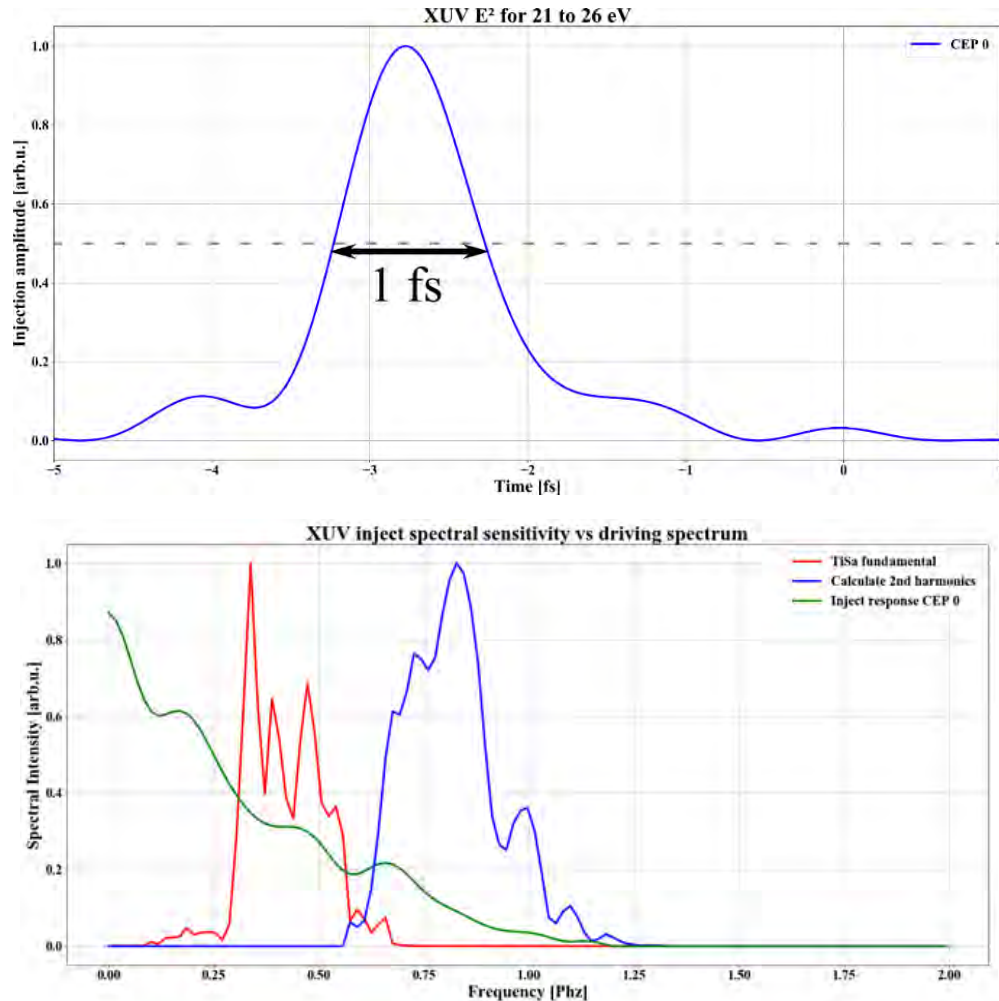


Figure 5.20. Spectral sensitivity of LPPS in Neon. a) The intensity envelope of the injecting VUV pulse. Since the LPPS signal is mainly from low-energy electrons with initial kinetic energy below 5 eV, it is safe to assume that injecting VUV has a bandwidth from 21 to 26 eV. This in return gives an injection duration of about 1 fs. b) The spectral sensitivity of the LPPS with injecting pulse from figure 5.23.a. red curve the spectrum of Ti:Sa, blue is calculated spectrum of second harmonics, and the green curve is the spectral sensitivity curve, which is Fourier transform of the square of the injecting field from VUV pulse which extends from 21 to 26 eV. As is evident the sensitivity drops by 50 % in the blue part due to the duration of injection.

The blue curve in figure 2.21 shows the calculated second harmonic time-dependent current (given if the second harmonic field amplitude is equal to fundamental field amplitude) and for the sake of comparison, the fundamental field calculated current is also plotted (red curve). As you can see, starting from the same field amplitude theoretically we will measure almost one-fifth of the fundamental signal. Further reduction of the signal amplitude is due to the fact that the second harmonics field amplitude is not the same as the fundamental field amplitude, and the reflectance of the mirrors after BBO is not the same as for the entire spectrum.

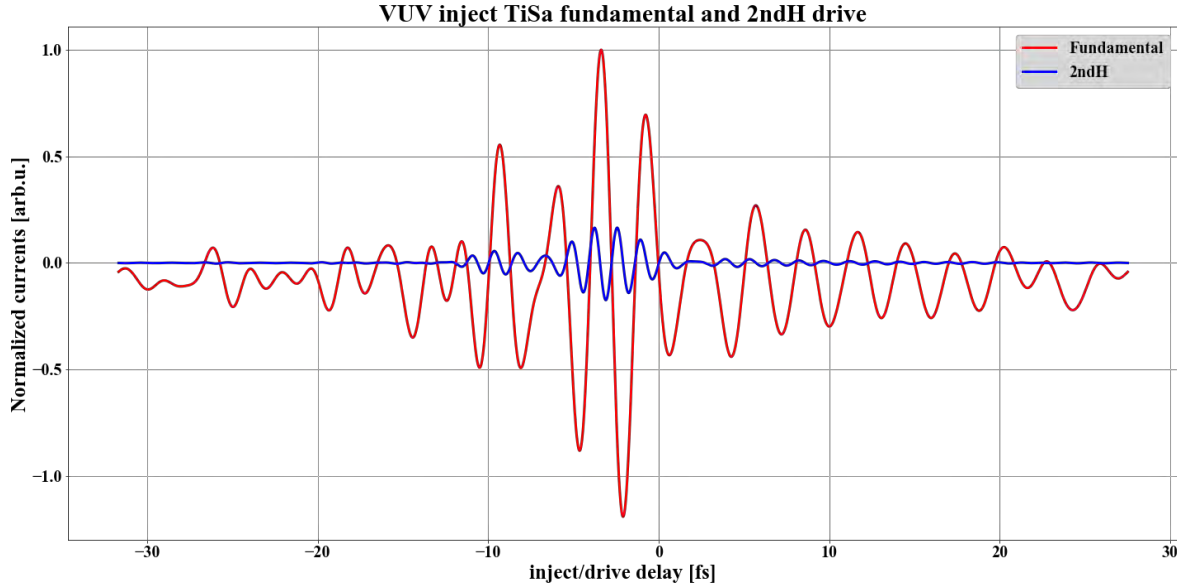


Figure 2.21. Comparison of the detected fundamental and second harmonics signal if both have the same amplitude of electric field envelope.

### 5.6.7 A recipe to increase SNR for second harmonics signal

In the following section, we will introduce a recipe to increase the SNR of the detected second harmonics current. As we mentioned before, the detected current in LPPS is the convolution of the vector potential of the driving pulse and the injection envelope, which is the square modulus of the electric field of the VUV injection pulse, (Eq. 4.5). Since we create the VUV injection source from the fundamental of our Ti:Sa laser, the UVU bursts are spaced by one half-cycle of our NIR transient. We have mentioned before that according to Eq. 4.5, if we have odd numbers of injection incidents, then the measured current from the NIR transient has a high SNR.

The situation is different when we create the second harmonic of the NIR (let's call it UV pulse). Here the spacing of the injection field is no longer one half-cycle of the UV pulse but rather one full-cycle of the UV pulse. Our simulation of HHG with the HHGMAX code shows that for CEP 0 of the NIR field that generates the VUV radiation (21 to 26 eV), the VUV pulse train has only one strong burst (the blue curve figure 5.9). When we change the CEP to  $\pi/2$  then we get two VUV bursts (the red curve in figure 5.8).

If we have two instances of injection, according to Eq. 4.5, we add the neighboring cycles of the UV field; therefore, we expect to get double the amplitude of the CEP 0 case.

If Eq. 4.5 is used to calculate the spectral response of both cases for the measured current from the second harmonics pulse as the driving field, then as we predicted, we see that the sensitivity of the response with CEP  $\pi/2$  (figure 5.22 black curve) is almost twice the case of CEP 0 (figure 5.22 green curves). Although we can increase the sensitivity of current detection at second harmonics of Ti:Sa, we will create a hole in the spectrum of fundamental pulse.

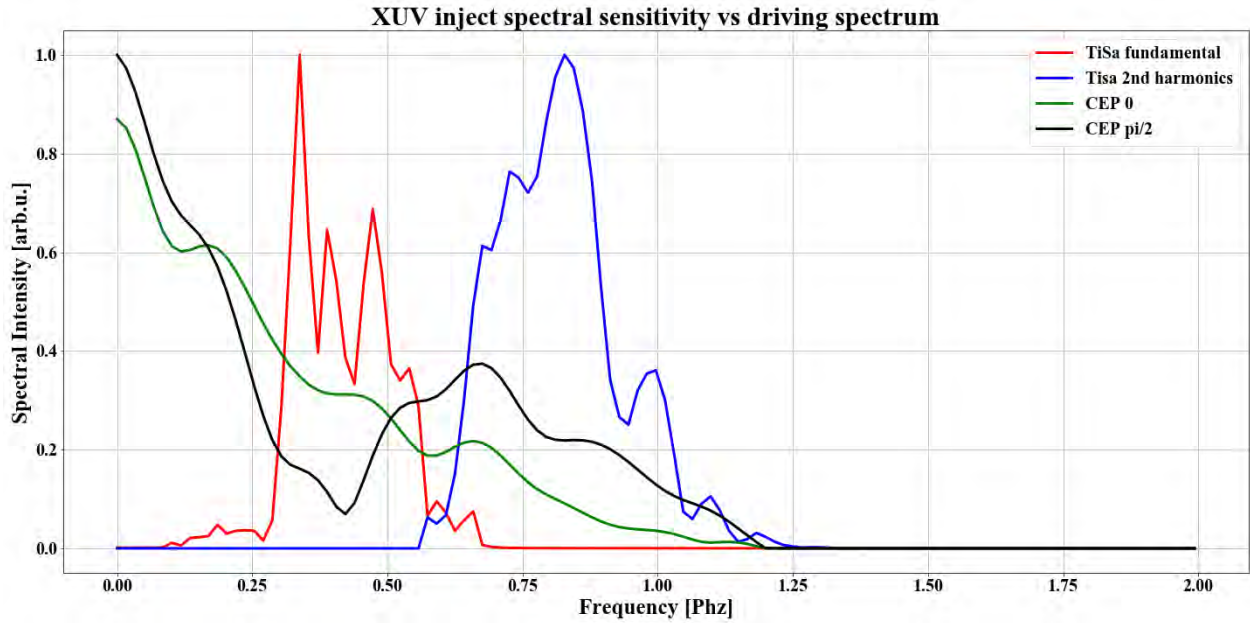


Figure 5.22. The CEP dependence of spectral response  $b$  of the LPPS for fundamental and second harmonics spectrum of the Ti:Sa source. The red solid curve is the spectrum of fundamental NIR pulse and the blue solid curve is the spectrum of the second harmonic pulse. The green curve is the response of the LPPS at CEP 0 and the black curve is the sensitivity at CEP  $\pi/2$ .

According to Eq. 4.6, the spectrum of the current is proportional to the spectrum of the vector potential times the spectrum of the injection's envelope. Calculation of the Eq. 4.5 for the Ti:Sa fundamental, and the calculated second harmonics of the Ti:Sa, for both CEPs (0 and  $\pi/2$ ), are shown in figure 5.23.

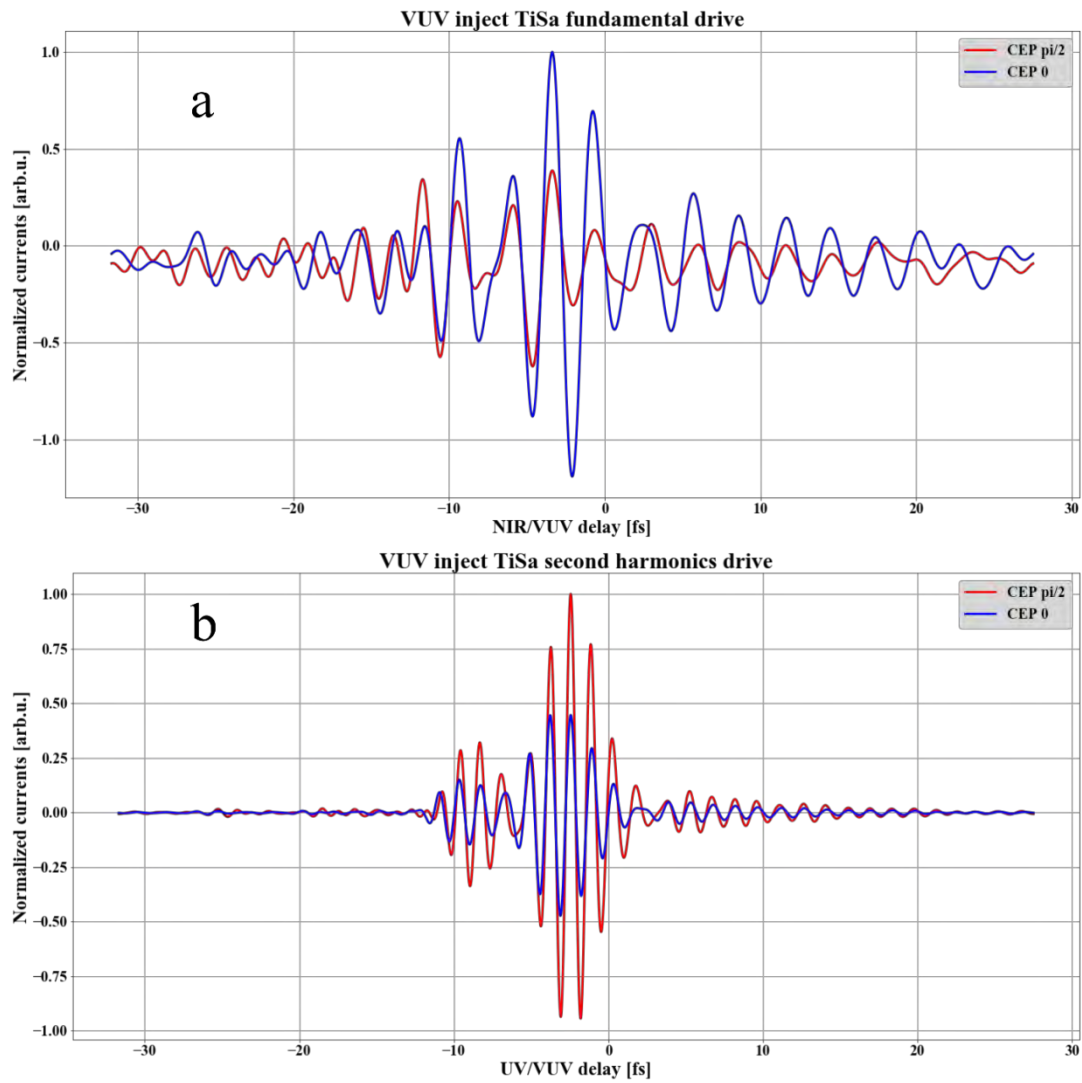


Figure 5.23. Comparison of the calculated time-dependent signal based on different CEPs. a) The fundamental signal (blue curve is for CEP 0 and the red curve is for CEP  $\pi/2$ ). b) The second harmonics signal (blue curve is for CEP 0 and the red curve is for CEP  $\pi/2$ ).

## 5.7. Conclusion of LPPS in gases

The results of LPPS in Ne show that in terms of bandwidth and dynamic range supersedes LPPS in LiF. These are the direct consequences of two important properties that Ne has in comparison to a LiF; 1) the energy of linear transition in Ne is larger than the case of the LiF (21.6 eV vs 13.5 eV). Since higher harmonics are created in a shorter time scale, the transition time happens in a shorter time scale; 2) ionized state of an electron in Ne case have infinitely large parabolic dispersion relation. This first means the bandwidth of the transition, in this case, can be infinitely large and as a result even shorter transition time. Furthermore, the factor that limited the Dynamic range of LPPS signal in LiF was the finite size of its band first CB. The removal of this limitation in Ne increased the LPPS dynamic range from 27 dB to over 44 dB. We predict LPPS in Ne can reach 56 dB can be reached before the field strength of the optical transient can ionize the Ne atoms.

Although, Ne has an infinitely parabolic free-electron state, the sensitivity of signal detection of LPPS in Ne for frequencies above 0.7 PHz drops below 20 %. For the case of LPPS, it is expected that the existence of infinitely large parabolic CB would result in a large bandwidth of photo-conduction which reduces the photo-injection duration and consequently large bandwidth of detection. This result is only possible when the external circuit of current detection only sees the electric field of the asymptotic dipole from the injection and the driving process. In the case of LPPS in gases, since the source of the signal is the transport of photo-electrons to electrodes, the signal from fast electrons only creates a large constant current offset. Fast electrons only need a few picoseconds to reach electrodes while mechanisms such as population transfer and the metallic barrier transmission probability cannot modulate the population of the received electrons to electrodes. Based on the cutoff of the spectral sensitivity of LPPS in Ne we predict that only electrons with below 5 eV initial kinetic energy, contribute to the detected LPPS signal (i.e. photo-ionization with UVU photons from 21.6 to 26.6 eV). The Fourier limit of this photo-ionization pulse is 247 as. But VUV generated by the high harmonic generation is not compressed. The calculations VUV pulse for this range show a pulse duration of 1 fs.

With the mentioned photo-ionizing pulse (21.56 eV to 26.56 eV with pulse duration of 1 fs) the detection of frequencies above 0.7 PHz is challenging. Furthermore, since the LPPS current is proportional to the vector potential of the field, the sensitivity of detection of higher frequencies drops inversely with respect to frequency. Our proposed scheme of to XUV pulse that can provide two instance of injection which are separated in time by one half-cycle of the NIR pulse seems to increase the sensitivity of detection of second harmonic frequencies with a fundamental pulse (1000 nm to 500 nm). While this method increases the sensitivity of detection by a factor of two, the absolute phase of the detected frequencies becomes unknown. We can guess this absolute phase if we have the temporal structure of the injection envelope. For this purpose, we can perform a CEP scan and treat integral 4.2 as the case of the FROG. Once this injection envelope is determined the full phase of the 2nd harmonics field can be extracted. This can push the extent of detection of frequencies up to 1.2 PHz.



# 6. Conclusion and outlooks

The experimental results of this work show that LPPS, both in large bandgap solids and inert gases, can be used as a new method for the time-resolved measurement of the electric field of optical pulses. The main motivation for introducing this method in contrast to NPS is to reduce the complications arising from the nonlinear nature of photoconduction in NPS. We showed that linear injection using VUV pulses, generated by means of high harmonics generation, creates an attosecond Auston switch. By proper selection of the bandwidth of injection, the method can become analogous to attosecond streaking in large bandgap materials.

We have shown that, with linear injection, we can measure the electric field of the NIR transients with intensities up to  $0.4 \text{ TW/cm}^2$  linearly, corresponding to field amplitude of  $0.24 \text{ V/\AA}$ . This result is possible because the first conduction band of the LiF has a large parabolic extend and the energy difference between the first and the second conduction band is large. Moreover, we can detect light pulses down to intensities of  $1 \text{ GW/cm}^2$ , which correspond to field amplitude of  $0.08 \text{ V/\AA}$ . When averaging over an estimated 108 ultraviolet photons per second, we achieve a signal-to-noise ratio for the driving field intensity structure of 26 dB in the linear regime. Using VUV pulses as source linear photo-conduction also reduces the chance of damaging the medium, that's why strong driving fields with intensities up to  $0.4 \text{ TW/cm}^2$  did not damage our sample.

The spectral sensitivity of LPPS in LiF does not surpass the frequencies above 0.5 PHz. This is the direct consequence of the limited electronic switching speed in LiF. By comparing the results of the spectral bandwidth of the LPPS in LiF and attosecond streaking we could estimate an injection duration of 1.3 fs. We have shown that further compression of the injecting pulse by increasing its bandwidth will not increase the detected bandwidth because this leads to the occupation of more empty states in the first CB of LiF. As a result, driving fields with lower field amplitude can easily move the electrons toward non-parabolic parts of the CB and transit these electrons to higher CBs. In both cases, the averaged group velocity of the Bloch waves will be less. As a result, SNR and the bandwidth of detection will decrease. Therefore, a faster injection time might not be suitable for current detection. We concluded that the perfect condition for LPPS in solids is a material with a large bandgap and large parabolic CB.

Learning from the experience with solids, we used gases to investigate if we can increase the upper limit in the bandwidth of detection of LPPS. The results indicated that we can push this limit toward 1 PHz (i.e. 300 nm). Also, as a byproduct of the infinite parabolic dispersion of the ionized states of the free electrons from Ne, we could increase the dynamic range of the measurement to 44 dB, this is the upper limit only due to the fact that we couldn't send more power to the Delay arm of our setup. If this limit is removed, we can reach up to 56 dB of dynamic range.

We observed that the source of the detected current for the case of LPPS in Ne was the transport of the ionized electrons with initial kinetic energies of 0 to 5 eV. Due to the effect of the transport, the SNR of LPPS in Ne was 100 times stronger than the case of LiF for the same driving field amplitude.

We expect that we can increase the upper limit of the bandwidth of detection by using bias voltage across the electrodes. In this way, we expect to block electrons with initial kinetic energies below half the voltage of the bias. Since the higher energy electrons are ionized by higher energy photons, we expect to get a shorter injection time and a higher cutoff of detected frequency.

The CEP of the injecting pulse plays an important role in the amplitude and bandwidth of the measurement. We have seen two different ways it can affect the signal. For the bandwidth of the frequencies of the NIR transient, setting the CEP to 0 will give the best SNR. Since the HHG radiation is generated by the same source, setting the CEP to 0 rad will generate only one dominant instance of ionization in neon. This is the same case as in LiF which results in large SNR. Setting the CEP to  $\text{CEP } \pi/2$  would result in 2 instances of ionization which are separated by one half-cycle of the NIR field which would reduce the SNR. But for the frequencies which have double the value,  $\text{CEP} = \pi/2$  rad results in better SNR. The reason is that at this CEP, for which we have 2 instances of injection, the spacing of the injection instances, in time, is one complete cycle. Therefore, the SNR becomes twice the case of  $\text{CEP} = 0$  rad.

One of the limiting factors for the detection bandwidth of the LPPS is the duration of the injection. A VUV pulse with 5 eV photon energy bandwidth centered around 23 eV should have almost 400 as pulse duration at Fourier limit. One of the shortcomings in creating such a pulse via HHG is that this pulse will be inherently chirped. Therefore, the pulse duration is much longer (around 1 fs) than the Fourier limit. Proper compression of these pulses can lead to shorter injection times in Ne and, as a result, larger bandwidth of detection.

We conclude that LPPS in neon can be used as a proper technique to replace attosecond streaking for measurement of the time-dependent electric field of the optical transients. The high SNR of this method provides us with fast measurements<sup>29</sup>. It can also resolve electric field oscillations as small as  $0.003 \text{ V/\AA}$ . In comparison to attosecond streaking, this lower limit is 20 times smaller, which makes LPPS a far superior technique for time resolve spectroscopy measurements where the amplitude of the radiated spectra from the sample is minute. The recipe is simple just put one electrode at the point of measurement and read the current. Since this current is proportional to the vector potential of the driving pulse there is no need for rigorous numerical calculations for retrieval of the vector potential as is the case for the attosecond streaking.

One shortcoming of this technique as well as other techniques which we discussed in this thesis is that it cannot give information about the temporal structure of the injecting pulse. This information is crucial for the initial calibration of any measurement technique and is only provided by the attosecond streaking. We can retrieve this information only if we can do a series of scans by changing the CEP of the injection source.

The ability to switch on the large bandgap materials at near-petahertz frequencies is the first step in creating optoelectronic switches at optical frequencies. The next step is to create such a switch is to turn off the conductivity. Ultra-fast linear injection creates electronic Bloch wave-packets in the CB. And the subsequent optical drive will leave the electron in a position in CB, determined by the vector potential of the optical drive at the moment of carrier injection; but, after the optical drive is gone, the electron will stay at this  $k$  point in the CB until, due to some thermal effects, it recombines with the corresponding hole in VB. The thermalization time is on the order of a few tens of femtoseconds. Future studies should focus on finding a solution for faster electron hole recombination or removal of these carriers from CB. Promising results on optical assisted carrier transfer in multilayered Nickel-Platinum thin films have been reported by F. Siegrist et.al [119]. We predict these kinds of carrier elimination can be helpful to create ultimate petahertz switches.

---

<sup>29</sup> It takes 30 seconds to measure a temporal window of 50 fs, while such measurements with attosecond streaking would take 12 and a half minutes with the same laser source.





# Bibliography

- [1] Schötz, Johannes, et al. "Perspective on petahertz electronics and attosecond nanoscopy." *ACS photonics* 6.12 (2019): 3057-3069.
- [2] Garg, M., Zhan, M., Luu, T. et al. Multi-petahertz electronic metrology. *Nature* 538, 359–363 (2016).
- [3] L. D. Nguyen, L. E. Larson, U. K. Mishra, "Ultra-high-speed modulation-doped field-effect transistors: A tutorial review," *Proc. IEEE*, vol. 80, no. 4, p. 494, 1992.
- [4] X. Mei et al., "First Demonstration of Amplification at 1 THz Using 25-nm InP High Electron Mobility Transistor Process," in *IEEE Electron Device Letters*, vol. 36, no. 4, pp. 327-329, April 2015, doi: 10.1109/LED.2015.2407193.
- [5] E. Goulielmakis, V. S. Yakovlev, A. L. Cavalieri, M. Uiberacker, V. Pervak, A. Apolonski, R. Kienberger, U. Kleineberg, F. Krausz, "Attosecond control and measurement: Lightwave electronics". *Science* 10 Aug 2007: 769-775
- [6] Rode, D. L. "Electron mobility in direct-gap polar semiconductors." *Physical Review B* 2.4 (1970): 1012.
- [7] D. H. Auston, K. P. Cheung, and P. R. Smith, "Picosecond photoconducting Hertzian dipoles", *Appl. Phys. Lett.* 45, 284 (1984)
- [8] Schmuttenmaer, Charles A. "Exploring dynamics in the far-infrared with terahertz spectroscopy." *Chemical reviews* 104.4 (2004): 1759-1780.
- [9] Nuss, Martin C., and Joseph Orenstein. "Terahertz time-domain spectroscopy." *Millimeter and submillimeter wave spectroscopy of solids* (1998): 7-50.
- [10] J. F. Holzman, F. E. Vermeulen, and A. Y. Elezzabi, "Ultrafast photoconductive self-switching of subpicosecond electrical pulses", *IEEE JOURNAL OF QUANTUM ELECTRONICS*, VOL. 36, NO. 2, FEBRUARY 2000.
- [11] Hohenleutner, M., Langer, F., Schubert, O. et al. Real-time observation of interfering crystal electrons in high-harmonic generation. *Nature* 523, 572–575 (2015)
- [12] Ghimire, S. et al. Observation of high-order harmonic generation in a bulk crystal. *Nat. Phys.* 7, 138–141 (2011).
- [13] Lakhotia, Harshit, et al. "A real space perspective of high harmonic generation in crystalline solids." *CLEO: QELS\_Fundamental Science*. Optical Society of America, 2018.
- [14] Ghimire, S., Reis, D.A. High-harmonic generation from solids. *Nature Phys* 15, 10–16 (2019).
- [15] Schultze, M. et al. Controlling dielectrics with the electric field of light. *Nature* 493, 75–78 (2013)
- [16] Gessner, Julia Anthea. Strong-Field Driven Charge and Spin Dynamics in Solids. Diss. Imu, 2021.
- [17] Mashiko, H., Oguri, K., Yamaguchi, T. et al. petahertz optical drive with wide-bandgap semiconductor. *Nature Phys* 12, 741–745 (2016).
- [18] Sommer, A., Bothschafter, E., Sato, S. et al. Attosecond nonlinear polarization and light–matter energy transfer in solids. *Nature* 534, 86–90 (2016).

- [19] MLA. Jackson, John David, 1925-2016. *Classical Electrodynamics*. New York: Wiley, 1999.
- [20] Goulielmakis, Eleftherios, et al. "Single-cycle nonlinear optics." *Science* 320.5883 (2008): 1614-1617.
- [21] Krausz, Ferenc, and Misha Ivanov. "Attosecond physics." *Reviews of modern physics* 81.1 (2009): 163.
- [22] Goulielmakis, Eleftherios, et al. "Real-time observation of valence electron motion." *Nature* 466.7307 (2010): 739-743.
- [23] Itatani, J., et al. "Attosecond streak camera." *Physical review letters* 88.17 (2002): 173903.
- [24] Boyd, R. W. *Nonlinear Optics* (Academic Press, Elsevier, 2008)
- [25] J. A. Valdmanis, G. Mourou and C. W. Gabel, "Picosecond electrooptic sampling system", *Appl. Phys. Lett.* 41 (3), 211 (1982)
- [26] J. A. Valdmanis, G. Mourou, and C. Gabel, "Subpicosecond electrical sampling", *IEEE J. Quantum Electron.* 19 (4), 664 (1983)
- [27] J. A. Valdmanis and G. Mourou, "Subpicosecond electrooptic sampling: principles and applications", *IEEE J. Quantum Electron.* 22 (1), 69 (1986)
- [28] Keiber, S., Sederberg, S., Schwarz, A. et al. Electro-optic sampling of near-infrared waveforms. *Nature Photon* 10, 159–162 (2016).
- [29] E. Ridente et al. Electro-optic characterization of synthesized infrared-visible light fields". In: *Nature Communications* (Submitted) (2021).
- [30] S. B. Park, K. Kim, W. Cho, S. I. Hwang, I. Ivanov, C. H. Nam, and K. T. Kim, "Direct sampling of a light wave in air," *Optica* 5, 402–408 (2018).
- [31] Cho, W., Hwang, S.I., Nam, C.H. et al. Temporal characterization of femtosecond laser pulses using tunneling ionization in the UV, visible, and mid-IR ranges. *Sci Rep* 9, 16067 (2019).
- [32] A. Korobenko, K. Johnston, M. Kubullek, L. Arissian, Z. Dube, T. Wang, M. Kübel, A. Yu. Naumov, D. M. Villeneuve, M. F. Kling, P. B. Corkum, A. Staudte, and B. Bergues, "Femtosecond streaking in ambient air", *Optica* Vol. 7, Issue 10, pp. 1372-1376 (2020)
- [33] S. V. Popruzhenko, "Keldysh theory of strong field ionization: history, applications, difficulties and perspectives.", 2014 *J. Phys. B: At. Mol. Opt. Phys.* 47 204001
- [34] Hwang, Sung In, et al. "Generation of a single-cycle pulse using a two-stage compressor and its temporal characterization using a tunneling ionization method." *Scientific reports* 9.1 (2019): 1-6.
- [35] Kim, K., Zhang, C., Shiner, A. et al. petahertz optical oscilloscope. *Nature Photon* 7, 958–962 (2013).
- [36] Schiffrin, A. et al. Optical-field-induced current in dielectrics. *Nature* 493, 70–74 (2012).
- [37] Sederberg, S., Zimin, D., Keiber, S. et al. Attosecond optoelectronic field measurement in solids. *Nat Commun* 11, 430 (2020).
- [38] Roncin, Jean-Yves, et al. "The vacuum ultraviolet absorption bands of the pink afterglow spectrum of molecular nitrogen revisited at high resolution." *Journal of molecular spectroscopy* 194.2 (1999): 243-249.

- [39] Zimin, Dmitry. "petahertz optoelectronics via attosecond control of solids.", LMU PhD dissertation, 2021
- [40] Seres, Enikoe, Jozsef Seres, and Christian Spielmann. "X-ray absorption spectroscopy in the keV range with laser generated high harmonic radiation." *Applied Physics Letters* 89.18 (2006): 181919.
- [41] Dromey, B., et al. "Bright multi-keV harmonic generation from relativistically oscillating plasma surfaces." *Physical Review Letters* 99.8 (2007): 085001.
- [42] Brabec T. and Krausz F., 2000 *Rev. Mod. Phys.* 72 545.
- [43] Krause, Jeffrey L.; Schafer, Kenneth J.; Kulander, Kenneth C. (1992). "High-order harmonic generation from atoms and ions in the high intensity regime". *Physical Review Letters*. 68 (24): 3535–3538.
- [44] Corkum, P. B. (1993). "Plasma perspective on strong field multiphoton ionization". *Physical Review Letters*. 71 (13): 1994–1997.
- [45] K. C. Kulander, K. J. Schafer, and J. L. Krause, in *Proceedings of the Super Intense Laser-Atom Physics III Workshop*, Vol. 316 of NATO Advanced Study Institute, Series B: Physics (Plenum Press, New York, 1993).
- [46] Connerade, Jean-Patrick. *Highly excited atoms*. No. 9. Cambridge University Press, 1998. p. 339
- [47] K. C. Kulander, K. J. Schafer, and J. L. Krause, in *Proceedings of the Super Intense Laser-Atom Physics III Workshop*, Vol. 316 of NATO Advanced Study Institute, Series B: Physics (Plenum Press, New York, 1993).
- [48] CHIN, S. L. (2004). "From multiphoton to tunnel ionization". *Advances in Multi-Photon Processes and Spectroscopy*. 16. WORLD SCIENTIFIC. pp. 249–271.
- [49] M. Lewenstein, Ph. Balcou, M. Yu. Ivanov, A. L'Huillier, and P. B. Corkum, "Theory of High Harmonic Generation by low-frequency laser fields," *Phys. Rev. A*. 49, 2117-2132 (1994).
- [50] Volkov D. M. 1935 *Z. Phys.* 94 250
- [51] Beretetskii V. B., Lifshitz E. M. and Pitaevskii L. P. 1971 *Quantum Electrodynamics* (Oxford: Butterworth-Heinemann)
- [52] Heitler, Walter. *The quantum theory of radiation*. Courier Corporation, 1984
- [53] T. Brabec and F. Krausz, "Intense few-cycle laser fields: Frontiers of nonlinear optics," *Reviews of Modern Physics*, vol. 72, no. 2, pp. 545–591, 2000.
- [54] Lytle, Amy Louise. *Phase matching and coherence of high-order harmonic generation in hollow waveguides*. Diss. University of Colorado at Boulder, 2008.
- [55] K. Kulander, K. Schafer, and J. Krause, "Dynamics of short-pulse excitation, ionization, and harmonic conversion," in *Super-Intense Laser-Atom Physics*, B. Piraux, A. L'Huillier, and K. Rzazewski, Eds., vol. 316. Han-sur-Lesse, Belgium: Plenum, 1993, pp. 95–110
- [56] B. Dromey, M. Zepf, M. Landreman, and S. M. Hooker, "Quasi-phasematching of harmonic generation via multimode beating in waveguides," *Optics Express*, vol. 15, no. 13, pp. 7894–7900, 2007.
- [57] Kazamias, S., and Ph Balcou. "Intrinsic chirp of attosecond pulses: Single-atom model versus experiment." *Physical Review A* 69.6 (2004): 063416.

- [58] de Bohan, A., Antoine, P., Milosevic, D. B. & Piraux, B. Phase-dependent harmonic emission with ultrashort laser pulses. *Phys. Rev. Lett.* 81, 1837–1840 (1998).
- [59] Nisoli, M. et al. Effects of carrier-envelope phase differences of few-optical-cycle light pulses in single-shot high-order-harmonic spectra. *Phys. Rev. Lett.* 91, 213905 (2003).
- [60] Becker, W., S. Long, and J. K. McIver. "Modeling harmonic generation by a zero-range potential." *Physical Review A* 50.2 (1994): 1540.
- [61] Ferray, M.; et al. (1988). "Multiple-harmonic conversion of 1064 nm radiation in rare gases". *Journal of Physics B: Atomic, Molecular and Optical Physics*. 21 (3): L31.
- [62] Li, X. F.; L'Huillier, A.; Ferray, M.; Lompre, L. A.; Mainfray, G. (1989). "Multiple-harmonic generation in rare gases at high laser intensity". *Physical Review A*. 39 (11): 5751–5761.
- [63] Wildenauer, J. "Generation of the ninth, eleventh, and fifteenth harmonics of iodine laser radiation." *Journal of applied physics* 62.1 (1987): 41-48.
- [64] G. Sansone, E. Benedetti, F. Calegari, C. Vozzi, L. Avaldi, R. Flammini, L. Poletto, P. Villoresi, C. Altucci, R. Velotta, S. Stagira, S. D. Silvestri, and M. Nisoli, "Isolated Single-Cycle Attosecond Pulses," *Science*, vol. 314, pp. 443-446, 2006.
- [65] M. Hentschel et al., *Nature* 2001, 414, 501.
- [66] E. Goulielmakis et al. *Science* 2004, 305, 1267.
- [67] Yakovlev, Vladislav S., Ferdinand Bammer, and Armin Scrinzi. "Attosecond streaking measurements." *journal of modern optics* 52.2-3 (2005): 395-410.
- [68] Stephens W. E. (1946). "A Pulsed Mass Spectrometer with Time Dispersion". *Phys. Rev.* 69 (11–12): 691
- [69] Wiza, Joseph Ladislav. "Microchannel plate detectors." *Nucl. Instrum. Methods* 162.1-3 (1979): 587-601.
- [70] Kienberger, R., Goulielmakis, E., Uiberacker, M. et al. Atomic transient recorder. *Nature* 427, 817–821 (2004).
- [71] Gagnon, Justin, and Vladislav S. Yakovlev. "The robustness of attosecond streaking measurements." *Optics express* 17.20 (2009): 17678-17693.
- [72] F. Quéré, Y. Mairesse, J. Itatani, "Temporal characterization of attosecond XUV fields". *J. Mod. Opt.* 52, 339–360 (2005).
- [73] Kohn, Walter, and Lu Jeu Sham. "Self-consistent equations including exchange and correlation effects." *Physical review* 140.4A (1965): A1133.
- [74] Runge, Erich, and Eberhard KU Gross. "Density-functional theory for time-dependent systems." *Physical Review Letters* 52.12 (1984): 997.
- [75] Marques, Miguel, et al. *Time-dependent density functional theory*. Vol. 706. Springer Science & Business Media, 2006.
- [76] Ashcroft, Neil W., and N. David Mermin. "Solid state physics." (1976).
- [77] L. Landau (1932). "Zur Theorie der Energieubertragung. II". *Physikalische Zeitschrift der Sowjetunion*. 2: 46–51.

- [78] C. Zener (1932). "Non-Adiabatic Crossing of Energy Levels". *Proceedings of the Royal Society of London A*. 137 (6): 696–702.
- [79] E. C. G. Stueckelberg (1932). "Theorie der unelastischen Stöße zwischen Atomen". *Helvetica Physica Acta*. 5: 369.
- [80] E. Majorana (1932). "Atomi orientati in campo magnetico variabile". *Il Nuovo Cimento*. 9 (2): 43–50.
- [81] C. Wittig (2005). "The Landau–Zener Formula". *Journal of Physical Chemistry B*. 109 (17): 8428–8430.
- [82] Rubbmark, Jan R., et al. "Dynamical effects at avoided level crossings: A study of the Landau-Zener effect using Rydberg atoms." *Physical Review A* 23.6 (1981): 3107.
- [83] Torosov, Boyan T., and Nikolay V. Vitanov. "Pseudo-hermitian landau-zener-stückelberg-majorana model." *Physical Review A* 96.1 (2017): 013845.
- [84] D. E. Spence, P. N. Kean, W. Sibbett, "60-fsec pulse generation from a self-mode-locked Ti:sapphire laser", *Opt. Lett.* 16 (1), 42 (1991)
- [85] F. Salin et al., "Modelocking of Ti:sapphire lasers and self-focusing: a Gaussian approximation", *Opt. Lett.* 16 (21), 1674 (1991)
- [86] S. Chen and J. Wang, "Self-starting issues of passive self-focusing mode locking", *Opt. Lett.* 16 (21), 1689 (1991)
- [87] T. Brabec et al., "Kerr lens mode locking", *Opt. Lett.* 17 (18), 1292 (1992)
- [88] Koke, Sebastian, et al. "Direct frequency comb synthesis with arbitrary offset and shot-noise-limited phase noise." *Nature Photonics* 4.7 (2010): 462-465.
- [89] H. R. Telle et al. "Carrier-envelope offset phase control: A novel concept for absolute optical frequency measurement and ultrashort pulse generation". In: *Applied Physics B* 69.4 (1999), pp. 327–332.
- [90] Lücking, Fabian, et al. "Long-term carrier-envelope-phase-stable few-cycle pulses by use of the feed-forward method." *Optics letters* 37.11 (2012): 2076-2078.
- [91] Strickland, Donna; Mourou, Gerard (1985). "Compression of amplified chirped optical pulses". *Optics Communications*. Elsevier BV. 56 (3): 219–221.
- [92] Schweinberger, Hans Wolfgang. A laser source for the generation of intense attosecond pulses and its first applications. Diss. lmu, 2014.
- [93] David F. Hotz, "Gain Narrowing in a Laser Amplifier," *Appl. Opt.* 4, 527-530 (1965)
- [94] Pierre Tournois (1997). "Acousto-optic programmable dispersive filter for adaptive compensation of group delay time dispersion in laser systems". *Optics Communications*. 140 (4–6): 245–249.
- [95] F. Verluise, V. Laude, Z. Cheng, Ch. Spielmann, and P. Tournois. Amplitude and phase control of ultrashort pulses by use of an acousto-optic programmable dispersive filter: pulse compression and shaping. *Opt. Lett.*, 25(8):575–577, Apr 2000.
- [96] S. Kane and J. Squier. Grism-pair stretcher–compressor system for simultaneous second- and third-order dispersion compensation in chirped-pulse amplification. *J. Opt. Soc. Am. B*, 14(3):661–665, Mar 1997.
- [97] Agrawal, Govind P. (2001). *Nonlinear Fiber Optics* (3rd ed.). San Diego, CA, USA: Academic Press.

- [98] Yang, G. and Y.R. Shen (1984) Spectral broadening of ultrashort pulses in a nonlinear medium. *Opt. Lett.* **9**, 510.
- [99] Robert Szipöcs, Kárpát Ferencz, Christian Spielmann, and Ferenc Krausz, "Chirped multilayer coatings for broadband dispersion control in femtosecond lasers," *Opt. Lett.* **19**, 201-203 (1994)
- [100] Kärtner, F. X., et al. "Design and fabrication of double-chirped mirrors." *Optics letters* **22.11** (1997): 831-833.
- [101] Matuschek, N., et al. "Back-side-coated chirped mirrors with ultra-smooth broadband dispersion characteristics." *Applied Physics B* **71.4** (2000): 509-522.
- [102] Pervak, V., et al. "1.5-octave chirped mirror for pulse compression down to sub-3 fs." *Applied Physics B* **87.1** (2007): 5-12.
- [103] Kevin Scharl, *Linear-Photoconductive-Sampling in Wide-Bandgap Dielectrics*, Diss. Imu, 2020
- [104] Trubetskov, M., et al. "Broadband phase-shifting mirrors for ultrafast lasers." *Applied optics* **59.5** (2020): A123-A127.
- [105] L. Lehnert. "Dispersion-Free Polarization State Control of Ultrashort Few-Cycle Laser Pulses". Master's thesis. Ludwig Maximilians Universität München, 2019.
- [106] Roessler, D. M., and W. C. Walker. "Electronic spectrum of crystalline lithium fluoride." *Journal of Physics and Chemistry of Solids* **28.8** (1967): 1507-1515.
- [107] Tan, Guo-Long, Michael F. Lemon, and Roger H. French. "Optical properties and London dispersion forces of amorphous silica determined by vacuum ultraviolet spectroscopy and spectroscopic ellipsometry." *Journal of the American Ceramic Society* **86.11** (2003): 1885-1892.
- [108] Scofield, John H. "Frequency-domain description of a lock-in amplifier." *American journal of physics* **62.2** (1994): 129-133.
- [109] Bloch, Felix. "Über die quantenmechanik der elektronen in kristallgittern." *Zeitschrift für physik* **52.7** (1929): 555-600.
- [110] Flores-Mancera, Miguel Angel, John S. Villarrubia, and Guerda Massillon-Jl. "Electron inelastic mean free paths for LiF, CaF<sub>2</sub>, Al<sub>2</sub>O<sub>3</sub>, and liquid water from 433 keV down to the energy gap." *ACS omega* **5.8** (2020): 4139-4147.
- [111] Shannon, Claude E. (January 1949). "Communication in the presence of noise". *Proceedings of the Institute of Radio Engineers.* **37** (1): 10–21.
- [112] Nyquist, Harry (April 1928). "Certain topics in telegraph transmission theory". *Trans. AIEE.* **47** (2): 617–644.
- [113] Kresse, G. & Furthmüller, J. Efficient iterative schemes for ab initio total-energy calculations using a plane-wave basis set. *Phys. Rev. B* **54**, 11169–11186 (1996).
- [114] Chen, G., Boldarev, A. S., Geng, X., Li, X., Cao, Y., Wang, L., & Kim, D. E. (2016). The radial dimension of a supersonic jet expansion from conical nozzle. *AIP Advances*, **6**(11), 115015.
- [115] McNaught, Alan D. *Compendium of chemical terminology*. Vol. 1669. Oxford: Blackwell Science, 1997.

[116] Sakurai, Jun John, and Eugene D. Commins. "Modern quantum mechanics, revised edition." (1995): 93-95.

[117] Högner, Maximilian. "Optical High-Order Harmonic Generation in Gas Targets with Spatially Tailored Driving Fields". Master thesis, Ludwig-Maximilians-Universität München, Fakultät für Physik, 2013.

[118] Wendl, Maximilian, Maximilian Högner, and Hanieh Fattahi. "Theoretical study: High harmonic generation by light transients." *Applied Sciences* 8.5 (2018): 728.

[119] Siegrist, Florian, et al. "Light-wave dynamic control of magnetism." *Nature* 571.7764 (2019): 240-244.



# Appendix A. Lock-in modulation:

A lock-in amplifier such as ZURICH INSTRUMENT HF2LI has differential signal input ports. In this case if you feed to signals in ports +in and -in diff, then the lock-in would measure the difference the signals fed to these two ports. If we connect our two electrodes in these ports, we will get yet again twice the signal. So, a combination of CEP flipping and differential electrode measurement will give us 4 times gain (figure. A.1 demonstrates how this method works).

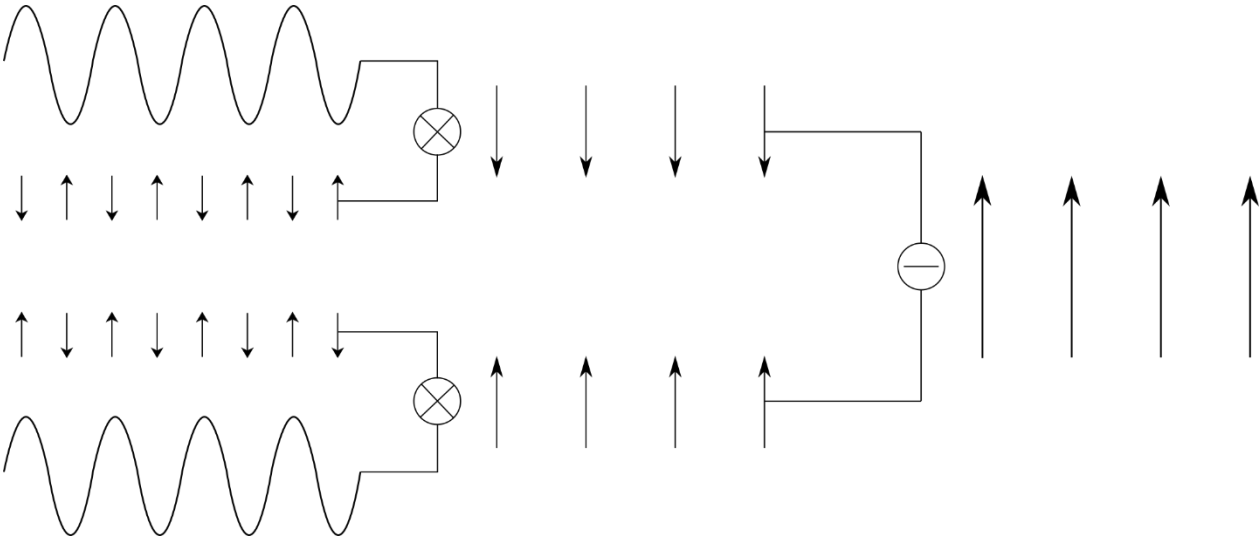


Figure A.1. Detection mechanism of the Lock-in amplifier. The data has 3 KHz rep rate. We flip the sign of each second pulse and we lock to 1.5 KHz frequency. This will remove the shot to shot laser noise and results in twice the amplitude of each single shot. Later we use the differential input of the Lock-in to read out the signal from the opposing electrodes. Since the current on the opposing electrodes has different signs, the difference input increases the signal amplitude by another factor of two and we end up having 4 times the signal.

In case of measurements of second harmonics signal we cannot use CEP flipping since a CEP flip 0 to  $\pi$  rad change the CEP of the second harmonics from 0 to  $2\pi$  rad. If we give a modulated signal like this to lock-in amplifier will result in zero signal (figure A.2).

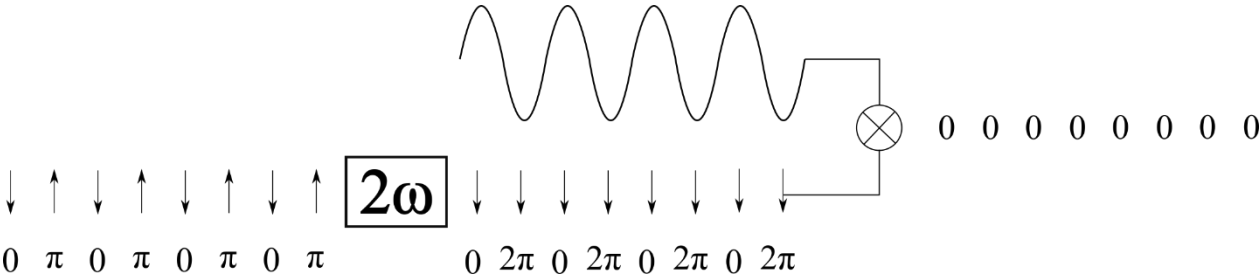


Figure A.2 Demonstration of failure of the CEP flipping scheme in 2<sup>nd</sup> harmonics detection.

Instead we use chopper in the drive arm to modulate the signal. Since we are not chopping the VUV injection we shall have, at 3 KHz, one shot that has the inject and the drive pulse and one shot that only has inject. Most of the 3 KHz signal that we have is due to the total amount of the electrons that reach the electrodes. So shot to shot we have a situation like this: shot1) inject + drive, shot2) inject. Considering the fact that locking in to 1.5 KHz with the lock-in amplifier means that we will subtract the neighboring shots at the 3 KHz, the chopping scheme will result in only having the drive part of the signal (figure A.3 shows how this chopped modulation works). One drawback of this modulation technique is that we lose an amplification factor of 2 that was the direct result of the CEP flipping (since we are blocking every second signal).

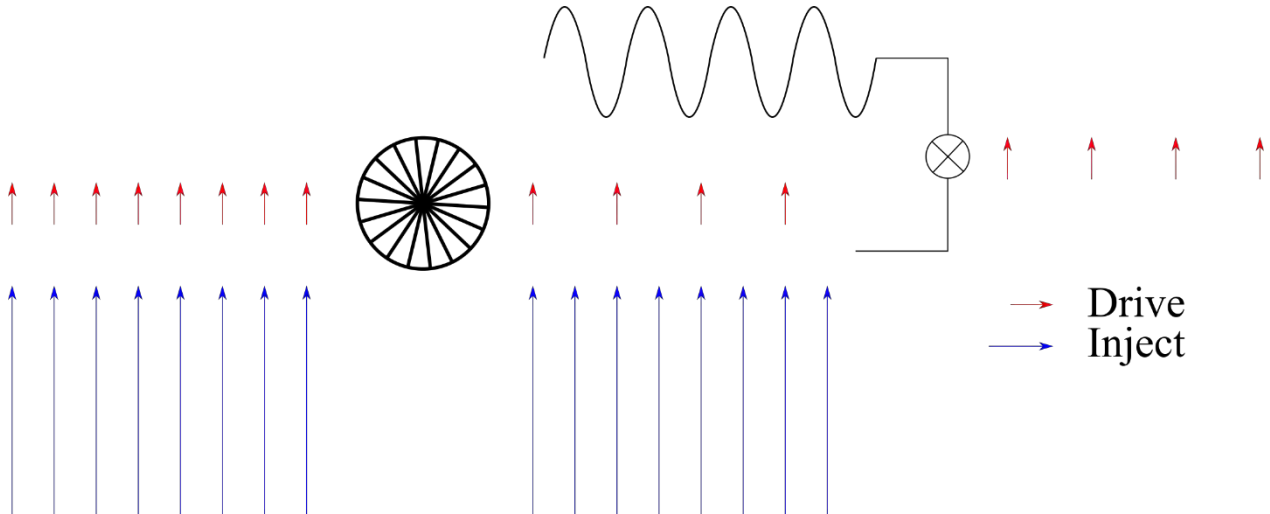


Figure A.3. Signal modulation scheme for detection of the 2<sup>nd</sup> harmonics pulse. Red arrows are indicative of the electron population transfer plus momentum change due to the driving pulse (in this case the UV). Blue arrows are indicative of the electron initial population due to the XUV ionization. The chopper is set to pass every second pulse in the drive arm creating a 1.5 KHz UV signal, while the XUV remains unchanged. When we trigger to 1.5 KHz signal in the Lock-in amplifier the resultant output is only the changes made by the UV pulse.

# Appendix B. lithium fluoride crystal:

Lithium fluoride (LiF) is an ionic crystal that has simple cubic lattice. The lattice constant of LiF is  $a = 0.4026$  nm. The reciprocal lattice of the LiF is simple cubic as well. its reciprocal lattice constant of is  $b = 2 \times \frac{\pi}{a} = 15.6065$  nm<sup>-1</sup>. Since we drive the electrons along the X symmetry of the reciprocal lattice, the edge Brillouin zone is at  $\vec{k} = (0,1,0) \times b$ . The magnitude of this point is  $k = 15.6065$  nm<sup>-1</sup>.

The energy difference for LiF between the first CB and the second CB along the L direction is 6.1 eV. Using a simple quadratic approximation, i.e:

$$\Delta E_{CB1} = \frac{\hbar^2 k^2}{2m_{\text{eff}}} \quad \text{B.1}$$

,we estimate that effective mass of the electron in this band is  $m_{\text{eff}} = 1.04 \times 10^{-30}$ kg. this is 1.52 times heavier than actual mass of electron.

The average group velocity is can be calculated as follow:

$$\langle v_g \rangle = \frac{\hbar k}{2 \times m_{\text{eff}}} = 1.18 \times 10^6 \text{ m/s} \quad \text{B.2}$$

# Appendix C. Data Archiving:

All the data presented in the current work are archived on the server of the Laboratory for Attosecond Physics at Max Planck Institute of Quantum Optics and can be found in the following directory: [/afs/ipp-garching.mpg.de/mpq.lap/publication\\_archive/](https://afs/ipp-garching.mpg.de/mpq.lap/publication_archive/)

Detailed explanation of the relation between the figures and the raw experimental data can be found in the document “Code.docx”. The figures are saved in the folder figures. The generating codes are in the folder codes. All the data related to thesis are also in the code folder in sub folders of data and XUV.

# Acknowledgements

I would like to thank Prof. Ferenc Krausz that without his blessing and his insight, this work would have never been done. Your motivation always helped me in hardest times. All the best to you. I wish I can also host you once in Iran.

The next person I would like to send gratitude is Prof. Martin Schultze. In Iran we say being a teacher is profession of prophets. What we mean is that a true teacher can create change and through this change life becomes better for everybody. I would like to use this opportunity to express my greatest gratitude to my most important teacher:

Dear Martin, If it wasn't for your faith in me, I would have never been able to reach this position right now. Four years ago, you answered my email kindly and put your trust in me and brought me to Germany. Like a father patient you taught me how to work in lab and gave best kind of motivations. My deepest gratitude for you. You are always in my prayers. I wish I can host you once show you Iran.

I am here in this point writing acknowledgements and I can't thank you enough, Dr. Matthew Weidman. Last two years you helped me a lot in finishing my PhD your feedbacks and your supervisions gave helped me a lot. Also thanks a lot for helping me writing my thesis. All the best to you too.

Next person in line is of course Dr. Marcus Ossiander. Best postdoc ever. It is absolutely an honor working by your side. I can't really understand how on earth you are this good. I deeply enjoyed learning physics from you and miss deep physics discussions I had with you.

Dear Vlad, Nick, Johannes and Thomas, thanks a lot for good scientific advices and helps. I Wish all the best.

As for colleagues, first and foremost I would like to give my gratitude to Dr. Florian Siegrist who taught me first-hand how to work with laser. I also enjoyed a lot hang around with you, especially after hour drinks.

Next, I would like to thank Dr. Julia Gessner. You helped me a lot to settle in first when I arrived in Germany. My deepest gratitude to you as well

Next all the best to my current and former good colleagues Amelie Schulte, Kevin Scharl, Lukas Lehnert and Johannes Burger. All the best to all of you guys.

I would like to mention Mr. Simon Reiger. You are the best officemate. Thanks a lot for putting up with all my ups and downs. In most stressful times talking to you was a source relaxation. Wish you best my friend.

I would like give my warmest regards to my colleagues of office B1.33. Dr. Mikhail Mamaikin, Dr Enrico Ridente, Najd Altwajry and Muhammad Qasim. You are my family here. Through all ups and downs I felt I am home spending time with you guys. I wish all best. I wish I host once in Iran.

Especial Thanks to my kind land lady. Dear Jutta, Thanks a lot for sharing with me the warmth of your house. My most sincere prayers always for you.

مادر و پدر عزیزتر از جانم:

دستان را از دور دست می بوسم. از اینکه مهربانج بسیار بزرگ نموده و عالی ترین شرایط را در عین سختی برایم مهیا ساختید، بسیار متشکرم. چقدر دلم بر اتان تنگ است. ای کاش شرایط جور دیگری بود و همیشه زیر سایه کرمتان می بودم. انشا الله سایه کرمتان همیشه روی سرم باشد.

برادر و خواهر عزیزم:

ممنون از اینکه ای بار خرد و توان ره گمگ کردن. موخایی دلوم بر اتان تنگ رفته. از دور ما چنان مویکونوم. ای کاش اونجه بودوم باجم خوش گذروندم.

خاله نوری عزیزم:

ممنون که در این دیار غربت برایم چون مادی دلسوز بودید. دستان را می بوسم.

به پایان آمد این دفتر، حکایت همچنان باقیست